Aus dem Institut für Biochemie

der Medizinischen Fakultät Charité – Universitätsmedizin Berlin

DISSERTATION

The role of the actin-binding-protein Drebrin in astrocytic scar formation upon traumatic brain injury

Die Rolle des Aktin-bindenden Proteins Drebrin während der astrozytären Narbenbildung nach traumatischer Gehirnverletzung

zur Erlangung des akademischen Grades

Doctor of Philosophy (PhD)

vorgelegt der Medizinischen Fakultät

Charité – Universitätsmedizin Berlin

von

Juliane Schiweck

Datum der Promotion: 25.11.2022

Table of Contents

Abstract

Injuries to the central nervous system have debilitating consequences for affected individuals, since neuronal regeneration, tissue repair and remodeling are limited. In order to avoid spreading of inflammation and neurodegeneration, astrocytes initiate a program termed 'reactive astrogliosis' and form an astrocytic scar at the injury site. Here, we investigated the role of the actin-binding protein Drebrin during reactive astrogliosis. We show that Drebrin is not expressed in astrocytes under physiological conditions, but is upregulated in astrocytes *in vitro* and *in vivo* upon injury. Genetic deletion of Drebrin leads to impaired polarization of scar-forming astrocytes in the short term and abolishes astrocyte reactivity in the long term. This defective astrocytic scar formation in Drebrin deficient mice is accompanied by excessive neurodegeneration *in vivo*.

At the cellular level, we show that Drebrin switches actin homeostasis from branched ARP2/3-dependent actin arrays to microtubule-compatible scaffolds. This organization of the actin cytoskeleton by Drebrin, in turn, allows for the formation of Rab8-positive tubular endosomes which extend along microtubules. Drebrin deficient astrocytes fail to form Rab8+ tubular compartments upon injury due to excessive ARP2/3 activity and thus, branched actin networks do not support the extension of Rab8+ tubular endosomes along microtubules. We further show that Rab8+ tubular endosomes serve as a trafficking compartment for astrogliosis-mediating focal adhesion proteins, as Drebrin deficient astrocytes show impaired localization of β1-Integrin.

In conclusion, we establish a novel role for the actin-binding protein Drebrin in injury-induced membrane trafficking and demonstrate the importance of Drebrin for astrocyte-mediated neuroprotection after traumatic brain injury in mice.

Zusammenfassung

Verletzungen des zentralen Nervensystems (ZNS) haben für Betroffene schwerwiegende Folgen, da die neuronale Regeneration, Gewebereparatur und Geweberemodellierung im ZNS eingeschränkt sind. Um eine Ausbreitung von Inflammation und Neurodegeneration zu verhindern, leiten Astrozyten ein Programm ein, mit dessen Hilfe an der Verletzungsstelle eine astrozytäre Narbe gebildet wird. Durch diese sogenannte ‚reaktive Astrogliose' können Schäden lokal begrenzt und das gesunde Gehirngewebe vor schädlichen Einflüssen geschützt werden.

In dieser Arbeit untersuchen wir die Rolle des Aktin-bindenden Proteins Drebrin während der reaktiven Astrogliose. Wir zeigen, dass Drebrin unter physiologischen Bedingungen nicht in Astrozyten exprimiert wird, sondern bei Verletzung in Astrozyten *in vitro* und *in vivo* hochreguliert wird. Die genetische Deletion von Drebrin führt kurzfristig zu einer gestörten Polarisation narbenbildender Astrozyten und hebt langfristig die Astrozytenreaktivität auf. Diese defekte astrozytäre Narbenbildung bei Drebrin-defizienten Mäusen wird *in vivo* von exzessiver Neurodegeneration begleitet.

Auf der zellulären Ebene zeigen wir, dass Drebrin die Aktinhomöostase dahingehend beeinflusst, dass statt ARP2/3-abhängiger Aktin-Arrays Mikrotubuli-kompatible Aktin-Strukturen gebildet werden. Diese Organisation des Aktin-Zytoskeletts durch Drebrin ermöglicht wiederum die Bildung von Rab8-positiven tubulären Endosomen, die sich entlang von Mikrotubuli erstrecken. Drebrin-defiziente Astrozyten können aufgrund einer übermäßigen ARP2/3-Aktivität keine Rab8+-tubulären Kompartimente bilden, da verzweigte Aktinnetzwerke die Verlängerung von Rab8+-tubulären Endosomen entlang der Mikrotubuli verhindern. Wir zeigen weiterhin, dass Rab8+ tubuläre Endosomen als Transportkompartiment für Astrogliose-mediierende fokale Adhäsionsproteine dienen, da Drebrin-defiziente Astrozyten eine beeinträchtigte Lokalisation von β1-Integrin aufweisen.

Zusammenfassend zeigen wir hier eine zuvor noch nicht bekannte Rolle von Drebrin für die Astrozyten-abhängige Neuroprotektion nach traumatischen Hirnverletzungen bei Mäusen, die auf Drebrins Funktion während des verletzungsinduzierten Membrantransport in Astrozyten zurückzuführen ist.

Introduction

1.1 CNS injury

Upon injury, mammals initiate a wounding response consisting of hemostasis, inflammation, repair, and remodeling, followed by a resolution phase (Stroncek & Reichert, 2008). This process restores key functions in many organs, however, injuries to the adult mammalian central nervous system (CNS) often result in permanent damage because tissue repair and remodeling in the CNS are insufficient. Impairments caused by CNS injury are extremely disabling, ranging from immediate and permanent loss of movement control following spinal cord injury (SCI) (Courtine & Sofroniew, 2019) to long-term consequences in response to mild traumatic brain injury (TBI), such as seizures, neuropsychiatric symptoms or increased susceptibility to neurodegenerative disorders (Burda et al., 2016).

CNS injuries have a high estimated global prevalence (~55 million for TBI and ~27 million for SCI) and represent a burden to health-care systems due to associated high health-care cost (Injury & Spinal Cord Injury, 2019). Moreover, available therapies rarely restore function due to the limited success of regenerative strategies (Tam et al., 2014).

The development of successful therapies is challenging because of the complexity of the CNS and its inaccessibility due to limited diffusion of drugs across the blood-brain barrier (Tam et al., 2014).

To aid the development of novel regenerative therapies, it is necessary to gain a more detailed understanding of CNS injury-induced processes on a cellular level.

1.2 Brain cells during injury

The CNS is a complex cellular network consisting of neurons and glial cells, which are separated from the rest of the body by the blood-brain barrier. Disruption of this highly organized system upon injury coordinates a multifaceted and multicellular response in an attempt to preserve CNS integrity (Burda & Sofroniew, 2014; Vainchtein & Molofsky, 2020).

While many cell types in other tissues can proliferate and regenerate, postmitotic neurons in the CNS have a limited capacity of regeneration: transected or damaged axons of neurons fail to regrow spontaneously (Anderson et al., 2016) and - despite a limited amount of neural sprouting after injury - fail to reintegrate into their original neural circuits to rebuild functional connections (Jara et al., 2020; Mahar & Cavalli, 2018). Reasons for the poor regeneration in the mature mammalian CNS include (i) limited capacity to reinitiate intrinsic developmental growth programs in adult neurons, (ii) the absence of extracellular growth factors and guidance cues that support neuronal growth and (iii) the presence of inhibitory molecules at the injury site (Anderson et al., 2016). This absence of

functional regeneration in neurons makes the containment of damage at the injury site crucial to avoid spreading of inflammation throughout the CNS into uninjured areas.

Similar to other tissues, injuries to the CNS trigger a coordinated wound healing response involving many different cell types. First, disruption of the blood-brain barrier initiates hemostasis within seconds after an insult. The entry of serum and blood cells at the injury site leads to formation of a blood clot. Signaling molecules released during hemostasis initiate an inflammation response within minutes to hours. During inflammation, microglia, the only resident phagocytic cells in the brain, are activated and recruited to the injury site, where they, in conjunction with invading macrophages, degrade damaged axons and myelin from compromised oligodendrocytes (Stroncek & Reichert, 2008).

A large variety of extracellular signals then act as molecular regulators to initiate an injury response in astrocytes (Sofroniew, 2014).

Collectively, this injury response leads to the formation of a 'glial' scar. The glial scar refers to a lesion core, consisting of a mixture of deposited extracellular matrix proteins and non-CNS resident cells which invade the lesion site, including perivascular-derived fibroblasts, pericytes, ependymal cells and phagocytic macrophages. Around the lesion core, a compact border is formed by astrocytes, NG2-Glia and microglia (Adams & Gallo, 2018).

The term glial scar will be used in this thesis when referring to the above definition. In contrast, astrocytic scar will be used when referring to the specific scar forming behavior of astrocytes only. In this thesis, I will focus on the impact of CNS injury on astrocytes and how astrocytes contribute to the CNS wounding response.

1.3   Astrocytes and astrogliosis

Under physiological conditions, adult astrocytes occupy distinct territorial domains in the brain, with little overlap of extending processes between different astrocytes (Bushong et al., 2004). Within their domains, astrocytes exert several structural, metabolic, and homeostatic functions (Santello et al., 2019). During CNS injuries, astrocytes become reactive, a process that is accompanied by substantial changes in gene expression (Burda et al., 2016) and morphology (Schiweck et al., 2018) .

Reactive astrogliosis is a gradual rather than an all-or-nothing response, ranging from reversible changes in gene expression and cell hypertrophy, to formation of permanent astrocytic scars that entail substantial tissue rearrangement (Anderson et al., 2014). In terms of morphology, astrocytes tune their responses to the severity of the insult: Upon mild and diffuse brain injuries, astrogliosis responses are characterized by upregulation of intermediate filaments and hypertrophy of soma and protrusions. Penetrating, profound lesions trigger formation of an astrocytic scar, where reactive

astrocytes lose their spongiform morphology and territorial domains due to proliferation and extension of long polarized processes towards the injury site, as depicted in **Figure 1** (Schiweck et al., 2018).

Whether astrocytic scars and glial scars are in fact a beneficial or detrimental process has been the subject of intense scientific debate (Adams & Gallo, 2018; Anderson et al., 2016; Bradbury & Burnside, 2019; Silver & Miller, 2004; Yang et al., 2020) and is likely to be answered with 'both', depending on molecular signaling events and context (Sofroniew, 2009):

On the one hand, astrogliosis can be regarded as a defensive mechanism that helps to prevent the propagation of inflammation into the uninjured brain parenchyma, limits the expansion of neurodegeneration (Faulkner et al., 2004; Frik et al., 2018) and even promotes axonal regeneration (Anderson et al., 2016). On the other hand, the persistence of an astrocytic scar at the injury site and deposition of associated inhibitory molecules can also impair neuronal regeneration (S. A. Busch & J. Silver, 2007; Silver & Miller, 2004).

While molecular triggers of astrogliosis as well as signaling events and anatomy of the astrocytic scar are well described (Sofroniew, 2015), less is known about the molecular mechanisms responsible for the morphological changes required for astrocyte polarization and extension of processes towards the injury site. The following section will discuss the astrocytic cytoskeleton and the current state of knowledge on rearrangements during astrogliosis.
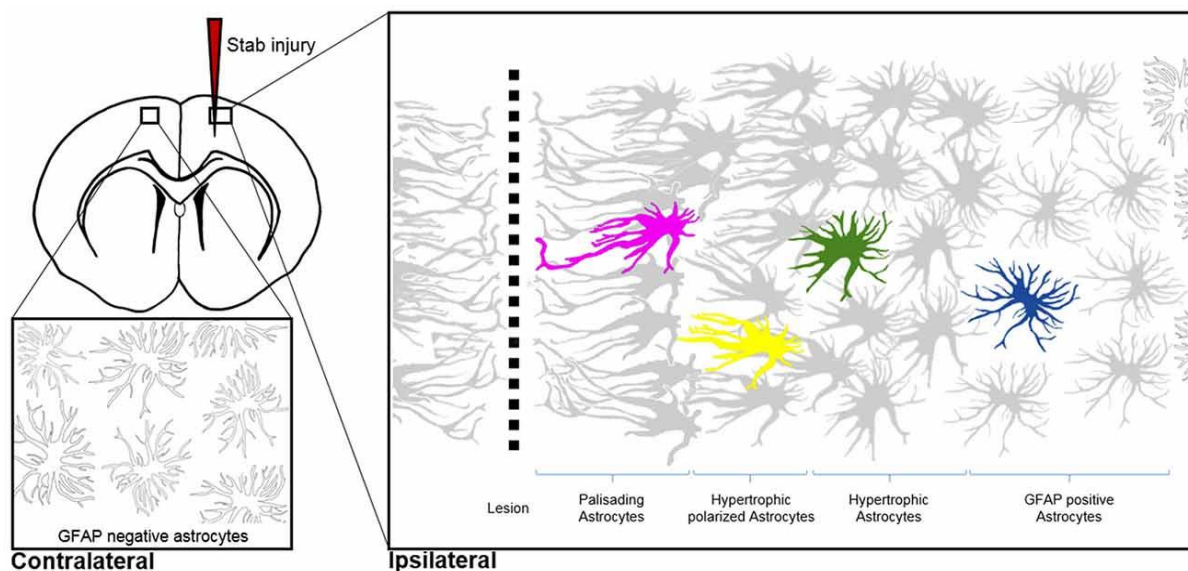
Figure 1 Morphological changes during astrogliosis with respect to the lesion site, from (Schiweck et al., 2018)

1.4 Astrocytic cytoskeleton

The astrocytic cytoskeleton is composed of microtubules, intermediate filaments and microfilaments (actin cytoskeleton). These three filament systems interact and cooperate to fulfill a plethora of important functions, including establishing and maintaining cell shape, allowing for intracellular transport and facilitating cell migration (Hohmann & Dehghani, 2019). Therefore, the cytoskeleton directly mediates some of the important features of astrogliosis.

1.4.1 Microtubules during astrogliosis

Microtubules provide the basis for important cellular functions, such as mitosis and cell division or long-range transport of intracellular vesicles and organelles (Lasser et al., 2018).

Most of the research on microtubules during astrogliosis was obtained in *in vitro* experiments, where astrocytes migrate into wound areas, unlike astrocytes *in vivo*, where they do not migrate but rather proliferate and extend processes to form the astrocytic scar (Bardehle et al., 2013). *In vitro*, microtubules are enriched in extending astrocytic processes and reach the leading edge of astrocyte protrusions, which stands in contrast to other cell types, where few microtubules actually invade the actin-rich leading edge (Etienne-Manneville & Hall, 2001). Pharmacological depolymerization of microtubules demonstrated that microtubules are essential for the outgrowth of palisade-like processes.

In vitro experiments have shown an important role for the small GTPase Cdc42 in regulating outgrowth of polarizing processes in astrocytes, however, deletion of Cdc42 *in vivo* did not affect astrocyte polarization but rather impaired astrocyte proliferation in response to TBI (Robel et al., 2011). Interestingly, *in vivo* experiments employing a model of SCI in rats showed that pharmacological stabilization of microtubules reduced fibrotic scar formation and promoted neuronal regeneration. However, the microtubule stabilization did not affect astrogliosis, suggesting that the success of this treatment is based on astrocyte-extrinsic processes (Ruschel & Bradke, 2018).

1.4.2 Intermediate filaments in astrogliosis

While the composition of the astrocytic intermediate filament network varies during different developmental stages, maturing and fully differentiated astrocyte intermediate filaments are composed of Vimentin and GFAP (Sultana et al., 2000). Levels of these proteins vary in brain regions, for example, astrocytes located in the adult cortex are largely negative for GFAP (Walz, 2000; Kimelberg, 2004).

A special role is attributed to the intermediate filament system during astrogliosis: CNS insults trigger a prominent upregulation of GFAP and Vimentin in astrocytes, that is considered a hallmark of

reactive astrogliosis (Pekny, 2001). Early studies investigating the effect of genetic ablation of GFAP and Vimentin during CNS injury found impaired formation of astrocytic scars. Scars in GFAP and Vimentin deficient (GFAP$^{-/-}$Vim$^{-/-}$) mice were less dense and fissures filled with blood, tissue fluid or debris were present at the injury site, emphasizing the importance of the intermediate filament system for the astrogliosis response (Pekny, 2001). Nevertheless, other studies showed positive effects of GFAP and Vimentin deficiency. Glial scar formation in GFAP$^{-/-}$Vim$^{-/-}$ mice was reduced while axonal plasticity and functional recovery were enhanced (Menet et al., 2003), which is in line with previous findings showing that the presence of the glial scar has negative effects on neuronal regeneration (Sarah A. Busch & Jerry Silver, 2007).

1.4.3 The actin cytoskeleton during astrogliosis

Microfilaments are formed by the protein Actin, and are classically considered as a determinant in regulating cell morphology and migration (Pollard & Cooper, 2009). Most cellular processes, including endocytosis, cellular transport and membrane trafficking also rely on the actin cytoskeleton. The dynamic remodelling of complex actin network structures is the basis for a plethora of different tasks in eurkaryotic cells (Pollard & Cooper, 2009).

Actin exists as free globular monomers (G-Actin) and as filamentous polymers (F-Actin). Actin polymerization into polar filaments occurs via ATP-bound G-Actin monomers. The first step of F-actin formation is the generation of actin nucleation sites, where the rapid addition of ATP-G-actin units drives the fast growth of new filaments. In vitro, three actin monomers spontaneously form a trimer, which serves as nucleation site for a new filament. ATP-bound G-actin incorporates at the fast growing plus end, while the filament actin subunits hydrolyse ATP to ADP. At the minus-end, ADP-actin dissociates from the filament. In vitro, the concentration of ATP-bound G-actin determines the rate of actin nucleation, polymerization, and turnover. Eukaryotic cells possess a complex machinery of actin-binding proteins, which control actin nucleation, polymerization, turnover, and organization into suprastructures in a tightly controlled spatial-temporal manner (Pollard & Cooper, 2009). For instance, polymerase-like proteins like Ena/VASP or formins, nucleate actin and promote the growth of linear filaments by continuously adding G-actin molecules to the plus-ends (Breitsprecher et al., 2008; Hansen & Mullins, 2010; Romero et al., 2007). Subsequently, cross-linking actin-binding proteins organize newly formed linear actin filaments into higher suprastructures, such as bundles and networks (Pollard & Cooper, 2009).

Branched actin arrays constitute another pool of dynamic networks, which are directly formed by the Arp2/3 complex. This protein complex resembles an actin trimer but requires an upstream activation by additional proteins, so called 'nucleation promoting factors'. When activated, the Arp2/3 complex binds to existing filaments and initiates the generation of new daughter filaments

(Pollard, 2007; Pollard & Cooper, 2009). Both types of actin networks create distinct morphological features of eukaryotic cells: Linear actin filaments constitute the structural components of antenna-like filopodia and necks of dendritic spines in neurons. Arp2/3 complex-dependent networks create lamellipodia in moving cells, veil-like leading edges of neuronal growth cones, and head-like structures of mature dendritic spines (Gallop, 2020; Konietzny et al., 2017). In addition, branched actin arrays are involved in membrane trafficking, for instance during the internalization and propulsion of endocytic vesicles (Chakrabarti et al., 2021). Both linear and branched actin networks are balanced in homeostasis by competing for a common pool of G-actin molecules (Rotty & Bear, 2014).

Upon CNS injury, reactive astrocytes undergo comprehensive changes in their morphology like hypertrophy and the extension of long processes. Those changes undoubtedly require an extensive remodeling of the actin cytoskeleton. However, only few actin regulators were already described to be involved in astrogliosis responses: The cross linking and bundling proteins α-actinin and paladin, are upregulated during astrogliosis (Abd-El-Basset & Fedoroff, 1997; Boukhelifa et al., 2003).

One previous study shows that the Arp2/3 complex negatively regulates astrogliosis: Inhibition of Arp2/3 in brain slices increased astrocyte cell body size and number of large processes, reminiscent of reactive astrocytes upon diffuse trauma. In a model of stroke, the inactivation of the Arp2/3 complex accelerated the hypertrophy of reactive astrocytes, while the overactivation of the Arp2/3 complex suppressed cell body expansion (Murk et al., 2013).

The fact that there is an upregulation of actin-binding proteins upon injury, and the observation that inhibition of actin-binding proteins induces changes in cell morphology that are reminiscent of astrogliosis suggest that the regulation of the actin cytoskeleton is an important factor determining the astrocytic response to injury. Little is known about the role of other actin-regulators during the astrocytic injury response and revealing the contribution of further actin regulators to this process will enhance our understanding of the molecular regulation of astrocytic scar formation. Following this line of thought, here, I investigated the role of the actin-binding protein Drebrin during astrogliosis. The following section will introduce Drebrin and its function.

1.5   Drebrin

The 'developmentally regulated brain protein' (Drebrin), consists of two major isoforms, Drebrin E and Drebrin A which are transcribed from a single gene through alternative splicing (Majoul et al., 2007) (Willmes et al., 2017). While Drebrin A is specifically expressed by mature neurons, Drebrin E

is not only expressed in immature neurons but also found in adult non-neuronal cells inside and outside the CNS (Shirao et al., 2017).

In principle, Drebrin (DBN) stabilizes F-Actin by sidewise binding and competes with other actin-binding proteins, thereby altering actin dynamics and impacting various cellular processes (Mikati et al., 2013).

Since Drebrin was discovered in neurons, where it is highly enriched in dendritic spines, most of the work in general and in our group in particular, has addressed the role of Drebrin in this cell type. While Drebrin deficiency in neurons was shown to reduce long-term potentiation and cause altered spine morphology in hippocampal neurons by other groups (Jung et al., 2015; Kojima et al., 2016), data obtained in our group did not corroborate these findings. No alterations regarding basic properties at hippocampal synapses or impairments of synaptic plasticity could be found in Drebrin-deficient mice at physiological conditions (Willmes et al., 2017). However, under conditions of oxidative stress, Drebrin exerts a protective function by stabilizing dendritic spines (Kreis et al., 2019), suggesting a specific role for Drebrin during cellular stress responses.

In non-neuronal cells, Drebrin was shown to play a role during viral infection: Drebrin restricts dynamin-dependent Rota-virus entry into host cells and, in its function as an actin binding protein, acts as a negative regulator of different dynamin-dependent endocytic pathways (Li et al., 2017).

Regarding astrocytes, the role of Drebrin was investigated previously by only one study. In their study, Butkevitch et al. postulated a role for Drebrin in maintaining Connexin 43 at the plasma membrane. The authors showed that a lack of Drebrin leads to impaired cell-cell coupling and internalization of gap junctions in cultured astrocytes (Butkevich et al., 2004).

To my knowledge, no study addressed the role of Drebrin during CNS injury. Given that actin-binding proteins have just emerged as important players in regulating astrogliosis and Drebrin plays a role in stabilizing actin filaments and modulating actin dynamics by competing off other actin regulators, it is conceivable that Drebrin may be involved in cytoskeletal rearrangements in astrocytes upon injury.

2. Aims of the Thesis

CNS injury has detrimental consequences for affected individuals, because tissue repair and remodeling are limited. Shielding off uninjured brain parenchyma from the injury site is necessary to avoid spreading of inflammation and neurodegeneration. In response to injury, astrocytes initiate a program termed 'reactive astrogliosis' which is characterized by altered gene expression and drastic changes in morphology. Astrocytes extend long processes and form an astrocytic scar that depends on the rearrangement of the cytoskeleton.

At the level of the actin-cytoskeleton, actin regulatory proteins control changes in actin networks. One such actin-binding protein is Drebrin, which stabilizes F-Actin by sidewise binding and alters actin dynamics by competing against other actin-binding proteins. I thus hypothesize that Drebrin in astrocytes participates in remodeling of the actin cytoskeleton during astrogliosis.

Therefore, the overall aim of this thesis is to elucidate the role of the actin-binding protein Drebrin during astrogliosis. More specifically, I aim to investigate the impact of Drebrin deficiency in an in vivo model of TBI in mice and to pinpoint the effects of Drebrin loss for astrogliosis on a molecular level *in vitro*, using primary astrocyte cultures in conjunction with an injury model for cell culture.

3. Methods

All methods employed in this thesis are described in detail in the paper associated with this Thesis (Schiweck et al., 2021). A short summary of the most important methodologies is provided below.

Ethical approval and mouse strains

This study was approved by the Landesamt für Gesundheit und Soziales' (LaGeSo; Regional Office for Health and Social Affairs) in Berlin, permit number G0189/14. All animals were handled in accordance to the permit after ethical approval.

Mouse strains used were $Dbn^{-/-}$ mice described previously (Willmes et al., 2017)), B6.CAMK:Cre/Dbnfl/fl mice (generated by crossing B6.Cg-Tg(Camk2a-cre)T29-1Stl/J (kindly provided by Dietmar Schmitz, Charité Berlin;) with B6. Dbnfl/fl mice) and BAC Aldh1L1 eGFP mice (described previously in (Yang et al., 2011)).

Antibodies, reagents, plasmids

Antibodies, reagents and plasmids and information on respective concentrations and applications can be found in the original publication (Schiweck et al., 2021).

Cell culture and plasmid transfection

Cortical astrocytes were isolated from wild type or $Dbn^{-/-}$ mouse brains as described previously (Murk et al., 2013). Astrocytes were expanded until 90% confluency and microglia were selectively removed by treatment with 60 mM l-leucine-methylester (LME, Sigma) for 90 minutes in DMEM supplemented with 10% fetal bovine serum (FBS). Astrocytes were then split and replated for imaging or biochemical experiments. For microglia cultures, astrocyte-microglia mixed cultures were placed on a shaker for 2 h at 150 rpm. Supernatant containing microglia was collected and plated on poly-ornithine-coated glass coverslips. Primary mixed cortical cultures were obtained from male and female wild type or $Dbn^{-/-}$ mouse embryos (embryonic day E16.5) as described previously (Schrötter et al., 2016). HEK293TN were obtained from BioCAT (Cat. no. LV900A-1-GVO-SBI). Astrocytes were transfected using TransIT LT1 (Mirus) according to the manufacturer's protocol. Information on lentivirus production, astrocyte infection and RNA interference can be found in the original publication.

Scratch wound in vitro and live-cell imaging

Astrocytes were cultured to confluency in phenol red-free DMEM (Thermo Scientific) with 10% FBS. Scratch wounds were performed as established previously (Etienne-Manneville & Hall, 2001). To ensure sufficient scratching of the monolayer, different scratch patterns were performed. 18 mm coverslips, were scratched once vertically and once horizontally; 4 well μ-slides dishes (IBIDI), were scratched once vertically; 30 mm dishes were scratched three times horizontally and vertically. Scratch wounded astrocytes were subjected to western blot analysis or live-cell imaging, employing a Nikon Widefield microscope with CCD camera, scanning stage, and environmental control chamber (OKO lab) and a ×40 objective (N.A. 0.7) with 1.5× intermediate magnification.

Quantification of membrane tubules

Rab8a+ tubular membrane compartments were quantified based on a macro for Fiji previously developed by Pasqualin et al. (Pasqualin et al., 2014). I modified the code to analyze video sequences acquired in live imaging experiments. Code available on github: https://github.com/jschiweck/TubuleMacro .

Pharmacological treatments

During live cell imaging experiments a 30 min baseline of GFP-Rab8A-expressing cells was recorded before either 100 nM Cytochalasin d (Merck Calbiochem, Cat. no. 250255), 100 μM CK-666 (Sigma-Aldrich, Cat. no: SML0006-5MG) or 25 μM SMIFH2 (Sigma-Aldrich, Cat. no. S4826-5MG) were added and effects of the treatments were imaged. For imaging of microtubule dynamics, astrocytes were treated with 1 μM SiR-tubulin for 6 hours prior to imaging (Spirochrome, cat#: SC002).

Immunocytochemistry and antibody feeding

Cultured astrocytes were fixed using 3.7% formaldehyde in cytoskeleton-preservation buffer (25 mM HEPES, 60 mM PIPES, 10 mM EGTA, 2 mM MgCl2, pH 7.4) for 20 min. Cells were washed thrice with cytoskeleton-preservation buffer. Immunocytochemistry was performed as follows: Cells were permeabilized by incubation with 0.02% Triton X-100 in Phosphate-buffered saline (PBS) for 3 minutes; brief incubation in 1% bovine serum albumin (BSA) in PBS; incubated with primary antibodies in PBS for 1h at RT; three 5-minute washes with PBS; brief incubation in 1% BSA in PBS; incubation with secondary antibody in 1% BSA for 1h at RT, followed by three 5 minute washes with PBS. Cells were mounted in Mowiol. In order to visualize endogenous Rab8, the protocol was adapted: PBS was replaced by cytoskeleton-preservation buffer and permeabilization time was increased to 30 min. For antibody feeding assays, astrocytes were serum starved for one hour and incubated with Integrin antibody (9EG7 antibody, BD Bioscience, 1:20) on ice for 1 hour. Cells were then washed thrice with DMEM+ 10% FBS and placed into the incubator too internalize the antibody

at 37 °C . After internalization, astrocytes were washed with ice-cold PBS and surface antibody was removed with acetic acid pH3 (0.5 M NaCl, 0.5% Acetic Acid in ddH2O). Cells were then fixed as described above.

Confocal microscopy and imaging processing

Cells were imaged on a Nikon A1Rsi+ (Nikon) confocal microscopes. Large image and multipoint scans were performed on Nikon A1 microscopes using an automated stage. Image processing was performed in FIJI and/or Imaris (Bitplane). For a detailed analysis on image processing and focal adhesion analysis performed see (Schiweck et al., 2021).

Surface biotinylation and internalization assay

Cultured astrocytes were incubated in 1 mg/ml membrane-impermeable EZ-Link Sulfo-NHS-SS-Biotin (ThermoFisher) in ice-cold PBS pH 8 for 2 h at 4 °C with gentle rotation before quenching and lysis. For a detailed description of Biotinylation see (Schiweck et al., 2021).

Protein lysate preparation, SDS–PAGE, and WB

Cultured astrocytes were washed once with cold PBS and lysed in cold radioimmunoprecipitation assay (RIPA) buffer, supplemented with protease inhibitors (Merck, Calbiochem set III, Cat. no. 539134) for 20 minutes on a rotator at 4 °C. Cell lysates were cleared by centrifugation at $20,000 \times g$ and supernatant was transferred to a fresh tube with sample buffer (Roti load I SDS buffer). Lysates were boiled for 3 min at 98 °C. Samples were loaded onto SDS-PAGE gels and were transferred to nitrocellulose membranes using a wet blot tank system (Bio-Rad). Membranes were blocked for 1 h at room temperature in 5% skim milk in TBS-T. Membranes were then incubated with primary antibodies diluted either in 5% skim milk or 5% BSA in TBS-T overnight. The next day, membranes were washed 3×10 min in TBS-T and incubated with HRP-coupled secondary antibody for 1 hour, followed by 3×10 washes in TBS-T before detection. Signals were quantified using FIJI and measurements were normalized to loading control.

***In vivo* stab wound and spinal cord injury**

Mice were anesthetized using ketamine (100 mg/kg) and xylazine (10 mg/kg). Full anesthesia was verified by monitoring breathing and toe reflexes. Mice were placed on a stereotactic frame (Kopf Stereotax) while maintaining body temperature at 37 °C, using a heating blanket. An incision was created in the scalp and a small craniotomy was drilled above M1 motor cortex (bregma: −1 mm; lateral: 1 mm). To induce a stab wound, a 33-gauge injection needle was inserted into the motor cortex and moved up and down three times (0.8 mm). The needle was removed and the scalp was

sutured. Metamizol (5 mg/ml) was added to drinking water until, after 7 or 30 days, mice were sacrificed by sedation with isoflurane and perfused with PBS and 4% formaldehyde. Brains were removed and placed in formaldehyde for 24 h before placing them in 30% sucrose in PBS.

IHC, tissue clearance and histology

Coronal sections (60 μm) were obtained by sectioning mouse brains, permeabilized with 1% Triton X-100 in PBS overnight and blocked in 5% BSA. IHC for GFAP was performed to identify sections with a scar. GFAP-positive sections were then selected and stained for additional markers. Sections were then fixed in 4% formaldehyde for 1 h at 4 °C. Brain slices were cleared by incubation in tissue clearing buffer ScaleA2 (4 M UREA, 10% (wt/vol) glycerol, 0.1% (wt /vol) Triton X-100 and 0.1× PBS) for 48 h. Transparent slices were mounted on glass slides using Mowiol with 4 M Urea and analyzed by confocal microscopy. For visualization of RAB8 tubules *in vivo*, animals were perfused with 3.7% formaldehyde in a cytoskeleton-preservation buffer (25 mM HEPES, 60 mM PIPES, 10 mM EGTA, 2 mM MgCl2, pH 7.4) instead of formaldehyde in PBS. For Rab8 visualization, brain slices were not tissue cleared and mounted in Mowiol. Creysl violet staining was performed as per manufacturer instructions (Merck Millipore, 105235).

Purification of recombinant GST-hSLP4A and isolation of endogenous GTP-bound RAB8 from astrocytes

Recombinant GST-hSLP4A was expressed in and purified from BL21 Rosetta DE3 Eschechia coli (Merck, Ca. no. 70954) as described in the original publication (Schiweck et al., 2021). For coating of the beads, bacterial lysates were incubated with glutathione sepharose beads for 1 hour on a rotating wheel at 4 °C. Subsequently, beads were washed three times with ice-cold lysis buffer (20 mM HEPES, 150 mM NaCl, 0.5% Triton X-100). For isolation of GTP-bound Rab8, astrocyte lysates were rotated with the coated beads for 1 hour at 4 °C, followed by four washes with Lysis buffer supplemented with protease inhibitors. Samples were then subjected to SDS–PAGE and WB.

Electron microscopy

Electron microscopy was performed by our collaborators. A detailed description of the procedure used can be found in the original publication (Schiweck et al., 2021).

Statistics and reproducibility

All statistical analyses were performed in GraphPad Prism software (Prism 7.0). The data are reported as bar graphs showing individual values and means ± SEM, or as box-and-whiskers plots, ranging from minimum to maximum values, sample sizes are reported in the respective figure

legends. All data were tested for normality and accordingly subjected to parametric or non-parametric statistical analysis. No experiments were excluded from the analyses.

4. Results

The results obtained in this thesis were generated in close collaboration with my colleagues Dr. Kai Murk, Dr. Julia Ledderose, Marta Ornaghi and Dr. Agnieszka Münster-Wandowski. The exact contributions are mentioned in the section 'Detailed Declaration of Contributions'.

4.1. Drebrin is upregulated in response to injury in astrocytes *in vitro* and *in vivo*

This project set out to study the actin-binding protein Drebrin in astrocytes. In a first step, we assessed whether Drebrin was present in astrocytes under physiological conditions. To this end, we examined Drebrin expression in 21 day old cortical cultures containing astrocytes and neurons. As expected, Drebrin immunoreactivity was detected at high levels in dendritic spines of cortical neurons (Koganezawa et al., 2017) (Figure1A, upper panel**,** in Schiweck et al., 2021). In contrast, astrocytes in neuronal cultures did not express Drebrin at detectable levels. Likewise, when examining brain slices of adult mice, a strong signal for Drebrin was obtained in the cortex, originating from dendrities harboring harboring Map2+ dendrictic spines, whereas S100β-positive cortical astrocytes did not show any Drebrin expression (Figure 1C, upper panel in Schiweck et al., 2021).

In view of the substantial morphological and functional changes in astrocytes upon injury, we next asked whether Drebrin may be involved in astrogliosis responses. Therefore, we tested whether injury induces Drebrin expression in astrocytes. We took advantage of an *in vitro* scratch injury model to induce astrogliosis in cultured astrocytes and observed that astrocyte processes invading the scratch area in mixed cortical cultures displayed prominent Drebrin labelling (Figure 1A, lower panel, in Schiweck et al., 2021). In order to quantify the upregulation of Drebrin upon injury, we then subjected purified astrocyte cultures to injury and performed immunoblotting after different time points. Purified astrocytes expressed Drebrin at low basal levels at physiological conditions, which may be a result of culturing conditions that render these cells marginally reactive even in the absence of any acute injury stimulus (Foo et al., 2011). Nevertheless, purified astrocytes also showed a robust upregulation of Drebrin upon scratch injury, reaching a 3.2-fold increase as compared to basal levels after 24 hours (Figure 1B in Schiweck et al., 2021).

To study Drebrin in reactive astrocytes *in vivo*, we induced TBI in wild type or BAC Aldh1l1 eGFP reporter mice by inflicting a unilateral stab wound to the cortex and analyzing the tissue by immunohistochemistry. Usage of BAC Aldh1l1 eGFP reporter mice facilitated the visualization of both reactive and non-reactive astrocytes. The gray matter-restricted stab injury in the cortex resulted in astroglial scar formation at the injury site within 7 days. We observed strong Drebrin-labeling in GFAP+ astrocytes extending processes to the injury site, further confirming that Drebrin is also upregulated in astrocytes upon injury *in vivo* (Figure 1C, lower panel in Schiweck et al., 2021). These findings establish Drebrin as an injury-specific protein in reactive astrocytes.

4.2   Loss of Drebrin impairs glial scar formation

Given the upregulation of Drebrin upon injury, we next aimed to elucidate whether Drebrin plays a functional role in morphological rearrangements during astrogliosis.

We thus investigated the effect of Drebrin loss in glial scar formation *in vivo*. Cortical stab injuries in Drebrin-deficient mice revealed that astrocytes were able to induce their astrogliosis program, as prominent hypertrophy and GFAP immunoreactivity were observed in astrocytes surrounding the lesion area 7 days post injury. However, $Dbn^{-/-}$ astrocytes displayed defects in polarization. 45% of wild type astrocytes extended long processes to the injury site, whereas only ~ 16% of $Dbn^{-/-}$ astrocytes showed clear polarization (Figure 2A in Schiweck et al., 2021).

Since glial scar formation is a multicellular process, we next analyzed microglia, the first glia type to be recruited to the injury site. We studied IBA1+ microglia in the close vicinity of the injury site, which showed no or little signs of reactive hypertrophy in functional wild type scars. However, microglia in $Dbn^{-/-}$ mice showed hypertrophic cell bodies when compared to wild type mice (Figure 2B in Schiweck et al., 2021). This finding is indicative of defective scarring in injured $Dbn^{-/-}$ mouse brains. To assess whether the altered scar formation also affects surrounding neurons, we next assessed neuronal health at the injury site.

Induction of a stab injury usually generates limited tissue damage with loss of neurons restricted only to the needle insertion site in wild type brains. To assess the health of neurons surrounding the injury site, we studied the marker protein NeuN that localizes to both the cytoplasm and nuclei of healthy neurons. Cellular stress induces the translocation of NeuN from nuclei to cytoplasm (Lucas et al., 2014; Shandra et al., 2019; Wang et al., 2015). We used the translocation of NeuN as readout for neuronal stress and discovered a substantial number of neurons (42%) surrounding injury sites that displayed a translocation of NeuN from the nucleus to the cytoplasm in $Dbn^{-/-}$ brains. In wild type brains, only a neglectable proportion of cells showed this phenotype (~1%) (Figure 2C in Schiweck et

al., 2021). These findings demonstrate exacerbated neuronal stress in *Dbn*[^-/-] animals upon brain injury.

4.3 Drebrin is essential for maintaining of astrocyte reactivity and its loss causes extensive neurodegeneration

We next investigated the long-term consequences of Drebrin deficiency on glial scar formation and neuronal survival. To our surprise, glial scars, as measured by GFAP and Vimentin immunoreactivity, were absent at the needle insertion site in *Dbn*[^-/-] animals 30 days after injury, whereas wild type animals displayed astrocytic scars as expected (Figure 2D, S2A, B in Schiweck et al., 2021). In *Dbn*[^-/-] animals, the lack of scars was accompanied by exacerbated neurodegeneration adjacent to the injury site, quantified by counting of NeuN+ cells and Nissl staining. The number of NeuN+ cells around the lesion area revealed a drastic reduction of NeuN+ cells in *Dbn*[^-/-] animals. Nissl staining showed that neurons, normally identified by a bright violet stain of the large neuronal cell body, were absent from the injury site, while cells with dark, smaller nuclei were found, indicating the presence of non-neuronal cells at the injury site (Figure 2E, S4A in Schiweck et al., 2021).

Previous work in our group showed that loss of Drebrin in neurons leads to increased vulnerability upon cellular stress (Kreis et al., 2019). The *Dbn*[^-/-] mice used in this study are germline knockouts and consequently, Drebrin is deleted in all cells. To ensure that the observed excessive neuron degeneration was not due to increased neuronal vulnerability rather than astrocyte-dependent effects, we analyzed astrogliosis and neurodegeneration in *Dbn*[^fl/fl]*:CAMK-Cre*[^+/cre] (*Dbn*[^fl/fl]*:CAMK-Cre*) mice, which lose Drebrin specifically in neurons. *Dbn*[^fl/fl]*:CAMK-Cre*[^+/cre] (*Dbn*[^fl/fl]*:CAMK-Cre*) mice were comparable to wild type mice regarding astrocytic scar formation and did not show any signs of neuronal stress or neurodegeneration beyond the amount observed in wild type animals 7 and 30 days post injury (Figure 2E, S4C in Schiweck et al., 2021).

The absence of reactive astrocytes at the injury site in *Dbn*[^-/-] animals raised the question whether astrocytes simply downregulated their reactivity or whether they have vanished and other cell types are invading the area. We thus performed immunohistochemistry for a broad range of astrocytic markers, including Aldh1l1 and Sox9. Cells at the injury site expressed low levels of Aldh1l1, whereas an unusual pattern of Sox9 could be observed (Figure 2D, S3B in Schiweck et al., 2021).

Sox9 labeling in *Dbn*[^-/-] animals revealed large numbers of Sox9+ cells at the core lesion. Instead of displaying the typical nuclear Sox9 distribution, as observed in wild type animals, *Dbn*[^-/-] mice showed cells with an exclusively cytoplasmic Sox9 localization directly at the injury site. *Dbn*[^-/-] astrocytes distant to the core lesion showed the typical nuclear Sox9 distribution (FigureS3A in Schiweck et al., 2021). While nuclear Sox9 is astrocyte-specific in the adult mouse brain outside of neurogenic

regions (Sun et al., 2017), cytoplasmic Sox9 localization was previously described for undifferentiated stem cells as well as precursor cells. In conjunction with the downregulation of several astrocytic markers, this finding might therefore indicate de-differentiation of $Dbn^{-/-}$ astrocytes at the injury site, however, further investigation is required to correctly identify these cells.

We then investigated if the defects in glial scar formation and absence of astrocyte reactivity in $Dbn^{-/-}$ animals lead to the infiltration of invading monocytes. Appearance of monocytes in the lesion area and surrounding tissue would indicate compromised blood-brain barrier integrity. Immunostainings with CD45 revealed the presence of very few monocytes in both wild type and $Dbn^{-/-}$ animals, which were exclusively restricted to the needle insertion site (Figure S4B in Schiweck et al., 2021). Thus, increased monocyte invasion does not occur in the injured Drebrin-deficient brain. In summary, we showed the crucial role of Drebrin in maintaining astrocyte reactivity and neuronal survival after brain injury.

4.4   Drebrin localizes to structures beyond actin fibers *in vitro*

To further investigate the molecular mechanisms behind perturbed astrogliosis responses in Drebrin-deficient mice, we went back to purified astrocytes as a cell culture model and first established whether these astrocytes recapitulate the polarization defects observed *in vivo*.

Employing time lapse imaging in combination with scratch injury, we observed the polarization of astrocytes *in vitro* for 30 hours. $Dbn^{-/-}$ astrocyte monolayers showed impaired wound closure as compared to their wild type counterparts after 30 hours. In addition, lentivirally transduced astrocytes expressing the actin probe Lifeact-GFP showed that $Dbn^{-/-}$ cells extended over smaller distances and changed their orientation during scratch closure, while wild type astrocytes polarized in a coordinated and collective manner (Figure S5A, B). Thus, our cell culture assay recapitulated key features of Drebrin-dependent astrocyte scarring observed *in vivo*.

When we studied the subcellular distribution of Drebrin in these astrocytes after scratch injury, we observed time-dependent changes in protein localization: One hour after injury, Drebrin was mainly present at the actin-rich leading edge of cells. After 24 hours, Drebrin localized to more central parts of the extending processes. Overexpression of DBN-YFP together with labeling of F-Actin showed that Drebrin was only partially present on actin fibers and also labelled different cellular compartments, reminiscent of vesicular and tubular endosomal structures, suggesting that Drebrin might be involved in cellular trafficking processes (Figure S5 C, D in Schiweck et al., 2021).

4.5   Drebrin deficiency impairs Focal adhesions

We next asked whether the polarization defect observed in *Dbn*^{-/-} astrocytes *in vivo* may be due to impaired focal adhesion formation. Focal adhesions are multi-protein complexes, tethered to the actin cytoskeleton, which link cells to the extracellular matrix, and facilitate cell adhesion and movements (Kim & Wirtz, 2013). Astrocytes displaying defects in focal adhesion formation may therefore not be able to orient and extend their processes correctly towards the injury site.

We thus explored the focal adhesion proteins Paxillin and β1-Integrin in wild type and *Dbn*^{-/-} astrocytes employing live cell imaging, antibody feeding assays and immunocytochemistry. Observation of Paxillin-positive focal adhesions over time revealed a reduced focal adhesion size in *Dbn*^{-/-} cells. When we studied the distribution of β1-Integrin during injury-induced polarization, we observed long β1-Integrin-positive focal adhesions in wild type animals, whereas *Dbn*^{-/-} astrocytes showed a more scattered pattern of β1-Integrin at the membrane (Figure 5 B, C in Schiweck et al., 2021).

Malformation of focal adhesions can be caused by defects in focal adhesion assembly or due to impaired protein trafficking to focal adhesion sites. Given that Drebrin localized to vesicular and tubular endosomal compartments, we hypothesized that β1-Integrin trafficking is impaired in *Dbn*^{-/-} cells. Surface biotinylation experiments and antibody feeding assays revealed that *Dbn*^{-/-} cells had a substantially reduced amount of β1-Integrin on their surface compared to wild type astrocytes. In addition, internalized β1-Integrin appeared to accumulate just under the leading edge, whereas wild type cells displayed internalized β1-Integrin throughout the cell (Figure 5D, E in Schiweck et al., 2021).

In summary, Drebrin regulates β1-Integrin trafficking and focal adhesion formation in reactive astrocytes. These findings prompted us to ask how Drebrin could control membrane trafficking on the molecular level.

4.6   Injury-induced Rab8a- tubular endosomes formation is impaired in *Dbn*^{-/-}

With over 60 family members, Rab GTPases coordinate virtually all aspects of membrane trafficking in cells (Stenmark, 2009). Rab GTPases cycle between an 'active', GTP-bound form and an 'inactive' GDP-bound form. Different effector molecules, like kinases or phosphatases can be recruited by the active form and mediate different aspects of vesicle trafficking. Rab GTPases have roles in vesicle sorting, uncoating, motility, tethering and membrane fusion (Stenmark, 2009). Since Drebrin localized to vesicular structures and trafficking of β1-Integrin was disturbed in reactive *Dbn*^{-/-}

astrocytes, we explored if Rab family members displayed trafficking defects in *Dbn*^{-/-} cells. To this end, we expressed GFP-tagged Rabs involved at different steps of membrane trafficking in wild type and *Dbn*^{-/-} astrocytes after injury and compared their expression patterns. Rab5 (early endosome and phagosome-associated), Rab7 (late-endosome-associated) and Rab11 (recycling endosome-associated) did not show apparent difference between wild type and *Dbn*^{-/-} cells (Figure S6A in Schiweck et al., 2021). However, Rab8a, previously associated with trafficking from the *trans*-Golgi network (TGN) to the plasma membrane (Stenmark, 2009) as well as secretory autophagy (Dupont et al., 2011) showed a particular subcellular localization: GFP-Rab8a formed numerous prominent membrane tubules in wild type astrocytes, whereas the number of Rab8a membrane tubules was reduced in *Dbn*^{-/-} animals (Figure S6A in Schiweck et al., 2021). Quantification of GFP-Rab8a+ tubular endosomes was performed by extending a script previously developed to analyze tubular structures in cardiomyocytes, to be able to analyze data obtained during live cell imaging (Pasqualin et al., 2014).

Endogenous labeling of Rab8 confirmed the presence of tubular endosomes in wild type astrocytes after scratch injury, with tubules being most prominent in astrocytes invading the scratch area. When comparing differences between wild type and *Dbn*^{-/-} cells, we observed many more tubules in wild type cells, which extended throughout the cytosol. *Dbn*^{-/-} cells displayed less tubular endosomes that were mostly localized to the perinuclear region. (Figure 3A in Schiweck et al., 2021). We attempted to quantify endogenous tubule numbers in an automated manner, however, the determination of endogenous Rab8+ tubules was not feasible due to a low signal to noise ratio yielded with antibody labeling (Figure 3A in Schiweck et al., 2021).

Given that Rab8a has a different subcellular localization in injured wild type and *Dbn*^{-/-} astrocytes, we next asked whether this phenotype is correlated with astrogliosis or whether uninjured *Dbn*^{-/-} and wild type astrocytes display a similar phenotype.
We thus assessed Rab8a+ tubular endosome numbers in wild type and *Dbn*^{-/-} cells with and without injury. Indeed, under basal conditions, the number of Rab8+ tubular endosomes was very low and did not differ in wild type and *Dbn*^{-/-} astrocytes. However, wild type cells upregulated this compartment in response to injury whereas *Dbn*^{-/-} astrocytes failed to do so (Figure 3D, E in Schiweck et al., 2021). Since we also observed an upregulation of Drebrin in astrocytes upon injury, taken together these findings indicate a role for Drebrin in formation of the Rab8+ tubular compartment in response to injury.
One possibility of how Drebrin could influence Rab8+ tubular endosome formation is by directly affecting Rab8 protein levels. We thus asked whether total Rab8 protein levels are altered by the

lack of Drebrin. Immunoblotting showed that Rab8 total protein levels did not differ between wild type and *Dbn*^{-/-} astrocytes either with or without injury (Figure 3B in Schiweck et al., 2021). Since the active, GTP-bound form of Rab8 may be able to mediate tubule formation, we also analyzed whether wild type and *Dbn*^{-/-} astrocytes display different GTP-Rab8 levels in the presence of absence of injury. To this end, we employed a pulldown assay, using synaptotagmin-like protein 4, which preferentially binds GTP-Rab8 (Hampson et al., 2013) and found that GTP-Rab8 levels did not differ between wild type and *Dbn*^{-/-} astrocytes both with or without injury (Figure 3C in Schiweck et al., 2021).

Our findings suggest that Rab8a+ tubular endosomes are specifically induced in reactive astrocytes upon injury and that the role of Drebrin in the formation of Rab8+ tubular endosomes may be of structural nature rather than by influencing Rab8 protein levels, conceivably by cytoskeletal scaffolds that allow the formation of tubular Rab8+ endosomes.

4.7   Drebrin counteracts ARP2/3 activity to enable Rab8+ tubular endosome formation

To understand the role of Drebrin in tubular endosome formation, we next sought to rescue the phenotype in *Dbn*^{-/-} cells by different means. First, we expressed DBN-YFP in *Dbn*^{-/-} cells, which not only restored formation of tubular endosomes upon injury, but also revealed a localization of DBN to Rab8a+ tubular compartments (Figure 4A in Schiweck et al., 2021).

We next aimed to further study the role of Drebrin in mediating actin dynamics during membrane tubulation. To analyze the role of Drebrin in this process, we took a pharmacological approach and altered actin dynamics in injured *Dbn*^{-/-} astrocytes while monitoring the impact of different drugs on Rab8+ tubule formation. The small molecule inhibitor SMIFH2 inhibits formins, proteins that initiate actin filament nucleation and stay associated with the fast-growing filament end, where they act to accelerate filament elongation (Goode & Eck, 2007; Rizvi et al., 2009). Inhibition of formins by SMIFH2 showed no effect on Rab8+ tubule formation in *Dbn*^{-/-} cells, indicating that altered actin nucleation by formins does not underlie the lack of Rab8+ tubular endosomes.

Next we used cytochalasinD, an inhibitor that functionally resembles actin capping proteins and prevents filament polymerization and de-polymerization (Cooper, 1987), however, when used at low doses, cytochalasinD primarily inhibits Arp2/3 dependent actin polymerization (Rotty et al., 2015).. Treatment with low doses of cytochalasin D rapidly restored Rab8+ tubular endosomes in *Dbn*^{-/-} cells, indicating that actin branching is affected by the loss of Drebrin (Figure 4B in Schiweck et al., 2021). To further elucidate which specific actin-regulators are involved in the aberrant actin branching and impaired tubular endosome formation, we inhibited the ARP2/3 protein complex, which induces actin networks by enabling branching of new filaments from already existing filaments. Similar to cytochalasin D, treatment with the ARP2/3 inhibitor CK666 (Nolen et al., 2009) rescued Rab8+

tubular endosomes in *Dbn*$^{-/-}$ cells (Figure 4B in Schiweck et al., 2021). This data suggests that Drebrin mediates Rab8+ membrane tubulation by suppression of Arp2/3-dependent branched actin networks.

Rab8+ tubular endosome trafficking was previously shown to be dependent on both actin and microtubules and disruption of either of the two filaments systems interferes with tubule formation (Hattula et al., 2006). Thus, we hypothesized that Drebrin is important for establishing actin scaffolds that are compatible with microtubules and allow Rab8+tubular endosomes to change between initial stabilizing actin structures at the leading edge to microtubule networks.

Live cell imaging combining the visualization of microtubules, actin and Rab8 in wild type and *Dbn*$^{-/-}$ cells showed that microtubules were present at the actin-rich leading edge in wild type cells and Rab8+ tubular endosome readily extended along microtubules. In *Dbn*$^{-/-}$ cells, microtubules were present in vicinity to, but rarely extend into, the actin-rich area.

In addition, we observed Rab8+ membrane accumulations at the leading edge, but no Rab8+ tubules were formed. Upon treatment with the ARP2/3 inhibitor CK666, *Dbn*$^{-/-}$ cells immediately formed Rab8+ tubular endosomes, drawn from the accumulating Rab8+ membrane compartments at the leading edge, and extended along microtubules (Figure 4D in Schiweck et al., 2021). This indicates that Drebrin indeed acts to stabilize linear actin filaments and counteracts excessive ARP2/3-dependent actin branching, thereby promoting microtubule-compatible actin scaffolds that allow the formation of injury-induced Rab8+ tubular endosomes.

4.8   Rab8+ tubular endosomes mediate β1-Integrin trafficking

The accumulation of β1-Integrin at the leading edge observed in section 4.5 corresponds to our observations that Rab8a+ membrane structures accumulate at the leading edge in *Dbn*$^{-/-}$ cells. A double labeling for both proteins confirmed the presence of internalized β1-Integrin in Rab8+ tubular endosomes (Figure 5A in Schiweck et al., 2021). To verify the role of Rab8 in β1-Intergin trafficking, we employed siRNA-knockdown of Rab8a in wild type astrocytes in conjunction with an antibody feeding assay. Indeed, Rab8a knockdown mimicked the phenotype observed in *Dbn*$^{-/-}$ cells, as both accumulated internalized β1-Integrin underneath the leading edge. These results establish a role for Drebrin in facilitating Rab8-mediated transport of β1-Integrin (Figure 5E in Schiweck et al., 2021).

4.9   Drebrin deficiency leads to accumulation of multilamellar bodies in astrocytes *in vivo*

Since we observed a trafficking defect of β1-Integrin in injured Drebrin$^{-/-}$ astrocytes *in vitro*, we next asked whether such a trafficking defect could be observed *in vivo*. We first performed

immunohistochemistry to assess if Rab8+ tubular endosomes are present in astrocytes at the injury site *in vivo*. Wild type astrocytes displayed Rab8+ tubular structures, which were mainly localized to extending processes. *Dbn*^{-/-} astrocytes displayed a dispersed Rab8 signal in their processes and numerous small tubular and vesicular structures in cell bodies (Figure 3G in Schiweck et al., 2021). To verify the extent of this membrane trafficking defect, we employed high-resolution transmission electron microscopy (TEM) in brain slices and compared uninjured and injured cortical areas in wild type and *Dbn*^{-/-} animals 7 days after injury. Whereas no differences could be found between wild type and *Dbn*^{-/-} animals in the uninjured contralateral cortex, *Dbn*^{-/-} astrocyte processes were filled with extensive membrane accumulations resembling multilamellar bodies at the injury site (Hariri et al., 2000). In contrast, wild type animals surrounding the injury site displayed smaller, endosome like organelles frequently connected to tubular structures in astrocytic processes (Figure 6A, B in Schiweck et al., 2021). This apparent membrane trafficking phenotype induced upon injury in Drebrin deficient astrocytes is well in line with our results demonstrating that Drebrin plays a role during astrogliosis and mediates membrane trafficking of surface receptors, like β1-Integrin.

5. Discussion

The work presented here suggests a novel role for the actin-binding protein Drebrin during astrogliosis, summarized in **Figure 2**. Our study showed that (i) Drebrin is upregulated in astrocytes upon injury *in vitro* and *in vivo*; (ii) a lack of Drebrin causes defects in astroglial scar formation in the short term and interferes with maintenance of astrocyte reactivity in the long term, leading to exacerbated neurodegeneration in response to a mild injury model; (iii) Drebrin deficiency results in trafficking defects of focal adhesion proteins like β1-Integrin; (iv) Drebrin is necessary for the injury-induced formation of Rab8+ tubular endosomes which serve to traffic β1-Integrin; (v) Drebrin's role in forming Rab8+ tubular endosomes is based on counteracting the activity of the ARP2/3 complex, thereby allowing for invasion of microtubules into the leading edge and elongation of Rab8+ tubular endosomes along these microtubules; (vi) Last, we show that injury triggers abnormal accumulation of multilamellar bodies in Drebrin deficient astrocytes *in vivo*, further indicating an injury-induced membrane trafficking defect in *Dbn*^{-/-} astrocytes.
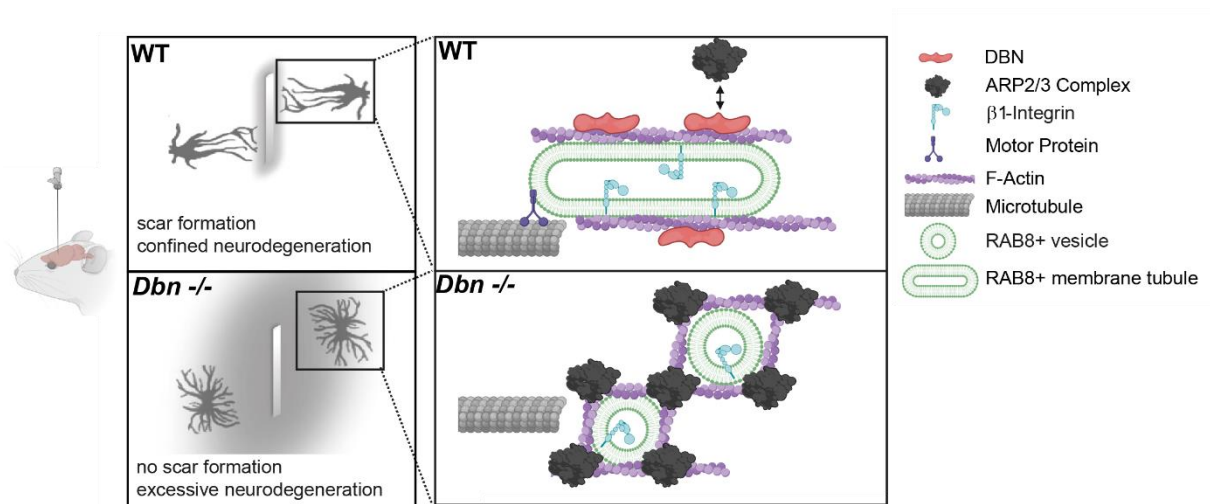
Figure 2. **The role of the Actin binding protein Drebrin during astrogliosis.** Adapted from Schiweck et al., 2021. Stab wound injury in the mouse brain induces defective scar formation in $Dbn^{-/-}$ animals and leads to excessive neurodegeneration. On the cellular level, Drebrin (DBN) counteracts Arp2/3 activity and thereby stabilizes actin filaments. The actin filaments then provide a scaffold for microtubules and facilitate injury-induced formation of Rab8 tubular endosomes and trafficking of surface receptors. In $Dbn^{-/-}$ animals, excessive Arp2/3 activity leads to branched filaments that impair tubule formation and surface receptor trafficking is impaired.

In conclusion, our study provides evidence for a conceptually new role for the actin-binding protein Drebrin during astrocytic scar formation and demonstrate the importance of Drebrin for injury-induced membrane trafficking.

5.1   Implications, potential clinical applications and limitations

Here, we observed an injury-induced upregulation of Drebrin protein levels in response to injury. Previously published transcriptome data corroborate this finding, since Drebrin transcripts were upregulated in astrocytes upon stab wound- or spinal cord injury: Astrogliosis occurs in response to a large variety of CNS pathologies, including stroke, inflammation or neurodegenerative diseases. Nevertheless, astrocytic changes in Drebrin levels seem to be associated with focal penetrating injuries and associated tissue damage in particular, as less pronounced increases in Drebrin mRNA were observed in response to a model of stroke or inflammation induced by lipopolysaccharide injections (Anderson et al., 2016; Sirko et al., 2015; Zamanian et al., 2012). Penetrating lesions require astrocytes to extend long protrusions towards the lesion area, a process that is associated with substantial cytoskeletal rearrangements, whereas LPS-induced inflammation induces astrogliosis, but does not require polarization of astrocytes towards one specific area (Schiweck et

al., 2018). This difference may explain why Drebrin is particularly upregulated in response to penetrating lesions.

Furthermore, we show that Drebrin is important for the polarization of astrocytes and maintenance of astrocyte reactivity *in vivo*. The impaired trafficking of β1-Integrin by Rab8+ tubular endosomes observed in our study not only provides a mechanism for polarization defects in $Dbn^{-/-}$ astrocytes, but also explains why they fail to maintain their reactivity.

Polarization of astrocytes relies on focal adhesions and interaction with the extracellular matrix (Schiweck et al., 2018). Our finding that focal adhesion size is reduced in Drebrin deficient astrocytes explains why these cells are not able to polarize normally. In addition, previous studies have shown that β1-Integrin functions as an important co-receptor that controls astrocyte reactivity (Hara et al., 2017; North et al., 2015; Robel et al., 2009). Impaired trafficking of β1-Integrin may therefore cause alterations of β1-Integrin-signaling and explain why $Dbn^{-/-}$ astrocytes loose GFAP+ reactivity after 30 days post injury.

Understanding central aspects of the molecular mechanisms involved in the astrogliosis response are valuable in a therapeutic context, as previous research has shown that the glial scar per se is neither only detrimental nor only beneficial (Bradbury & Burnside, 2019). Successful therapeutic approaches will take advantage of the beneficial aspects of astrogliosis while dampening its harmful effects. Our data emphasize the importance of initial astrocytic scar formation for preserving neuronal integrity. However, future approaches may consider targeting β-1Integrin during stages of tissue remodeling, providing the opportunity to resolve glial scars at stages where they hinder regeneration. Furthermore, Integrins have been studied extensively in neurons, where they are involved in spontaneous neuronal regeneration responses in the PNS and can be inactivated by axon-repulsive molecules at the lesion site of spinal cord injuries, thereby inhibiting axonal regeneration in the CNS (Nieuwenhuis et al., 2018). Thus, Integrins play a central role in nervous system injuries and understanding the effects of Integrin signaling in different cell types may provide valuable insights into nervous system recovery as well as potential therapeutic targets.

In addition, our findings implicate Drebrin in membrane trafficking and protein sorting by stabilization of Rab8+ tubular endosomes. Rab8 plays roles in endocytosis, membrane recycling, autophagy as well as exocytosis (Grigoriev et al., 2011; Ryan & Tumbarello, 2018) and is associated to different pathologies, like microvillar inclusion disease or neurodegenerative diseases (Peränen, 2011). The appearance of multilamellar bodies in Drebrin-deficient astrocytes upon injury supports our hypothesis of an injury-specific membrane trafficking defect in $Dbn^{-/-}$ astrocytes. Multilamellar bodies are associated with physiological lipid storage and secretion (Hariri et al., 2000), however, the lack of these structures in injured wild type astrocytes suggests that multilamellar bodies in $Dbn^{-/-}$ cells are a consequence of a pathological feature. Given that Rab8a was previously associated with

secretory autophagy (Dupont et al., 2011), the multilamellar bodies observed here may reflect defects in (secretory) autophagy. Further research on this association, could lead to novel therapeutic avenues targeting Rab8-dependent secretion.

One limitation of this study is the use of germline $Dbn^{-/-}$ mice to study astrocyte-specific processes after TBI. Given that transgenic mouse lines expressing constitutively active Cre recombinase under control of the truncated human GFAP, endogenous mouse GFAP or ALDH1L1 promoter also show gene ablations in some neurons and/or oligodendrocytes (Garcia et al., 2004; Tien et al., 2012; Zhuo et al., 2001), we employed a germline knockout of Drebrin and simultaneously verified that our effects are not caused by loss of Drebrin in neurons, which express Drebrin at high levels, by repeating crucial experiments in mice bearing a neuron-specific deletion of Drebrin. To further verify that the phenotype we observed is not caused by Drebrin deficiency in other cell types, we tested whether Drebrin is expressed by microglia. Microglia did not express any Drebrin *in vitro* and *in vivo*, however, we cannot rule out that other cells involved in the injury response are affected by the loss of Drebrin and may have contributed differently to the collective injury response as compared to wild type conditions in vivo. Nevertheless, our data obtained from purified astrocyte cultures suggests that the lack of DBN in astrocytes is a determinant of a functional astrogliosis response.

A further limitation is the usage of juvenile mice in this study. Stab wound injury was conducted on postnatal day 30, when mice are not yet sexually mature and are at the verge of being considered adults (Jackson et al., 2017). While a recent study reported that spinal cord injuries in animals at postnatal day 2 or 7 caused substantially different glial scars as compared to adult animals, mice injured at postnatal day 20 displayed scars similar to adults (Li et al., 2020). However, extrapolating the results of this study to fully mature adults or aged animals should be done with caution.

5.2 Further questions

The present study has raised several questions that are currently being addressed in our laboratory and in collaboration with other laboratories.

First, the molecular signaling pathways and mechanisms underlying the upregulation of Drebrin upon injury are unknown. Possible explanations of increased Drebrin levels include increased transcription as well as control of protein degradation by post-translational modifications and could provide further insights into the role of Drebrin in different cellular processes.

The second question is whether Drebrin also plays a role in other astrogliosis-related pathologies in the CNS, with a focus on SCI. Initial experiments involving immunohistochemistry of SCI tissue provided by our collaborators suggest that reactive astrocytes upregulate Drebrin protein levels upon SCI (data not shown), which is in line with the transcriptomic studies mentioned above.

Together with our collaborators, we are currently investigating if targeting Drebrin after SCI may have beneficial effects on glial scar formation and neuronal regeneration.

Another line of research initiated by this project addresses the appearance of cells with a cytoplasmic expression pattern of Sox9 at the injury site in $Dbn^{-/-}$ mice 30 days post injury. Whether these cells stem from an endogenous pool of neural stem or precursor cells, whether they are invading cells, like meningeal fibroblasts that may enter the brain upon disruptive brain injury (Komuta et al., 2010) or whether these cells are indeed de-differentiated astrocytes remains to be resolved and is currently being investigated.

In conclusion, the work presented in this study identifies a novel role for the actin-binding protein Drebrin during astrogliosis through modulation of actin scaffolds necessary for injury-induced membrane trafficking. This research is relevant in the context of traumatic CNS injury and initiated several further lines of research that may deepen our understanding of processes involved in astrogliosis and specificities of injury-related membrane trafficking.

References

Abd-El-Basset, E. M., & Fedoroff, S. (1997). Upregulation of F-actin and α-actinin in reactive astrocytes [https://doi.org/10.1002/(SICI)1097-4547(19970901)49:5<608::AID-JNR11>3.0.CO;2-R]. *Journal of Neuroscience Research*, *49*(5), 608-616. https://doi.org/https://doi.org/10.1002/(SICI)1097-4547(19970901)49:5<608::AID-JNR11>3.0.CO;2-R

Adams, K. L., & Gallo, V. (2018). The diversity and disparity of the glial scar. *Nat Neurosci*, *21*(1), 9-15. https://doi.org/10.1038/s41593-017-0033-9

Anderson, M. A., Ao, Y., & Sofroniew, M. V. (2014). Heterogeneity of reactive astrocytes. *Neurosci Lett*, *565*, 23-29. https://doi.org/10.1016/j.neulet.2013.12.030

Anderson, M. A., Burda, J. E., Ren, Y., Ao, Y., O'Shea, T. M., Kawaguchi, R., Coppola, G., Khakh, B. S., Deming, T. J., & Sofroniew, M. V. (2016). Astrocyte scar formation aids central nervous system axon regeneration. *Nature*, *532*(7598), 195-200. https://doi.org/10.1038/nature17623

Bardehle, S., Kruger, M., Buggenthin, F., Schwausch, J., Ninkovic, J., Clevers, H., Snippert, H. J., Theis, F. J., Meyer-Luehmann, M., Bechmann, I., Dimou, L., & Gotz, M. (2013). Live imaging of astrocyte responses to acute injury reveals selective juxtavascular proliferation. *Nat Neurosci*, *16*(5), 580-586. https://doi.org/10.1038/nn.3371

Boukhelifa, M., Hwang, S. J., Valtschanoff, J. G., Meeker, R. B., Rustioni, A., & Otey, C. A. (2003). A critical role for palladin in astrocyte morphology and response to injury. *Molecular and Cellular Neuroscience*, *23*(4), 661-668. https://doi.org/https://doi.org/10.1016/S1044-7431(03)00127-1

Bradbury, E. J., & Burnside, E. R. (2019). Moving beyond the glial scar for spinal cord repair. *Nat Commun*, *10*(1), 3879. https://doi.org/10.1038/s41467-019-11707-7

Breitsprecher, D., Kiesewetter, A. K., Linkner, J., Urbanke, C., Resch, G. P., Small, J. V., & Faix, J. (2008). Clustering of VASP actively drives processive, WH2 domain-mediated actin filament elongation. *The EMBO journal*, *27*(22), 2943-2954. https://doi.org/10.1038/emboj.2008.211

Burda, J. E., Bernstein, A. M., & Sofroniew, M. V. (2016). Astrocyte roles in traumatic brain injury. *Exp Neurol*, *275 Pt 3*, 305-315. https://doi.org/10.1016/j.expneurol.2015.03.020

Burda, J. E., & Sofroniew, M. V. (2014). Reactive gliosis and the multicellular response to CNS damage and disease. *Neuron*, *81*(2), 229-248. https://doi.org/10.1016/j.neuron.2013.12.034

Busch, S. A., & Silver, J. (2007). The role of extracellular matrix in CNS regeneration. *Current Opinion in Neurobiology*, *17*(1), 120-127. https://doi.org/https://doi.org/10.1016/j.conb.2006.09.004

Busch, S. A., & Silver, J. (2007). The role of extracellular matrix in CNS regeneration. *Curr Opin Neurobiol*, *17*(1), 120-127. https://doi.org/10.1016/j.conb.2006.09.004

Bushong, E. A., Martone, M. E., & Ellisman, M. H. (2004). Maturation of astrocyte morphology and the establishment of astrocyte domains during postnatal hippocampal development. *Int J Dev Neurosci*, *22*(2), 73-86. https://doi.org/10.1016/j.ijdevneu.2003.12.008

Butkevich, E., Hülsmann, S., Wenzel, D., Shirao, T., Duden, R., & Majoul, I. (2004). Drebrin Is a Novel Connexin-43 Binding Partner that Links Gap Junctions to the Submembrane Cytoskeleton. *Current Biology*, *14*(8), 650-658. https://doi.org/https://doi.org/10.1016/j.cub.2004.03.063

Chakrabarti, R., Lee, M., & Higgs, H. N. (2021). Multiple roles for actin in secretory and endocytic pathways. *Curr Biol*, *31*(10), R603-R618. https://doi.org/10.1016/j.cub.2021.03.038

Cooper, J. A. (1987). Effects of cytochalasin and phalloidin on actin. *J Cell Biol*, *105*(4), 1473-1478. https://doi.org/10.1083/jcb.105.4.1473

Courtine, G., & Sofroniew, M. V. (2019). Spinal cord repair: advances in biology and technology. *Nat Med*, *25*(6), 898-908. https://doi.org/10.1038/s41591-019-0475-6

Dupont, N., Jiang, S., Pilli, M., Ornatowski, W., Bhattacharya, D., & Deretic, V. (2011). Autophagy-based unconventional secretory pathway for extracellular delivery of IL-1β. *The EMBO journal*, *30*(23), 4701-4711. https://doi.org/10.1038/emboj.2011.398

Etienne-Manneville, S., & Hall, A. (2001). Integrin-Mediated Activation of Cdc42 Controls Cell Polarity in Migrating Astrocytes through PKCζ. *Cell*, *106*(4), 489-498. https://doi.org/https://doi.org/10.1016/S0092-8674(01)00471-8

Faulkner, J. R., Herrmann, J. E., Woo, M. J., Tansey, K. E., Doan, N. B., & Sofroniew, M. V. (2004). Reactive astrocytes protect tissue and preserve function after spinal cord injury. *J Neurosci*, *24*(9), 2143-2155. https://doi.org/10.1523/JNEUROSCI.3547-03.2004

Foo, L. C., Allen, N. J., Bushong, E. A., Ventura, P. B., Chung, W.-S., Zhou, L., Cahoy, J. D., Daneman, R., Zong, H., Ellisman, M. H., & Barres, B. A. (2011). Development of a method for the purification and culture of rodent astrocytes. *Neuron*, *71*(5), 799-811. https://doi.org/10.1016/j.neuron.2011.07.022

Frik, J., Merl-Pham, J., Plesnila, N., Mattugini, N., Kjell, J., Kraska, J., Gomez, R. M., Hauck, S. M., Sirko, S., & Gotz, M. (2018). Cross-talk between monocyte invasion and astrocyte proliferation regulates scarring in brain injury. *EMBO Rep*, *19*(5). https://doi.org/10.15252/embr.201745294

Gallop, J. L. (2020). Filopodia and their links with membrane traffic and cell adhesion. *Semin Cell Dev Biol*, *102*, 81-89. https://doi.org/10.1016/j.semcdb.2019.11.017

Garcia, A. D. R., Doan, N. B., Imura, T., Bush, T. G., & Sofroniew, M. V. (2004). GFAP-expressing progenitors are the principal source of constitutive neurogenesis in adult mouse forebrain. *Nature Neuroscience*, *7*(11), 1233-1241. https://doi.org/10.1038/nn1340

Goode, B. L., & Eck, M. J. (2007). Mechanism and Function of Formins in the Control of Actin Assembly. *Annual Review of Biochemistry*, *76*(1), 593-627. https://doi.org/10.1146/annurev.biochem.75.103004.142647

Grigoriev, I., Yu, Ka L., Martinez-Sanchez, E., Serra-Marques, A., Smal, I., Meijering, E., Demmers, J., Peränen, J., Pasterkamp, R. J., van der Sluijs, P., Hoogenraad, Casper C., & Akhmanova, A. (2011). Rab6, Rab8, and MICAL3 Cooperate in Controlling Docking and Fusion of Exocytotic Carriers. *Current Biology*, *21*(11), 967-974. https://doi.org/https://doi.org/10.1016/j.cub.2011.04.030

Hampson, A., O'Connor, A., & Smolenski, A. (2013). Synaptotagmin-like protein 4 and Rab8 interact and increase dense granule release in platelets [https://doi.org/10.1111/jth.12068]. *Journal of Thrombosis and Haemostasis*, *11*(1), 161-168. https://doi.org/https://doi.org/10.1111/jth.12068

Hansen, S. D., & Mullins, R. D. (2010). VASP is a processive actin polymerase that requires monomeric actin for barbed end association. *J Cell Biol*, *191*(3), 571-584. https://doi.org/10.1083/jcb.201003014

Hara, M., Kobayakawa, K., Ohkawa, Y., Kumamaru, H., Yokota, K., Saito, T., Kijima, K., Yoshizaki, S., Harimaya, K., Nakashima, Y., & Okada, S. (2017). Interaction of reactive astrocytes with type I collagen induces astrocytic scar formation through the integrin–N-cadherin pathway after spinal cord injury. *Nature Medicine*, *23*(7), 818-828. https://doi.org/10.1038/nm.4354

Hariri, M., Millane, G., Guimond, M. P., Guay, G., Dennis, J. W., & Nabi, I. R. (2000). Biogenesis of multilamellar bodies via autophagy. *Molecular biology of the cell*, *11*(1), 255-268. https://doi.org/10.1091/mbc.11.1.255

Hattula, K., Furuhjelm, J., Tikkanen, J., Tanhuanpää, K., Laakkonen, P., & Peränen, J. (2006). Characterization of the Rab8-specific membrane traffic route linked to protrusion formation. *Journal of Cell Science*, *119*(23), 4866-4877. https://doi.org/10.1242/jcs.03275

Hohmann, T., & Dehghani, F. (2019). The Cytoskeleton-A Complex Interacting Meshwork. *Cells*, *8*(4). https://doi.org/10.3390/cells8040362

Injury, G. B. D. T. B., & Spinal Cord Injury, C. (2019). Global, regional, and national burden of traumatic brain injury and spinal cord injury, 1990-2016: a systematic analysis for the Global Burden of Disease Study 2016. *Lancet Neurol*, *18*(1), 56-87. https://doi.org/10.1016/S1474-4422(18)30415-0

Jackson, S. J., Andrews, N., Ball, D., Bellantuono, I., Gray, J., Hachoumi, L., Holmes, A., Latcham, J., Petrie, A., Potter, P., Rice, A., Ritchie, A., Stewart, M., Strepka, C., Yeoman, M., & Chapman,

K. (2017). Does age matter? The impact of rodent age on study outcomes. *Laboratory animals*, *51*(2), 160-169. https://doi.org/10.1177/0023677216653984

Jara, J. S., Agger, S., & Hollis, E. R., 2nd. (2020). Functional Electrical Stimulation and the Modulation of the Axon Regeneration Program. *Front Cell Dev Biol*, *8*, 736. https://doi.org/10.3389/fcell.2020.00736

Jung, G., Kim, E.-J., Cicvaric, A., Sase, S., Gröger, M., Höger, H., Sialana, F. J., Berger, J., Monje, F. J., & Lubec, G. (2015). Drebrin depletion alters neurotransmitter receptor levels in protein complexes, dendritic spine morphogenesis and memory-related synaptic plasticity in the mouse hippocampus [https://doi.org/10.1111/jnc.13119]. *Journal of Neurochemistry*, *134*(2), 327-339. https://doi.org/https://doi.org/10.1111/jnc.13119

Kim, D.-H., & Wirtz, D. (2013). Focal adhesion size uniquely predicts cell migration. *FASEB journal : official publication of the Federation of American Societies for Experimental Biology*, *27*(4), 1351-1361. https://doi.org/10.1096/fj.12-220160

Koganezawa, N., Hanamura, K., Sekino, Y., & Shirao, T. (2017). The role of drebrin in dendritic spines. *Molecular and Cellular Neuroscience*, *84*, 85-92. https://doi.org/https://doi.org/10.1016/j.mcn.2017.01.004

Kojima, N., Yasuda, H., Hanamura, K., Ishizuka, Y., Sekino, Y., & Shirao, T. (2016). Drebrin A regulates hippocampal LTP and hippocampus-dependent fear learning in adult mice. *Neuroscience*, *324*, 218-226. https://doi.org/https://doi.org/10.1016/j.neuroscience.2016.03.015

Komuta, Y., Teng, X., Yanagisawa, H., Sango, K., Kawamura, K., & Kawano, H. (2010). Expression of Transforming Growth Factor-β Receptors in Meningeal Fibroblasts of the Injured Mouse Brain. *Cellular and Molecular Neurobiology*, *30*(1), 101-111. https://doi.org/10.1007/s10571-009-9435-x

Konietzny, A., Bar, J., & Mikhaylova, M. (2017). Dendritic Actin Cytoskeleton: Structure, Functions, and Regulations. *Front Cell Neurosci*, *11*, 147. https://doi.org/10.3389/fncel.2017.00147

Kreis, P., Gallrein, C., Rojas-Puente, E., Mack, T. G. A., Kroon, C., Dinkel, V., Willmes, C., Murk, K., Tom-Dieck, S., Schuman, E. M., Kirstein, J., & Eickholt, B. J. (2019). ATM phosphorylation of the actin-binding protein drebrin controls oxidation stress-resistance in mammalian neurons and C. elegans. *Nature communications*, *10*(1), 486-486. https://doi.org/10.1038/s41467-019-08420-w

Lasser, M., Tiber, J., & Lowery, L. A. (2018). The Role of the Microtubule Cytoskeleton in Neurodevelopmental Disorders [10.3389/fncel.2018.00165]. *Frontiers in Cellular Neuroscience*, *12*, 165. https://www.frontiersin.org/article/10.3389/fncel.2018.00165

Li, B., Ding, S., Feng, N., Mooney, N., Ooi, Y. S., Ren, L., Diep, J., Kelly, M. R., Yasukawa, L. L., Patton, J. T., Yamazaki, H., Shirao, T., Jackson, P. K., & Greenberg, H. B. (2017). Drebrin restricts rotavirus entry by inhibiting dynamin-mediated endocytosis. *Proceedings of the National Academy of Sciences*, *114*(18), E3642. https://doi.org/10.1073/pnas.1619266114

Li, Y., He, X., Kawaguchi, R., Zhang, Y., Wang, Q., Monavarfeshani, A., Yang, Z., Chen, B., Shi, Z., Meng, H., Zhou, S., Zhu, J., Jacobi, A., Swarup, V., Popovich, P. G., Geschwind, D. H., & He, Z. (2020). Microglia-organized scar-free spinal cord repair in neonatal mice. *Nature*, *587*(7835), 613-618. https://doi.org/10.1038/s41586-020-2795-6

Lucas, C.-H., Calvez, M., Babu, R., & Brown, A. (2014). Altered subcellular localization of the NeuN/Rbfox3 RNA splicing factor in HIV-associated neurocognitive disorders (HAND). *Neuroscience letters*, *558*, 97-102. https://doi.org/10.1016/j.neulet.2013.10.037

Mahar, M., & Cavalli, V. (2018). Intrinsic mechanisms of neuronal axon regeneration. *Nat Rev Neurosci*, *19*(6), 323-337. https://doi.org/10.1038/s41583-018-0001-8

Majoul, I., Shirao, T., Sekino, Y., & Duden, R. (2007). Many faces of drebrin: from building dendritic spines and stabilizing gap junctions to shaping neurite-like cell processes. *Histochem Cell Biol*, *127*(4), 355-361. https://doi.org/10.1007/s00418-007-0273-y

Menet, V., Prieto, M., Privat, A., & Giménez y Ribotta, M. (2003). Axonal plasticity and functional recovery after spinal cord injury in mice deficient in both glial fibrillary acidic protein and

vimentin genes. *Proceedings of the National Academy of Sciences of the United States of America*, *100*(15), 8999-9004. https://doi.org/10.1073/pnas.1533187100

Mikati, M. A., Grintsevich, E. E., & Reisler, E. (2013). Drebrin-induced stabilization of actin filaments. *The Journal of biological chemistry*, *288*(27), 19926-19938. https://doi.org/10.1074/jbc.M113.472647

Murk, K., Blanco Suarez, E. M., Cockbill, L. M. R., Banks, P., & Hanley, J. G. (2013). The antagonistic modulation of Arp2/3 activity by N-WASP, WAVE2 and PICK1 defines dynamic changes in astrocyte morphology. *Journal of Cell Science*, *126*(Pt 17), 3873-3883. https://doi.org/10.1242/jcs.125146

Nieuwenhuis, B., Haenzi, B., Andrews, M. R., Verhaagen, J., & Fawcett, J. W. (2018). Integrins promote axonal regeneration after injury of the nervous system. *Biological reviews of the Cambridge Philosophical Society*, *93*(3), 1339-1362. https://doi.org/10.1111/brv.12398

Nolen, B. J., Tomasevic, N., Russell, A., Pierce, D. W., Jia, Z., McCormick, C. D., Hartman, J., Sakowicz, R., & Pollard, T. D. (2009). Characterization of two classes of small molecule inhibitors of Arp2/3 complex. *Nature*, *460*(7258), 1031-1034. https://doi.org/10.1038/nature08231

North, H. A., Pan, L., McGuire, T. L., Brooker, S., & Kessler, J. A. (2015). β1-Integrin alters ependymal stem cell BMP receptor localization and attenuates astrogliosis after spinal cord injury. *The Journal of neuroscience : the official journal of the Society for Neuroscience*, *35*(9), 3725-3733. https://doi.org/10.1523/JNEUROSCI.4546-14.2015

Pasqualin, C., Gannier, F., Malécot, C. O., Bredeloux, P., & Maupoil, V. (2014). Automatic quantitative analysis of t-tubule organization in cardiac myocytes using ImageJ. *American Journal of Physiology-Cell Physiology*, *308*(3), C237-C245. https://doi.org/10.1152/ajpcell.00259.2014

Pekny, M. (2001). Astrocytic intermediate filaments: lessons from GFAP and vimentin knock-out mice. In *Progress in Brain Research* (Vol. 132, pp. 23-30). Elsevier. https://doi.org/https://doi.org/10.1016/S0079-6123(01)32062-9

Peränen, J. (2011). Rab8 GTPase as a regulator of cell shape [https://doi.org/10.1002/cm.20529]. *Cytoskeleton*, *68*(10), 527-539. https://doi.org/https://doi.org/10.1002/cm.20529

Pollard, T. D. (2007). Regulation of actin filament assembly by Arp2/3 complex and formins. *Annu Rev Biophys Biomol Struct*, *36*, 451-477. https://doi.org/10.1146/annurev.biophys.35.040405.101936

Pollard, T. D., & Cooper, J. A. (2009). Actin, a central player in cell shape and movement. *Science (New York, N.Y.)*, *326*(5957), 1208-1212. https://doi.org/10.1126/science.1175862

Rizvi, S. A., Neidt, E. M., Cui, J., Feiger, Z., Skau, C. T., Gardel, M. L., Kozmin, S. A., & Kovar, D. R. (2009). Identification and characterization of a small molecule inhibitor of formin-mediated actin assembly. *Chemistry & biology*, *16*(11), 1158-1168. https://doi.org/10.1016/j.chembiol.2009.10.006

Robel, S., Bardehle, S., Lepier, A., Brakebusch, C., & Gotz, M. (2011). Genetic deletion of cdc42 reveals a crucial role for astrocyte recruitment to the injury site in vitro and in vivo. *J Neurosci*, *31*(35), 12471-12482. https://doi.org/10.1523/JNEUROSCI.2696-11.2011

Robel, S., Mori, T., Zoubaa, S., Schlegel, J., Sirko, S., Faissner, A., Goebbels, S., Dimou, L., & Gotz, M. (2009). Conditional deletion of beta1-integrin in astroglia causes partial reactive gliosis. *Glia*, *57*(15), 1630-1647. https://doi.org/10.1002/glia.20876

Romero, S., Didry, D., Larquet, E., Boisset, N., Pantaloni, D., & Carlier, M. F. (2007). How ATP hydrolysis controls filament assembly from profilin-actin: implication for formin processivity. *The Journal of biological chemistry*, *282*(11), 8435-8445. https://doi.org/10.1074/jbc.M609886200

Rotty, J. D., & Bear, J. E. (2014). Competition and collaboration between different actin assembly pathways allows for homeostatic control of the actin cytoskeleton. *Bioarchitecture*, *5*(1-2), 27-34. https://doi.org/10.1080/19490992.2015.1090670

Rotty, J. D., Wu, C., Haynes, E. M., Suarez, C., Winkelman, J. D., Johnson, H. E., Haugh, J. M., Kovar, D. R., & Bear, J. E. (2015). Profilin-1 serves as a gatekeeper for actin assembly by Arp2/3-

dependent and -independent pathways. *Developmental cell*, *32*(1), 54-67. https://doi.org/10.1016/j.devcel.2014.10.026

Ruschel, J., & Bradke, F. (2018). Systemic administration of epothilone D improves functional recovery of walking after rat spinal cord contusion injury. *Exp Neurol*, *306*, 243-249. https://doi.org/10.1016/j.expneurol.2017.12.001

Ryan, T. A., & Tumbarello, D. A. (2018). Optineurin: A Coordinator of Membrane-Associated Cargo Trafficking and Autophagy. *Frontiers in immunology*, *9*, 1024-1024. https://doi.org/10.3389/fimmu.2018.01024

Santello, M., Toni, N., & Volterra, A. (2019). Astrocyte function from information processing to cognition and cognitive impairment. *Nat Neurosci*, *22*(2), 154-166. https://doi.org/10.1038/s41593-018-0325-8

Schiweck, J., Eickholt, B. J., & Murk, K. (2018). Important Shapeshifter: Mechanisms Allowing Astrocytes to Respond to the Changing Nervous System During Development, Injury and Disease. *Front Cell Neurosci*, *12*, 261. https://doi.org/10.3389/fncel.2018.00261

Schiweck, J., Murk, K., Ledderose, J., Munster-Wandowski, A., Ornaghi, M., Vida, I., & Eickholt, B. J. (2021). Drebrin controls scar formation and astrocyte reactivity upon traumatic brain injury by regulating membrane trafficking. *Nat Commun*, *12*(1), 1490. https://doi.org/10.1038/s41467-021-21662-x

Schrötter, S., Leondaritis, G., & Eickholt, B. J. (2016). Capillary Isoelectric Focusing of Akt Isoforms Identifies Highly Dynamic Phosphorylation in Neuronal Cells and Brain Tissue. *The Journal of biological chemistry*, *291*(19), 10239-10251. https://doi.org/10.1074/jbc.M115.700138

Shandra, O., Winemiller, A. R., Heithoff, B. P., Munoz-Ballester, C., George, K. K., Benko, M. J., Zuidhoek, I. A., Besser, M. N., Curley, D. E., Edwards, G. F., 3rd, Mey, A., Harrington, A. N., Kitchen, J. P., & Robel, S. (2019). Repetitive Diffuse Mild Traumatic Brain Injury Causes an Atypical Astrocyte Response and Spontaneous Recurrent Seizures. *The Journal of neuroscience : the official journal of the Society for Neuroscience*, *39*(10), 1944-1963. https://doi.org/10.1523/JNEUROSCI.1067-18.2018

Shirao, T., Hanamura, K., Koganezawa, N., Ishizuka, Y., Yamazaki, H., & Sekino, Y. (2017). The role of drebrin in neurons [https://doi.org/10.1111/jnc.13988]. *Journal of Neurochemistry*, *141*(6), 819-834. https://doi.org/https://doi.org/10.1111/jnc.13988

Silver, J., & Miller, J. H. (2004). Regeneration beyond the glial scar. *Nat Rev Neurosci*, *5*(2), 146-156. https://doi.org/10.1038/nrn1326

Sirko, S., Irmler, M., Gascón, S., Bek, S., Schneider, S., Dimou, L., Obermann, J., De Souza Paiva, D., Poirier, F., Beckers, J., Hauck, S. M., Barde, Y.-A., & Götz, M. (2015). Astrocyte reactivity after brain injury-: The role of galectins 1 and 3. *Glia*, *63*(12), 2340-2361. https://doi.org/10.1002/glia.22898

Sofroniew, M. V. (2009). Molecular dissection of reactive astrogliosis and glial scar formation. *Trends Neurosci*, *32*(12), 638-647. https://doi.org/10.1016/j.tins.2009.08.002

Sofroniew, M. V. (2014). Astrogliosis. *Cold Spring Harb Perspect Biol*, *7*(2), a020420. https://doi.org/10.1101/cshperspect.a020420

Sofroniew, M. V. (2015). Astrocyte barriers to neurotoxic inflammation. *Nat Rev Neurosci*, *16*(5), 249-263. https://doi.org/10.1038/nrn3898

Stenmark, H. (2009). Rab GTPases as coordinators of vesicle traffic. *Nature Reviews Molecular Cell Biology*, *10*(8), 513-525. https://doi.org/10.1038/nrm2728

Stroncek, J. D., & Reichert, W. M. (2008). Overview of Wound Healing in Different Tissue Types. In W. M. Reichert (Ed.), *Indwelling Neural Implants: Strategies for Contending with the In Vivo Environment*. https://www.ncbi.nlm.nih.gov/pubmed/21204404

Sultana, S., Sernett, S. W., Bellin, R. M., Robson, R. M., & Skalli, O. (2000). Intermediate filament protein synemin is transiently expressed in a subset of astrocytes during development. *Glia*, *30*(2), 143-153. https://doi.org/10.1002/(sici)1098-1136(200004)30:2<143::aid-glia4>3.0.co;2-z

Sun, W., Cornwell, A., Li, J., Peng, S., Osorio, M. J., Aalling, N., Wang, S., Benraiss, A., Lou, N., Goldman, S. A., & Nedergaard, M. (2017). SOX9 Is an Astrocyte-Specific Nuclear Marker in the Adult Brain Outside the Neurogenic Regions. *The Journal of Neuroscience*, *37*(17), 4493. https://doi.org/10.1523/JNEUROSCI.3199-16.2017

Tam, R. Y., Fuehrmann, T., Mitrousis, N., & Shoichet, M. S. (2014). Regenerative therapies for central nervous system diseases: a biomaterials approach. *Neuropsychopharmacology*, *39*(1), 169-188. https://doi.org/10.1038/npp.2013.237

Tien, A.-C., Tsai, H.-H., Molofsky, A. V., McMahon, M., Foo, L. C., Kaul, A., Dougherty, J. D., Heintz, N., Gutmann, D. H., Barres, B. A., & Rowitch, D. H. (2012). Regulated temporal-spatial astrocyte precursor cell proliferation involves BRAF signalling in mammalian spinal cord. *Development (Cambridge, England)*, *139*(14), 2477-2487. https://doi.org/10.1242/dev.077214

Vainchtein, I. D., & Molofsky, A. V. (2020). Astrocytes and Microglia: In Sickness and in Health. *Trends Neurosci*, *43*(3), 144-154. https://doi.org/10.1016/j.tins.2020.01.003

Wang, J., Jahn-Eimermacher, A., Brückner, M., Werner, C., Engelhard, K., & Thal, S. C. (2015). Comparison of different quantification methods to determine hippocampal damage after cerebral ischemia. *Journal of Neuroscience Methods*, *240*, 67-76. https://doi.org/https://doi.org/10.1016/j.jneumeth.2014.11.001

Willmes, C. G., Mack, T. G. A., Ledderose, J., Schmitz, D., Wozny, C., & Eickholt, B. J. (2017). Investigation of hippocampal synaptic transmission and plasticity in mice deficient in the actin-binding protein Drebrin. *Scientific Reports*, *7*(1), 42652. https://doi.org/10.1038/srep42652

Yang, T., Dai, Y., Chen, G., & Cui, S. (2020). Dissecting the Dual Role of the Glial Scar and Scar-Forming Astrocytes in Spinal Cord Injury. *Front Cell Neurosci*, *14*, 78. https://doi.org/10.3389/fncel.2020.00078

Yang, Y., Vidensky, S., Jin, L., Jie, C., Lorenzini, I., Frankl, M., & Rothstein, J. D. (2011). Molecular comparison of GLT1+ and ALDH1L1+ astrocytes in vivo in astroglial reporter mice. *Glia*, *59*(2), 200-207. https://doi.org/10.1002/glia.21089

Zamanian, J. L., Xu, L., Foo, L. C., Nouri, N., Zhou, L., Giffard, R. G., & Barres, B. A. (2012). Genomic Analysis of Reactive Astrogliosis. *The Journal of Neuroscience*, *32*(18), 6391. https://doi.org/10.1523/JNEUROSCI.6221-11.2012

Zhuo, L., Theis, M., Alvarez-Maya, I., Brenner, M., Willecke, K., & Messing, A. (2001). hGFAP-cre transgenic mice for manipulation of glial and neuronal function in vivo. *Genesis*, *31*(2), 85-94. https://doi.org/10.1002/gene.10008

Statutory Declaration

"I, Juliane Schiweck, by personally signing this document in lieu of an oath, hereby affirm that I prepared the submitted dissertation on the topic 'The role of the actin-binding-protein Drebrin in astrocytic scar formation upon traumatic brain injury'/'Die Rolle des Aktin-bindenden Proteins Drebrin während der astrozytären Narbenbildung nach traumatischer Gehirnverletzung', independently and without the support of third parties, and that I used no other sources and aids than those stated.

All parts which are based on the publications or presentations of other authors, either in letter or in spirit, are specified as such in accordance with the citing guidelines. The sections on methodology (in particular regarding practical work, laboratory regulations, statistical processing) and results (in particular regarding figures, charts and tables) are exclusively my responsibility.

Furthermore, I declare that I have correctly marked all of the data, the analyses, and the conclusions generated from data obtained in collaboration with other persons, and that I have correctly marked my own contribution and the contributions of other persons (cf. declaration of contribution). I have correctly marked all texts or parts of texts that were generated in collaboration with other persons.

My contributions to any publications to this dissertation correspond to those stated in the below joint declaration made together with the supervisor. All publications created within the scope of the dissertation comply with the guidelines of the ICMJE (International Committee of Medical Journal Editors; www.icmje.org) on authorship. In addition, I declare that I shall comply with the regulations of Charité – Universitätsmedizin Berlin on ensuring good scientific practice.

I declare that I have not yet submitted this dissertation in identical or similar form to another Faculty.

The significance of this statutory declaration and the consequences of a false statutory declaration under criminal law (Sections 156, 161 of the German Criminal Code) are known to me."

28.09.2021

Date   Signature

Juliane Schiweck contributed the following to the below listed publication [contributions highlighted in dark blue]:

Schiweck, J., Murk, K., Ledderose, J., Munster-Wandowski, A., Ornaghi, M., Vida, I., & Eickholt, B. J. (2021). Drebrin controls scar formation and astrocyte reactivity upon traumatic brain injury by regulating membrane trafficking. Nat Commun, 12(1), 1490

Figure 1A: cell culture, immunocytochemistry (ICC), microscopy, analysis by Dr. Kai Murk
Figure 1B: cell culture, sample preparation, immunoblotting, analysis by Dr. Kai Murk
Figure 1C: (upper panel): tissue collection, immunohistochemistry, microscopy, analysis by Dr. Kai Murk; (lower panel); immunohistochemistry, microscopy, analysis by Juliane Schiweck

Figure 2A: animal experiments by Dr. Julia Ledderose; immunohistochemistry (IHC), microscopy, analysis by Dr. Kai Murk
Figure2 B: animal experiments by Dr. Julia Ledderose; IHC, microscopy, analysis by Dr. Kai Murk
Figure2 C: animal experiments by Dr. Julia Ledderose; IHC, microscopy, analysis by Dr. Kai Murk
Figure2 D: animal experiments, tissue collection, IHC, microscopy and analysis by Juliane Schiweck
Figure2E: animal experiments, tissue collection, IHC, microscopy, analysis by Juliane Schiweck

Figure 3A: cell culture, ICC, microscopy, analysis by Juliane Schiweck
Figure 3B: cell culture, sample preparation, immunoblotting, analysis by Juliane Schiweck
Figure 3B: production of recombinant protein, cell culture, sample preparation, pull-down, immunoblotting, analysis by Juliane Schiweck
Figure 3D: cell culture, plasmid-transfection, time-lapse live cell imaging, analysis by Juliane Schiweck
Figure 3E: augmentation of FIJI plugin for time-lapse imaging, analysis by Juliane Schiweck
Figure 3F: cell culture, ICC, analysis by Dr. Kai Murk
Figure 3G: animal experiments, tissue collection, IHC, microscopy, analysis by Juliane Schiweck

Figure 4A: cell culture, plasmid transfection, microscopy, analysis by Juliane Schiweck
Figure 4B: cell culture, plasmid transfection, time-lapse live cell imaging, inhibitor treatment, analysis by Juliane Schiweck
Figure 4C: cell culture, ICC, microscopy, analysis by Juliane Schiweck
Figure 4D: cell culture, plasmid transfection and labeling, inhibitor treatment, time-lapse imaging, analysis by Dr. Kai Murk
Figure 4E: cartoon design by Kai Murk and Juliane Schiweck

Figure 5A: cell culture, ICC, microscopy, analysis by Juliane Schiweck
Figure 5B: cell culture, ICC, microscopy, analysis by Kai Murk and Juliane Schiweck
Figure 5C: cell culture, plasmid transfection, time-lapse imaging, analysis by Juliane Schiweck
Figure 5D: cell culture, biotinylation, pulldown, immunoblotting, analysis by Juliane Schiweck
Figure 5E: analysis by Kai Murk; cell culture, siRNA knockdown, antibody feeding, fixation, microscopy by Juliane Schiweck

Figure 6A: animal experiments, tissue preparation, IHC by Juliane Schiweck; TEM by Dr. Agnieszka Münster-Wandowski; data analysis by Kai Murk
Figure 6B: animal experiments, tissue preparation, IHC by Juliane Schiweck; TEM by Dr. Agnieszka Münster-Wandowski; data analysis by Kai Murk

Figure 7: design of the cartoon by Kai Murk and Juliane Schiweck, implementation by Juliane Schiweck

Figure S1A: cell culture, ICC, microscopy, analysis by Dr. Kai Murk
Figure S1B: tissue preparation, IHC, microscopy, analysis by Kai Murk and Juliane Schiweck
Figure S1C: cell culture, IHC, microscopy, analysis by Dr. Kai Murk
Figure S1D: animal experiments, tissue collection by Dr. Julia Ledderose; IHC, microscopy, analysis by Dr. Kai Murk

Figure S2A: animal experiments, tissue collection, IHC, microscopy, analysis by Juliane Schiweck
FigureS2B: animal experiments, tissue collection, IHC, microscopy, analysis by Juliane Schiweck

Figure S3A: animal experiments, tissue collection, IHC, microscopy, analysis by Juliane Schiweck
Figure S3B: animal experiments, tissue collection, IHC, microscopy, analysis by Juliane Schiweck

Figure S4A: animal experiments, tissue collection by Juliane Schiweck; IHC, microscopy, analysis by Marta Ornaghi and Juliane Schiweck
Figure S4B: animal experiments, tissue collection, IHC, microscopy, analysis by Juliane Schiweck
Figure S4C: animal experiments, tissue collection, IHC, microscopy, analysis by Juliane Schiweck

Figure S5A: cell culture, virus preparation, time-lapse imaging, analysis by Dr. Kai Murk
Figure S5B: cell culture, time-lapse imaging, analysis by Juliane Schiweck
Figure S5C: cell culture, IHC, microscopy, analysis by Dr.Kai Murk
Figure S5D: cell culture, IHC, microscopy, analysis by Dr.Kai Murk

Figure S6A: cell culture, plasmid transfection, microscopy, analysis by Juliane Schiweck
Figure S6B: cell culture, siRNA knockdown, ICC, microscopy, analysis by Juliane Schiweck
Figure S6C: cell culture, siRNA knockdown, immunoblotting, analysis by Juliane Schiweck

FigureS7A: cell culture, stimulation, time-lapse imaging, analysis by Juliane Schiweck
Figure S7B: animal experiments, tissue collection by Juliane Schiweck, TEM by Dr. Agnieszka Münster-Wandowski; analysis by Kai Murk

The figures in the manuscript were created by Dr. Kai Murk and Juliane Schiweck. The manuscript was written and edited by Dr. Kai Murk, Juliane Schiweck and Prof. Dr. Britta Eickholt. All authors read and revised the manuscript.

_____

Signature, date and stamp of first supervising university professor / lecturer
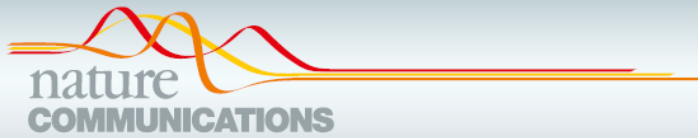
_____

Signature of doctoral candidate

Extract from the Journal Summary List ISI Web of KnowledgeSM

Journal Data Filtered By: **Selected JCR Year: 2019** Selected Editions: SCIE,SSCI
Selected Categories: **"MULTIDISCIPLINARY SCIENCES"** Selected Category
Scheme: WoS
Gesamtanzahl: 71 Journale

Rank	Full Journal Title	Total Cites	Journal Impact Factor	Eigenfactor Score
1	NATURE	767,209	42.778	1.216730
2	SCIENCE	699,842	41.845	1.022660
3	National Science Review	2,775	16.693	0.009760
4	Science Advances	36,380	13.116	0.172060
5	Nature Human Behaviour	2,457	12.282	0.014190
6	Nature Communications	312,599	12.121	1.259510
7	Science Bulletin	5,172	9.511	0.014150
8	PROCEEDINGS OF THE NATIONAL ACADEMY OF SCIENCES OF THE UNITED STATES OF AMERICA	676,425	9.412	0.931890
9	Journal of Advanced Research	3,564	6.992	0.005470
10	GigaScience	4,068	5.993	0.016410
11	Scientific Data	5,761	5.541	0.028720
12	Research Synthesis Methods	2,572	5.299	0.006440
13	ANNALS OF THE NEW YORK ACADEMY OF SCIENCES	45,596	4.728	0.026370
14	FRACTALS-COMPLEX GEOMETRY PATTERNS AND SCALING IN NATURE AND SOCIETY	2,156	4.536	0.002210
15	iScience	1,410	4.447	0.004140
16	GLOBAL CHALLENGES	481	4.306	0.001440
17	Scientific Reports	386,848	3.998	1.231180
18	JOURNAL OF KING SAUD UNIVERSITY SCIENCE	1,640	3.819	0.002020
19	Journal of the Royal Society Interface	13,762	3.748	0.027670

Selected JCR Year: 2019; Selected Categories: "MULTIDISCIPLINARY SCIENCES"

Publication

ARTICLE

Check for updates

Drebrin controls scar formation and astrocyte reactivity upon traumatic brain injury by regulating membrane trafficking

Juliane Schiweck [1,4], Kai Murk [1,4✉], Julia Ledderose[1], Agnieszka Münster-Wandowski[2], Marta Ornaghi[1], Imre Vida [2] & Britta J. Eickholt [1,3✉]

The brain of mammals lacks a significant ability to regenerate neurons and is thus particularly vulnerable. To protect the brain from injury and disease, damage control by astrocytes through astrogliosis and scar formation is vital. Here, we show that brain injury in mice triggers an immediate upregulation of the actin-binding protein Drebrin (DBN) in astrocytes, which is essential for scar formation and maintenance of astrocyte reactivity. In turn, DBN loss leads to defective astrocyte scar formation and excessive neurodegeneration following brain injuries. At the cellular level, we show that DBN switches actin homeostasis from ARP2/3-dependent arrays to microtubule-compatible scaffolds, facilitating the formation of RAB8-positive membrane tubules. This injury-specific RAB8 membrane compartment serves as hub for the trafficking of surface proteins involved in astrogliosis and adhesion mediators, such as β1-integrin. Our work shows that DBN-mediated membrane trafficking in astrocytes is an important neuroprotective mechanism following traumatic brain injury in mice.

[1] Institute of Biochemistry, Charité - Universitätsmedizin Berlin, Berlin, Germany. [2] Institute of Anatomy, Charité - Universitätsmedizin Berlin, Berlin, Germany. [3] NeuroCure - Cluster of Excellence, Charité - Universitätsmedizin Berlin, Berlin, Germany. [4] These authors contributed equally: Juliane Schiweck, Kai Murk. ✉email: kai.murk@charite.de; britta.eickholt@charite.de

The brain of higher mammals is vulnerable to traumatic injury and disease, but largely lacks the capacity to regenerate neurons and rarely regains function in damaged areas[1]. This makes the containment of local pathological incidents critical to avoid the propagation of inflammation and neurodegeneration into the uninjured brain parenchyma.

Astrocytes are key players in the protection of CNS tissue via a defense mechanism known as reactive astrogliosis. This process is associated with comprehensive changes in astrocyte morphology and function[2]. Reactive astrocytes develop hypertrophies of soma and protrusions, while cells in proximity to large lesion sites polarize and extend particularly long processes. Dense arrays of such "palisades" and hypertrophic astrocytes constitute scars, which enclose as physical barriers inflammatory cues and extravasating leukocytes, and limit the spread of damage[3,4]. Astrocyte scars are well described anatomically and with respect to certain signaling events[5], but little is known about molecular mechanisms controlling the cytoskeletal organization during polarization and outgrowth of palisade-like astrocyte processes.

In the context of astrogliosis and scar formation, we studied drebrin (DBN), a cytoskeletal regulator, which stabilizes actin filaments by sidewise binding and by competing off other actin-binding proteins[6,7]. It is widely expressed, but has mainly been studied in neurons[8]. In cultured astrocytes, DBN has been described to maintain connexin 43 at the plasma membrane[9]. Functional coupling of astrocytes into networks through gap junctions is essential to modulate neuronal transmission[10,11]. A deficit in DBN would therefore be expected to cause profound phenotypes in vivo. However, mouse models with acute or chronic DBN loss indicate non-essential functions of this actin-binding protein during neuronal development, as well as during synaptic transmission and plasticity[12]. Instead, we identified DBN as important local safeguard mechanism in dendritic spines during conditions associated with increased oxidative stress[13]. Here, we characterize DBN as an injury-specific actin regulator in astrocytes, crucial for the wounding response and tissue protection in the brain. During injury, DBN provides a key switch to alter actin network homeostasis, which prepares the foundation for tubular endosomes, enabling polarized membrane trafficking of crucial surface receptors. In this role, DBN controls reactive astrogliosis required to form astrocyte scars and to protect the susceptible CNS from traumatic brain injury.

Results

DBN is an injury-induced protein in reactive astrocytes. To investigate endogenous DBN protein expression in astrocytes, we performed immunocytochemistry in 21 days in vitro (DIV) cortical cultures from mice containing both neurons and astrocytes. Although we did not detect any DBN signals in astrocytes, high DBN levels were found in dendritic spines of neighboring neurons (Fig. 1A). We exploited an in vitro scratch-wound model to induce astrocyte reactivity, which increased DBN expression with prominent labeling along the astrocyte processes (Fig. 1A). In purified astrocyte cultures, where cells adopt polygonal morphologies, antibody labeling, and western blot analyses identified low DBN expression (Fig. 1B, S1A). Following mechanical scratch injury, DBN protein levels were increased, reaching 3.2-fold of the baseline level 24 h post injury (Fig. 1B).

In the mouse brain, DBN was distributed in distinct puncta in proximity to MAP2-positive dendrites, but not in S100ß+ astrocytes (Figures S1B). To induce reactive astrogliosis, we used an in vivo model for CNS trauma and inserted a needle unilaterally into the cortex of BAC Aldh1l1 eGFP reporter mice[14]. Seven days after this "stab injury", eGFP expression allowed us to visualize astrocytes independently of their quiescent or reactive status, while GFAP-labeled reactive astrocytes could be identified within the forming scar around the lesion site. After this stab injury, numerous injury-induced GFAP+ astrocytes exhibited DBN protein expression throughout their polarizing processes (Fig. 1, S1B, Movie 1). In summary, our results demonstrate that CNS injury triggers an immediate upregulation of DBN in astrocytes in vitro and in vivo.

Reactive astrocytes require DBN to form glia scars in vivo. To investigate if injury-induced upregulation of DBN protein is required during astrogliosis responses in vivo, we looked at its functional significance in DBN knockout mice during scar formation following cortical stab-injuries[12]. At 7 days post injury, the stab wound triggered the formation of long palisading processes extending toward the injury site in 45% of GFAP-positive astrocytes in WT brains, in line with previous studies[3,15,16]. In contrast, in $Dbn^{-/-}$ mice, GFAP-positive astrocytes showed strong defects in polarization and in the formation of palisade-like barriers (Fig. 2A).

Next, we addressed whether the defect in scarring induced by DBN-loss affects the surrounding tissue. Microglia are highly sensitive sentinels in the brain, which become hypertrophic phagocytic cells after injury[17]. Although cultured microglia, as well as microglia in intact and injured brains do not express DBN (Figures S1C, D), they respond to injury with increased hypertrophy in $Dbn^{-/-}$ brains when compared with WT brains (Fig. 2B). This result indicates that stab injury in $Dbn^{-/-}$ brains exacerbate microglial responses, which likely reflects defective scarring.

We then asked if this defective scar development affects surrounding neurons. Loss of NeuN indicates degenerating neurons[18], and its translocation from the nucleus to the cytosol identifies neurons exhibiting an initial stress response to pathologies[19–22]. Following stab injury, WT brains consistently maintained NeuN in the neuronal nuclei irrespective of their position relative to the injury site. In contrast, in $Dbn^{-/-}$ brains, NeuN translocation from the nucleus to the cytosol was present in 42% of neurons (Fig. 2C). As our disease model is considered as mild injury, we conclude that $Dbn^{-/-}$ brains exhibit signs of increased brain damage 7 days post injury.

DBN provides long-term tissue protection after traumatic brain injury. To study the long-term outcome of DBN deficiency, we extended the stab injury analyses to a later time point. At 30 days post injury, WT mice maintained well-defined GFAP+ scars exhibiting typical signs of long-term thinning (Fig. 2D)[15], whilst we no longer detected GFAP+ astrocytes in lesion sites of $Dbn^{-/-}$ brains (Fig. 2D, Figure S2A). To verify these findings, we also used vimentin as additional marker for astrocyte reactivity. Analogous to GFAP, WT astrocytes showed prominent vimentin levels in scars 30 days post injury, while $Dbn^{-/-}$ astrocytes were negative for this marker protein (Figure S2B). To analyze the fate of astrocytes in lesions without GFAP and vimentin immunoreactivity, we stained for SOX9, a transcription factor and nuclear marker for mature astrocytes[23]. In WT brains, we consistently detected Sox9-positive nuclei in astrocytes within scars. In contrast, in core lesions of $Dbn^{-/-}$ brains, SOX9 exhibited a strictly cytoplasmic localization (Fig. 2D), as reported for undifferentiated stem cells and precursor cells[24]. This cytoplasmic localization was scar-specific, as in the uninjured tissue adjacent to stab wounds in $Dbn^{-/-}$ brains, SOX9 showed its typical nuclear localization (Figure S3A). Cytoplasmic SOX9 in the scar tissue correlated with the absence of GFAP in all injured $Dbn^{-/-}$ brains, which led us to hypothesize that $Dbn^{-/-}$ astrocytes at the lesion sites are present, but do not maintain their typical reactivity.
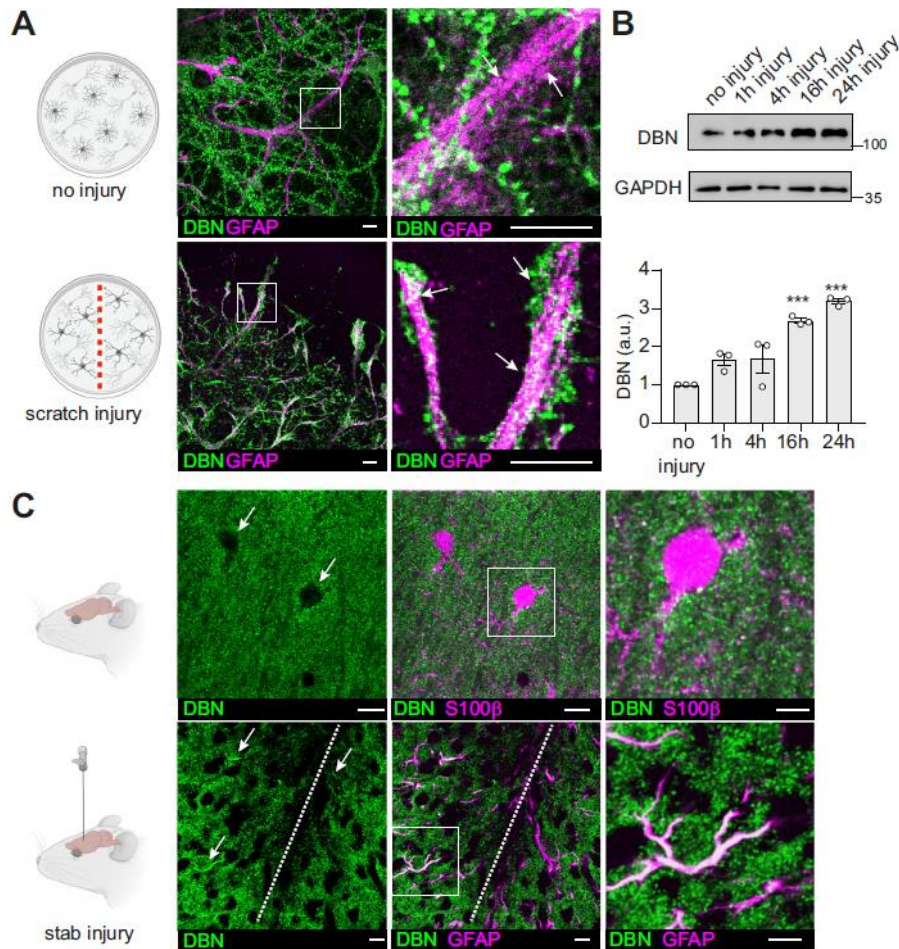
Fig. 1 DBN protein levels are increased in response to injury. A DBN labeling (green) in mixed 21 DIV cortical cultures without (upper panels) or with mechanical scratch injury (lower panels). Square in the left image is magnified on the right. Arrows show GFAP+ astrocyte processes, devoid of DBN (upper panel) and with strong DBN signals following scratch injury (lower panel). Representative image of three independent experiments. Scale bars: 10 μm. **B** DBN expression analyses by western blotting in enriched astrocyte cultures without, or 1, 4, 16, and 24 h after scratch injury. Quantification of protein levels showing mean, individual data points and SEM; $n = 3$ independent experiments, (one-way ANOVA $F = 23.39$; $DFn = 4$, $DFd = 10$, Dunnett's multiple comparisons test ***$P < 0.001$; multiplicity adjusted p values: no injury vs 16 h: $P = 0.0003$; no injury vs 24 h: $P = 0.0001$. **C** Sections of P30 mouse brains without (upper panels) or with stab injury (lower panels) were labeled with anti-DBN (green) and anti-S100β (upper panel, magenta) or anti-GFAP (bottom panel, magenta). Arrows show astrocytes devoid of DBN (upper panel) and with DBN protein following stab injury (lower panel). Scale bars: 10 μm. Magnifications on the right show no or high expression of DBN in S100ß+ or GFAP+ astrocytes in brains with or without stab injury, respectively. Representative image of two animals, three brain slices/animal. Scale bars: 20 μm. All confocal images in this figure are single optical sections. Source data are provided as a Source Data file.

Cresyl violet stainings supported this idea: multiple non-neuronal (Nissl body-) cells were present in proximity to the injury sites in $Dbn^{-/-}$ brains (Figure S4A). Labeling of stab-wounded brains with an antibody recognizing ALDH1L1, which is expressed in quiescent and reactive astrocytes[25], identified that GFAP-/cytoplasmic SOX9+ cells in $Dbn^{-/-}$ brains express this astrocyte marker protein (Figure S3B). Thus, 30 days after wounding, $Dbn^{-/-}$ astrocytes still occupied lesion sites, but were unable to uphold their reactive astrogliosis program.

Astrocyte scar formation and proliferation after injury are negatively regulated by invading monocytes[4]. We therefore studied the content of CD45+ monocytes in injured WT and $Dbn^{-/-}$ brains by immunohistochemistry (IHC). Comparable numbers of CD45+ monocytes were present inside lesion sites of

WT and $Dbn^{-/-}$ brains (30 DPI), but not in the surrounding tissue (Figure S4B).

At the same time, we identified a substantial loss of NeuN+ and Nissl+ cell bodies surrounding lesions in $Dbn^{-/-}$, but not in WT brains (Fig. 2E, Figure S4A). These findings show long-term neurodegeneration upon cortical stab-injuries in DBN-deficient mice.

Finally, to exclude the possibility that neurodegeneration in $Dbn^{-/-}$ brains following stab injury is owing to generally increased neuronal vulnerability rather than the observed defective astrocyte scarring, we analyzed the outcome of stab injury in the brain of $Dbn^{fl/fl}:CAMK\text{-}Cre^{+/cre}$ ($Dbn^{fl/fl}:CAMK\text{-}Cre$) mice. These mice lose DBN expression in neurons, but not in astrocytes. Following cortical stab injury, $Dbn^{fl/fl}:CAMK\text{-}Cre$
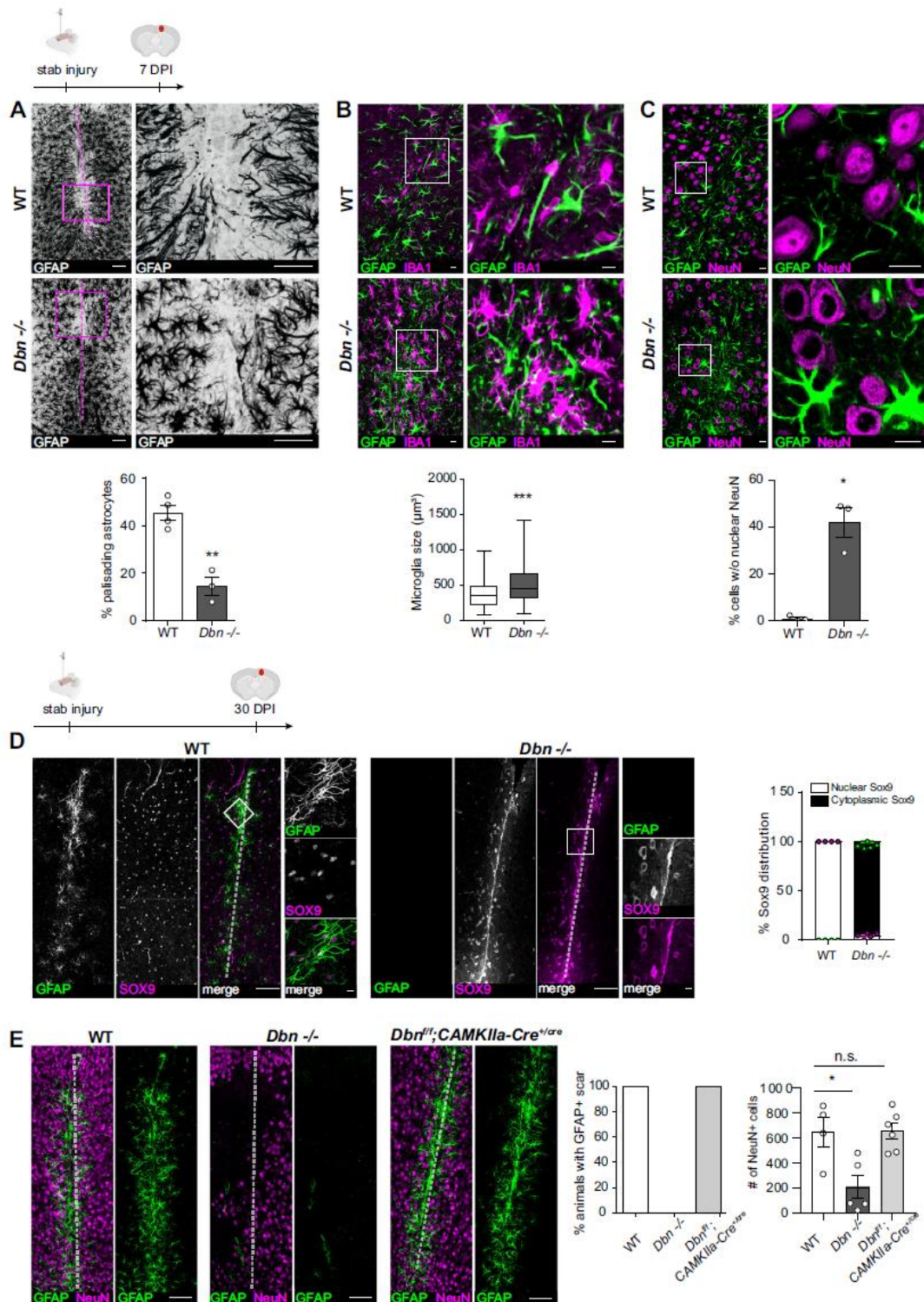
animals consistently show typical GFAP+ astrocytes with SOX9+ nuclei in lesions, with no signs of NeuN translocation after seven days of injury or NeuN loss 30 days after stab injury (Figure S3A, S4C, Fig. 2E). In summary, DBN is essential for astrocyte reactivity and damage containment during traumatic brain injury. DBN-loss perturbs injury-induced scar formation and suppresses maintenance of astrocyte reactivity, providing a

causal link of DBN function during injury-induced reactive astrogliosis.

DBN controls an injury-induced RAB8 membrane compartment. Towards identifying the DBN-dependent cellular mechanism in the injury setting, we employed the in vitro scratch injury of

Fig. 2 DBN controls astrocyte scar formation and astrocyte reactivity in vivo. A GFAP+ astrocytes at core lesion sites in WT (upper panels) and $Dbn^{-/-}$ (lower panels) brains, 7 days post stab injury (DPI). Magenta lines indicate the stab injury from needle insertion. Magnifications show stab lesions, with "palisading" astrocytes extending towards injury sites in WT mice. Scale bars: 100 μm. Quantification of palisading astrocytes in stab wounds 7 DPI, bar graph shows mean, individual data points and SEM. $n = 4$ WT and 3 $Dbn^{-/-}$ animals, Student's unpaired t test, two-sided, **$P = 0.0016$ $t = 6.205$ $df = 5$. **B** IBA1+ microglia (magenta) and GFAP+ reactive astrocytes (green) in the periphery of scars 7 DPI, in WT (upper panel) and $Dbn^{-/-}$ brains (lower panel). Scale bars: 10 μm. Quantification of soma sizes of IBA1+ microglia. $n = 145$ WT & 122 $Dbn^{-/-}$ cells from three mice per condition, graph shows box and whisker plots: box extends from 25th to 75th percentiles, central line = median, whiskers comprise all values from minimum to maximum, F test ***< 0.0001, Unpaired t test with Welch's correction, two-sided; ***$P = 0.000000205637371$, $t = 5.381$ $df = 201$. **C** NeuN+ neurons (magenta) and GFAP+ reactive astrocytes (green) in scars of WT (upper panel) and $Dbn^{-/-}$ brains (lower panel) 7 DPI. Scale bars: 10 μm. Quantification shows neurons without nuclear NeuN in scars. $n = 3$ WT and three $Dbn^{-/-}$ mice, bar graph shows mean, individual data points and SEM, Unpaired t test with Welch's correction, two-sided; *$P = 0.0231$, $t = 6291$ $df = 2044$. **D** IHC of WT and DBN$^{-/-}$ brains with 30-day post stab lesions. GFAP labeling (green) detects reactive astrocytes; SOX9 labeling (magenta) detects astrocytes. Scale bars in overview images: 200 μm. Scale bars in close up images: 10 μm. Quantification of cytoplasmic/nuclear SOX9 distribution in astrocytes in lesion sites. Single data points of nuclear SOX9 and corresponding error bars are displayed in magenta, cytoplasmic SOX9, and corresponding error bars in green. $n = 4$-5 animals per condition. **E** NeuN+ neurons (magenta) and GFAP+ reactive astrocytes (green) in WT (left), $Dbn^{-/-}$ (center) and $Dbn^{fl/fl}$:CAMK-Cre$^{+/cre}$ brains (right), 30 DPI. Quantifications show the percentage of animals with GFAP+ astrocytes (left graph) and NeuN+ cells (right graph) at lesion sites 30 days post stab wounding. Bar graph shows mean, individual data points and SEM $n = 4$ WT, five $Dbn^{-/-}$ animals, six $Dbn^{fl/fl}$:CAMK-Cre animals, (one-way ANOVA D$Fn = 2$, $DFd = 12$, $F = 8.397$; Dunnett's multiple comparisons test Multiplicity adjusted p value: *$P = 0.0112$). All images in this figure are confocal stacks. Scale bars: 200 μm. Source data are provided as a Source Data file.

---

cultured astrocytes. Following injury, WT astrocytes polarized, and extended long processes into the injury site (Figure S5A). In contrast, the majority of $Dbn^{-/-}$ astrocytes extended over smaller distances and frequently changed their orientation (Figure S5A; Movie 2), resulting in a significant decrease in wound closure (Figure S5B). During the wounding response, DBN, as well as overexpressed DBN-YFP only partially localized to prominent actin fibers and also decorated internal compartments consisting of vesicular and tubular structures (Figures S5C, D).

Given this subcellular distribution in astrocytes, together with a previous observation that identified DBN in association with internal membrane structures[26], we asked if DBN mediates injury responses by regulating membrane trafficking. Analyses of several trafficking compartments, including RAB5+, RAB7+, or RAB11 + endosomes showed no major differences in $Dbn^{-/-}$ astrocytes when compared with WT cells (Figure S6A). However, DBN-loss severely disturbed the distribution of RAB8 in astrocytes during mechanical injury. In WT astrocytes, using either GFP-RAB8A or an antibody that detects both RAB8A and RAB8B, we obtained signals of prominent RAB8+ tubular compartments adjacent to injury sites (Fig. 3A, Figure S6A). No signals were detected in cells depleted for both RAB8A and RAB8B demonstrating specificity to the antibody (Figures S46B, C). In $Dbn^{-/-}$ astrocytes, instead of marking internal tubules, RAB8 was mostly dispersed throughout the cytosol (Fig. 3A).

Western blotting (WB) confirmed that RAB8 protein levels and GTPase activity in $Dbn^{-/-}$ astrocytes were not altered when compared with WT, irrespective of injury (Fig. 3B, C), indicating that DBN is required during the generation of the tubule compartment rather than influencing the activity of the GTPase. Analogous to endogenous RAB8, GFP-RAB8A highlighted prominent membrane tubules in WT astrocytes, whereas GFP-RAB8A tubules in $Dbn^{-/-}$ were fragmented (Fig. 3D, Movie 3). Quantification of tubules in uninjured astrocyte cultures revealed very few RAB8A-positive tubules in both WT and $Dbn^{-/-}$ astrocytes. However, mechanical scratch injury increased the tubule number by 2.5-fold in WT astrocytes but not in $Dbn^{-/-}$ astrocytes (Fig. 3E), which indicates that tubular RAB8A endosomes form in response to injury and depend on the presence of DBN. We also detected Rab8+ tubules in polarizing WT astrocytes after injury in 21 DIV mixed cortical cultures and 7 DPI in vivo (Fig. 3F, G). In contrast, in $Dbn^{-/-}$ astrocytes, RAB8 was dispersed in processes and largely accumulated in vesicular

structures in the cell bodies. Only occasionally, RAB8 associated with short tubular structures. These findings suggest that DBN-dependent RAB+ tubular structures are regulators of astrogliosis in the setting of brain injury and scarring responses in vivo.

DBN generates tubular endosomes by counteracting Arp2/3-dependent actin nucleation. Dynamic rearrangement of the actin cytoskeleton is a critical component in generating tubular membrane systems[27,28]. It relies on the capacity of actin filaments to polymerize and depolymerize, a characteristic that can be influenced by the ability of DBN to bind the lateral filament surface, to bundle actin filaments and to inhibit actin nucleation[6,29,30]. We analyzed whether defects of $Dbn^{-/-}$ astrocytes in RAB8 compartments are linked to DBN and its function as actin regulator. In the first set of experiments, we co-transfected astrocyte cultures isolated from $Dbn^{-/-}$ mice with DBN-YFP (or control YFP) and labeled RAB8A using red fluorescent mRuby-RAB8A. Following in vitro injury, DBN-YFP expression, but not YFP, rescued the ability of $Dbn^{-/-}$ astrocytes to form membrane tubules (Fig. 4A). Next, we employed pharmacological approaches to address whether defective actin dynamics disrupts Rab8a tubules in $Dbn^{-/-}$ astrocytes. Low concentrations of Cytochalasin D (100 nM) interfere with the nucleation of new actin filaments whilst leaving existing filaments unaffected[31]. During scratch injury in $Dbn^{-/-}$ reactive astrocytes, this Cytochalasin D concentration re-established RAB8A-positive membrane tubules (Fig. 4B, Movie 4), suggesting that DBN induces tubule formation by antagonizing the cellular actin nucleation machinery. In this model, loss of DBN would increase actin nucleation. To test this idea, we applied the ARP2/3 inhibitor CK-666 or the formin-inhibiting molecule SMIFH2[32,33] to GFP-RAB8A expressing $Dbn^{-/-}$ astrocytes. Although inhibition of the ARP2/3 nucleation machinery by CK-666 reinstalled the ability of $Dbn^{-/-}$ astrocytes to form RAB8A tubules, the formin inhibitor did not (Fig. 4B Movie 4). Thus, DBN stabilizes actin filaments by mechanisms involving suppression of ARP2/3-dependent actin nucleation, a process essential for the injury-induced formation of the tubular RAB8 compartment.

DBN loss affects uptake and intracellular distribution of plasma membranes. RAB8 compartments have previously been reported to engage in plasma membrane recycling as well as in Golgi-derived delivery of cargo to the plasma membrane[34].
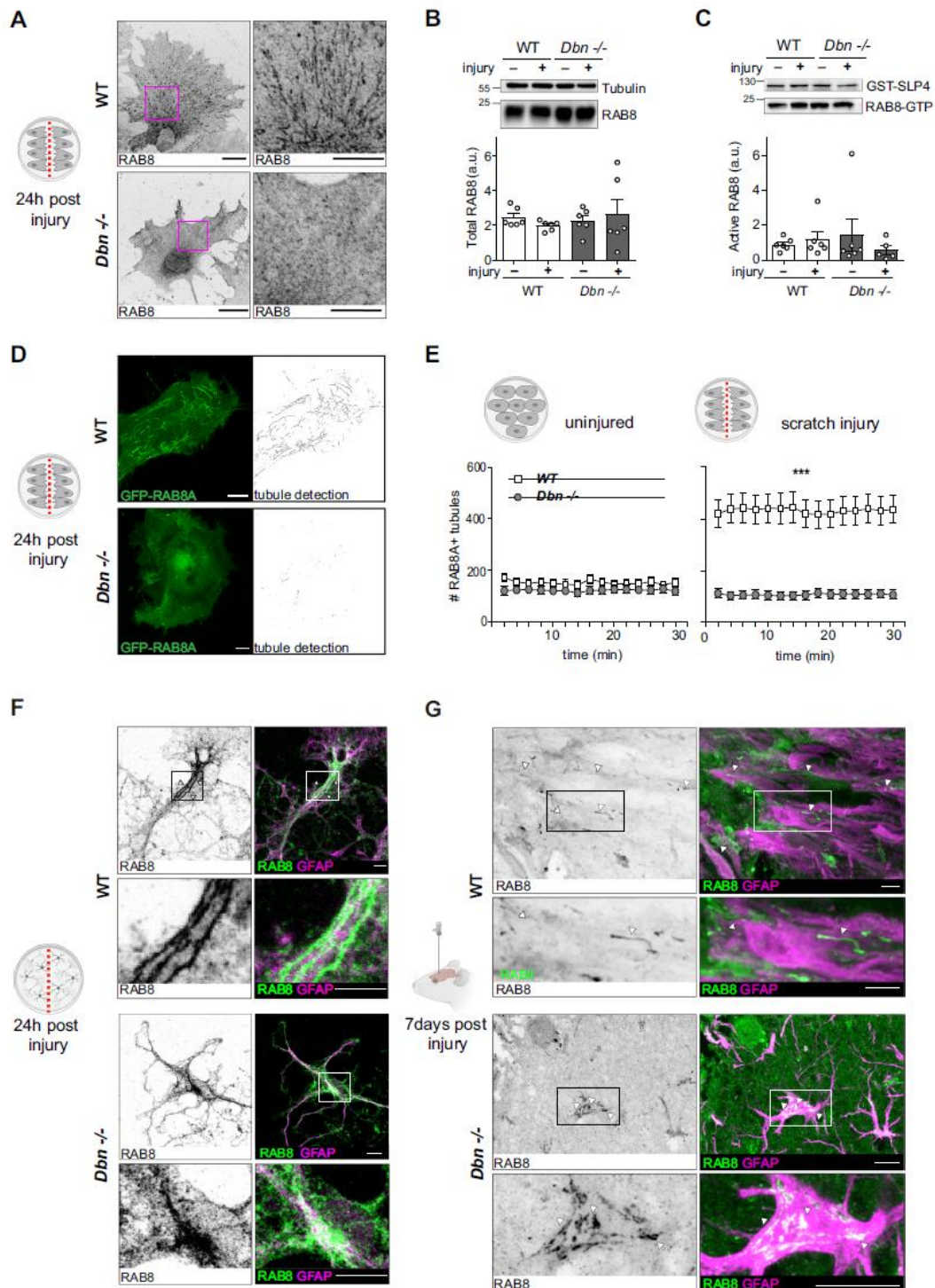
To characterize the specificity of endosomal trafficking of the DBN-dependent RAB8 compartment, we analyzed endogenous RAB8 tubules in WT and $Dbn^{-/-}$ astrocytes after injury using immunocytochemistry. RAB8-positive tubular structures were clearly orientated and extended through the cytosol of WT astrocytes, aligning closely with prominent actin filaments (Fig. 4C). In contrast, anti-RAB8 labeling in $Dbn^{-/-}$ astrocytes produced a diffuse cytosolic signal, with the appearance of cistern-like structures in the cellular periphery. These structures possessed a prominent ring of filamentous actin adjacent to the RAB8 signal, from where stub-like tubules originated (Fig. 4C). The presence of peripheral membrane cisterns suggested a general ability of $Dbn^{-/-}$ astrocytes to endocytose. We provoked increased membrane uptake in GFP-RAB8A-expressing astrocytes via EGF-induced macropinocytosis[35].

Fig. 3 DBN controls the formation RAB8 tubular endosomes during injury in cultured astrocytes. A RAB8 labeling in WT (upper panels) and $Dbn^{-/-}$ astrocytes (lower panels) 24 h after scratch injury in vitro. Scale bar: 10 µm. Representative images of four independent experiments. Images are confocal stacks. **B** Western blot analysis of RAB8 protein in WT and $Dbn^{-/-}$ astrocytes without or 24 h after injury. Tubulin serves as loading control. Rab8 and Tubulin antibody incubations were performed on the same membrane on consecutive days without stripping. Graph shows quantification of RAB8 protein levels in WT and $Dbn^{-/-}$ astrocytes, displaying mean, individual data points, and SEM ($n=6$ independent experiments, Bartlett's test for equal variances *** $P=0.0004$, one-sided Kruskal–Wallis test with Dunn's multiple comparisons test $P=0.6048$. **C** Western blot analysis of active RAB8-GTP isolated by GST-SLP4 pulldown from lysates obtained from WT and $Dbn^{-/-}$ astrocytes without or 24 h after scratch injury. GST levels confirm equal amounts of SLP4 in pulldowns. Rab8 and GST antibody incubations were performed on the same membrane on consecutive days without stripping. Quantification shows GTP-bound RAB8 levels in WT and $Dbn^{-/-}$ astrocytes, displaying mean, individual data points and SEM ($n=6$ independent experiments, Bartlett's test for equal variances ** $P=0.0014$; one-sided Kruskal–Wallis test with Dunn's multiple comparisons test $P=0.3589$). **D** GFP-RAB8A distribution in transfected WT (upper panels) and $Dbn^{-/-}$ astrocytes (lower panels). GFP-RAB8A-labeled compartments were detected automatically and are shown as skeletonized structures (black). Representative images of three independent experiments. Scale bars: 10 µm. Images are confocal stacks. **E** Quantification of GFP-RAB8A+ tubules in WT and $Dbn^{-/-}$ astrocytes, uninjured ($n=9$-10) and 24 h after scratch injury, displaying mean and SEM ($n=28$-32, two-way ANOVA (repeated measurements), F$=35.7$, $DFn=1$, $DFd=58$, Bonferroni's multiple comparisons test ***$P<0.001$ for all timepoints; multiplicity adjusted p values for timepoints in consecutive order: 0.000000341871; 0.000000021531; 0.000000016513; 0.000000039208; 0.000000017378; 0.000000014879; 0.000000189338; 0.000000625271; 0.000000265748; 0.000000100183; 0.000000085847; 0.000000034144; 0.000000095626; 0.000000034095). Cells were imaged for 30 min. **f** Presence of Rab8+ tubules (green) in GFAP+ astrocyte (magenta) at the wound edge of injured 21 DIV cortical cultures (upper panel). RAB8 in corresponding $Dbn^{-/-}$ astrocytes was dispersed in processes but accumulated in cell bodies (bottom panel). Representative images of three independent experiments. Scale bars: 10 µm. Confocal images are single optical sections. **G** Presence of Rab8+ tubules (green) in palisading processes of GFAP+ WT astrocytes (magenta) at lesion core following stab injury in the brain (upper panel). Arrowheads show Rab8+ tubules. RAB8 accumulated in distinct structures in soma of $Dbn^{-/-}$ astrocytes (arrows), whereas their processes showed no tubules (bottom panel). The tissue was labeled at 7 DPI. Representative images of two animals per condition. Scale bars: 10 µM. Images are confocal stacks. Source data are provided as a Source Data file.

EGF-treated WT astrocytes presented throughout the cytosol prominent GFP-RAB8A+ tubules, which locally assembled via the gathering of small Rab8A-positive particles (Movies 5 and 6). In $Dbn^{-/-}$ astrocytes, RAB8A+ membranes accumulated beneath the plasma membrane, where membrane cisterns frequently emerged but also rapidly disappeared (Figures S7A, Movies 5 and 6). These results establish the function of DBN during the generation and distribution of RAB8 associated membrane tubules.

Given that stabilization of membrane tubules requires the microtubule cytoskeleton in other cell types[36–38], we considered whether excessive ARP2/3-dependent actin dynamics in $Dbn^{-/-}$ astrocytes (Fig. 4B) antagonize the association of microtubules with the RAB8 compartment. Here, we visualized microtubules using SiR-tubulin in GFP-RAB8A expressing $Dbn^{-/-}$ astrocytes (Fig. 4D, Movie 7). GFP-RAB8A vesicles were visible in the cell's periphery in proximity to microtubules, but they did not form tubules. However, during the administration of CK-666, RAB8A-positive vesicles turned immediately into tubules, which then extended along the microtubules towards the cell body (Fig. 4D). Thus, DBN controls RAB8 membrane trafficking by antagonizing ARP2/3-dependent actin networks to enable the transport of tubular membranes along microtubules. In turn, DBN-loss disturbs the normal actin equilibrium and creates excessive ARP2/3 activity, which prevents the microtubule-assisted formation of tubular endosomes from RAB8+ vesicles (Fig. 4E).

DBN-dependent RAB8A tubules are required for β1-integrin trafficking. A known RAB8 target in cell lines is β1-integrin, a key molecule in cell polarization and migration[39,40], which also controls astrocyte differentiation and reactivity[41–43]. We used a C-terminus-specific β1-integrin antiserum to detect the spatiotemporal distribution of β1-integrin in astrocytes during injury, and identified prominent β1-integrin foci in RAB8 membrane tubules (Fig. 5A). To examine if DBN regulates β1-integrin, as a first read-out, we exploited the composition and assembly of focal adhesions, which are hot spots of β1-integrin activity. Antibody labeling in WT astrocytes during scratch injury showed the concentration of active β1-integrin, as well as the intracellular adapter paxillin in mature focal adhesions[40]. $Dbn^{-/-}$ astrocytes, in contrast, exhibited scattered membrane distribution of active β1-integrin with smaller paxillin+ focal adhesions (Fig. 5B). By

tracking GFP-tagged paxillin, we identified a persisting reduction in focal adhesion sizes during the injury-induced polarization of $Dbn^{-/-}$ astrocytes, when compared to WT cells (Fig. 5C). Thus, DBN controls the presentation of β1-integrin to focal adhesions in astrocytes during their responses to injury.

We then investigated if the DBN-dependent, injury-induced RAB8 membrane tubules are required for β1-integrin trafficking. To study the distribution and trafficking of β1-integrin independent of conformational states and antibody epitopes, we performed surface biotinylation experiments in injured WT and $Dbn^{-/-}$ astrocyte cultures. Although signals of intracellular biotinylated β1-integrin were at the detection limit after internalization, we found a substantial reduction of surface β1-integrin in $Dbn^{-/-}$ astrocytes when compared with WT astrocytes (Fig. 5D). Finally, we followed the internalization of active integrin in situ with an antibody-feeding assay. Thirty minutes after antibody labeling with anti-β1-integrin, the receptor was widely distributed throughout WT astrocytes (Fig. 5E). In contrast, in $Dbn^{-/-}$ astrocytes, β1-integrin accumulated beneath the plasma membrane of polarizing cells. We obtained a comparable β1-integrin distribution in WT astrocytes after depleting both RAB8 isoforms with RNAi (Fig. 5E), suggesting that DBN-dependent RAB8 compartments are major routes for β1-integrin trafficking. We conclude that the DBN-dependent, injury-induced RAB8 tubule compartment functions as an important hub to distribute internalized β1-integrin in astrocytes during injury.

DBN loss induces intracellular membrane accumulation in reactive astrocytes in vivo. The extensive accumulation of RAB8+ membranes beneath the leading edge of cultured $Dbn^{-/-}$ astrocytes prompted us to analyze internal membranes in vivo at the ultrastructural level using high-resolution transmission electron microscopy (TEM). We compared WT and $Dbn^{-/-}$ brains from 7 days post stab injury, using GFAP+ to locate reactive astrocytes in lesions. Processes of reactive astrocytes in WT brains in proximity to the stab lesion contained several endosome-like organelles, which frequently connected to thin membrane tubules. In contrast, processes of $Dbn^{-/-}$ reactive astrocytes in proximity to the stab injury displayed massive cytoplasmic vacuolization. The vacuoles resembled multilamellar bodies, as
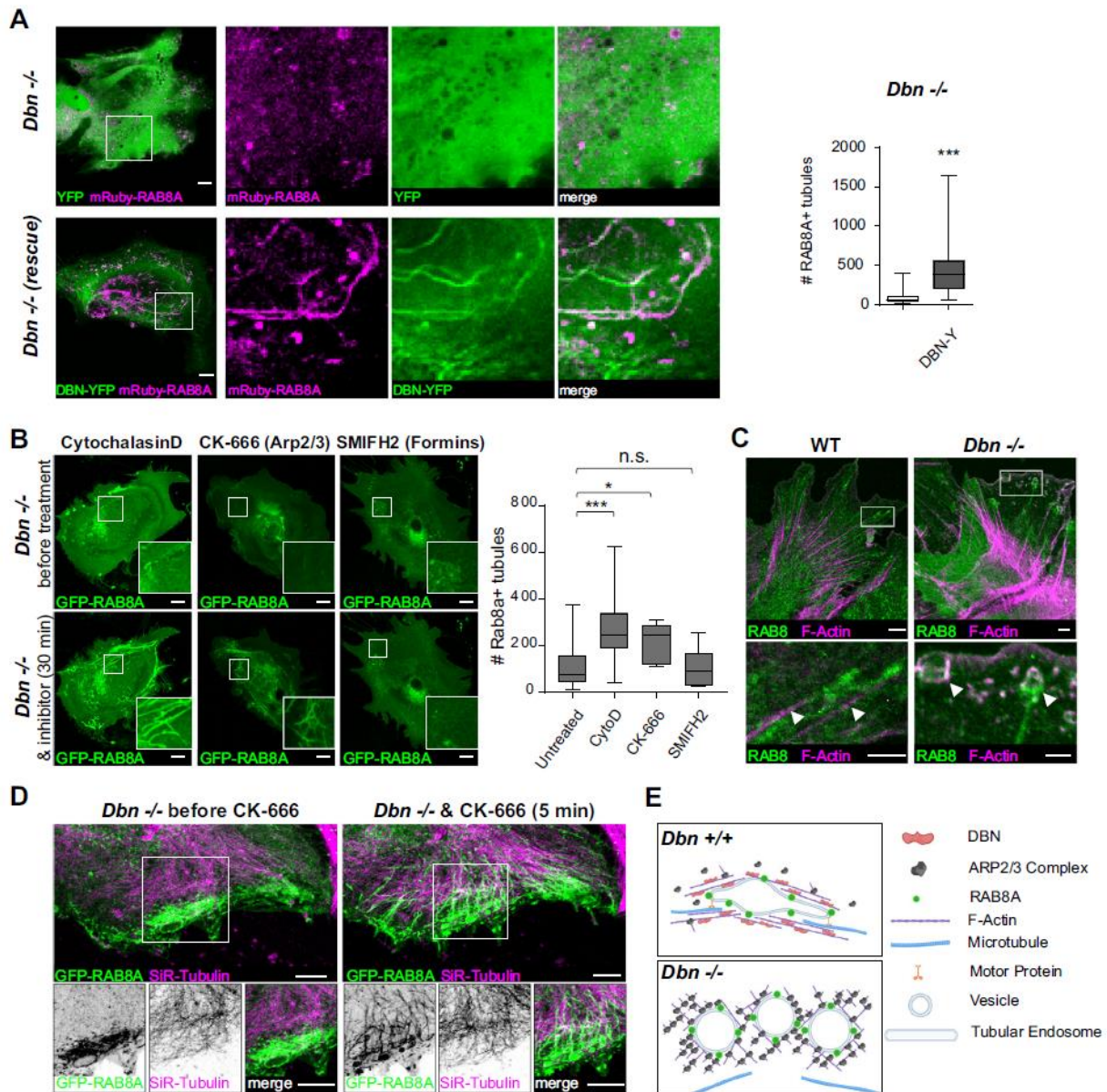
Fig. 4 DBN balances the actin nucleation machinery during RAB8A tubule formation. A DBN rescues RAB8A membrane tubules in $Dbn^{-/-}$ astrocytes. $Dbn^{-/-}$ astrocytes co-transfected with mRuby-RAB8A and YFP-control (upper panels), or with mRuby-RAB8A and DBN-YFP (bottom panels). Scale bars: 10 μm. Images are confocal stacks. Quantification of mRuby-RAB8A tubules displayed as box and whisker plots: box extends from 25th to 75th percentiles, central line=median, whiskers comprise all values from minimum to maximum; $n = 63$–65 cells from three independent experiments (F test for equal variances ***$P < 0.0001$, Unpaired t test with Welch's correction, two-sided, ***$P = 0.000000000025$, $t = 7.965$ $df = 68.19$). **B** Live imaging of $Dbn^{-/-}$ astrocytes expressing GFP-RAB8A before (upper panels) and 30 min after treatment with different inhibitors (lower panel); 100 nm Cytochalasin D (left), 100 μm CK-666 (center), or 25 μm SMIFH2 (right). Scale bars: 10 μm. Images are confocal stacks. Graph shows the quantification of GFP-RAB8A tubules 30 min after inhibitor treatment, Cytochalasin D, $n = 16$; SMIFH2, $n = 8$; CK-666, $n = 9$ cells; all from three experiments. Box and whisker plots: box extends from 25th to 75th percentiles, central line=median, whiskers comprise all values from minimum to maximum (one-way ANOVA $F = 11.47$, $DFn = 3$, $DFd = 63$, Dunnett's multiple comparisons test, multiplicity adjusted p values: * $P = 0.01534048$, ***$P = 0.0001$, ns $P = 0.9999$). **C** Distribution of endogenous RAB8A (green) and F-Actin (magenta) in WT (left panel) and $Dbn^{-/-}$ (right panel) astrocytes. Arrowheads in WT panel indicate RAB8+ tubules aligned with actin fibers. In the $Dbn^{-/-}$ panel, arrowheads highlight RAB8+ membrane cisterns. Representative images from three different experiments. Scale bars: 10 μm. Images are single confocal sections. **D** $Dbn^{-/-}$ astrocytes expressing GFP-RAB8A and labeled with SiR-tubulin before (left panel) and 5 min after adding 100 μM CK-666 (right panel); see Movie 7. Scale bars: 10 μm. RAB8+ tubules formed immediately after adding CK-666 and aligned with adjacent microtubules, while extending into the cytosol. Representative images showing the effect observed by CK-666 treatment in three independent experiments. Images are single confocal sections. **E** Proposed mechanism.: DBN functions as an essential switch in the actin network homeostasis, which supports the formation of RAB8A + tubular endosome along microtubules. Source data are provided as a Source Data file.

45
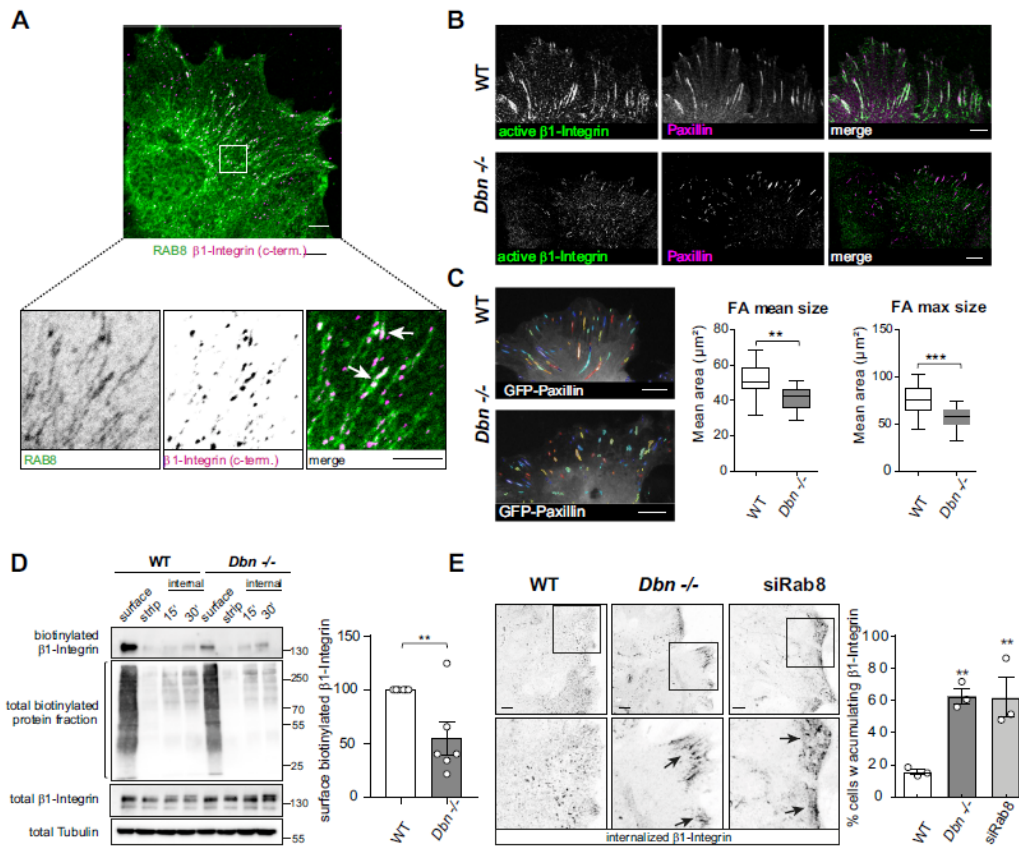
Fig. 5 DBN regulates RAB8 membrane trafficking of β1-integrin during injury. A Detection of β1-integrin (magenta in merged images) in RAB8+ tubules (green in merged images) in astrocytes. Arrows indicate RAB8+ tubules enriched with β1-integrin. Representative image of three independent experiments. Scale bar: 10 μm. Confocal images are single optical sections. **B** Confocal images of WT (upper panel) and $Dbn^{-/-}$ astrocytes (bottom panel) after mechanical injury, labeled for active β1-integrin (green) and paxillin (magenta). Representative images of three different experiments. Scale bars: 10 μm. Images are single optical sections. **C** Focal adhesions (FA) in WT (upper panel) and $Dbn^{-/-}$ astrocytes (lower panel) expressing GFP-paxillin analyzed by the Focal Adhesion Analysis Server. Graph shows box and whisker plots (box extends from 25th to 75th percentiles, central line=median, whiskers comprise all values from minimum to maximum) of focal adhesion (FA) mean sizes and FA maximum sizes over 22 h during live imaging experiments ($n = 17$ cells from three independent experiments, Student's unpaired t test (two-sided): FA mean size **$P = 0.0013$, $t = 3.515$ $df = 32$; FA max size ***$P = 0.0004$, $t = 3.995$ $df = 32$). Scale bars:10 μm. **D** Streptavidin-pulldown of proteins after surface biotinlyation of injured WT and $Dbn^{-/-}$ astrocytes. Western blot shows biotinylated β1-integrin in different conditions: immediately after surface biotinylation (surface), after removal of the surface-biotin label with MESNA (strip), 15 min and 30 min after incubating labeled astrocytes at 37 °C followed by MESNA treatment to remove the fraction of surface-exposed labeled proteins. Bar diagram shows quantification of surface β1-integrin after normalization to total integrin levels displaying mean, individual points and SEM; $n = 6$ experiments, Student's unpaired t test (two-sided) **$P = 0.0054$, $t = 3.541$, $df = 10$. **E** Labeling of internalized ligand-bound β1-integrin following antibody feeding in WT astrocytes (left image), $Dbn^{-/-}$ astrocytes (center image), and WT astrocytes after siRNA depletion of RAB8A and RAB8b (right image). Arrows indicate accumulations of β1-integrin directly beneath the leading edge of $Dbn^{-/-}$ or RAB8-depleted astrocytes. Boxes in upper panels are magnified in lower panels. Images are confocal stacks. Bar diagram shows quantification of astrocytes with antibody-labeled β1-integrin at leading edges displaying mean, individual points and SEM;. $n = 20$–37 cells from three experiments; one-way ANOVA $F = 12.57$, $DFn = 2$, $DFd = 6$ with Dunnett's multiple comparisons test WT vs $Dbn^{-/-}$: **$P = 0.0083$, WT vs siRab8: **$P = 0.0091$. Source data are provided as a Source Data file.

they were filled with amorphous, electron-dense material that was surrounded by double or multiple concentric membrane layers (Fig. 6A)[44]. Quantification of multilamellar bodies at injury and contralateral sites of WT and $Dbn^{-/-}$ brains showed that this compartment was induced upon injury only in the absence of DBN (Fig. 6A, B). In addition, we investigated the ultrastructure of astrocytic endfeet, which sustain high levels of membrane trafficking during nutrient and metabolite uptake, and efflux of waste products[2]. Analogous to astrocyte processes, astrocyte endfeet at the injury site in WT brains contained several endosomal structures. In contrast, excessive amounts of multilamellar bodies filled the endfeet at injury sites in $Dbn^{-/-}$ mice

(Figure S7B). In summary, astrocytes from $Dbn^{-/-}$ mice show excessive, injury-specific accumulation of membrane-derived material in both astrocytic processes and endfeet.

Discussion

We have identified the function of DBN in protecting the brain from tissue damage following injury. We show that (1) under physiological conditions, DBN protein is not expressed in astrocytes; however, its injury-induced upregulation in reactive astrocytes is required for the coordinated formation and maintenance of astrocyte scars, demonstrating its essential role in effective tissue protection in the brain. (2) At the cellular level, DBN shifts the
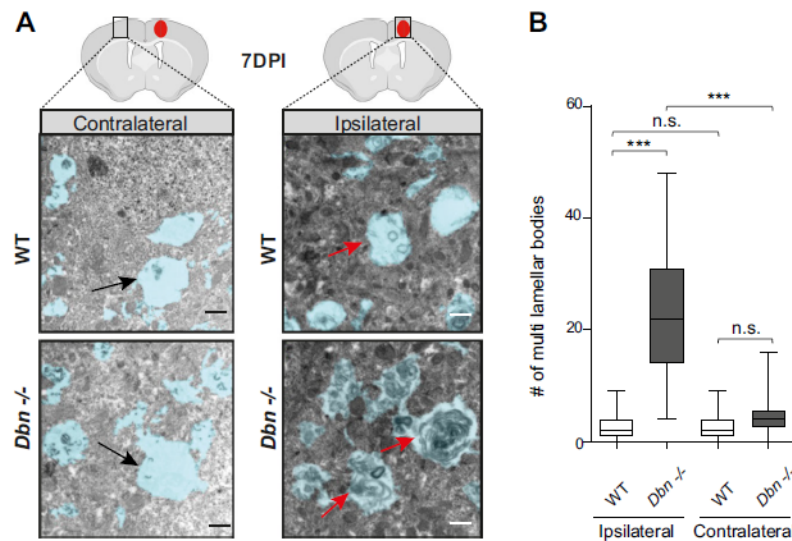
Fig. 6 DBN loss induced membrane accumulations in polarizing astrocytes during injury. A TEM ultrastructural architecture of astrocytes in brains of WT and $Dbn^{-/-}$ mice. Images were acquired on the contralateral side of injury (left panels) or inside the lesion core (right panels); 7 days post stab injury (7 DPI). Astrocyte processes are shaded in blue. Black arrows show astrocyte processes largely devoid of membranous compartments, on the site contralateral to the stab injury. Red arrows show astrocyte processes at the injury site with endosome-like organelles (WT, upper image) or with multilamellar bodies ($Dbn^{-/-}$, bottom image). Scale bars: 500 nm. **B** Quantification of multilamellar bodies displayed as box and whisker plots: box extends from 25th to 75th percentiles, central line=median, whiskers comprise all values from minimum to maximum. Field of view size: 1170 μm². Number of fields/view: 92 WT and 77 $Dbn^{-/-}$ ipsilateral, 85 WT and 77 $Dbn^{-/-}$ contralateral from three WT and three $Dbn^{-/-}$ animals (Bartlett's test for equal variances ***$P < 0.001$; one-sided Kruskal–Wallis test with Dunn's multiple comparisons test ***$P < 0.001$; multiplicity adjusted p values: Ipsilateral WT vs Ipsilateral $Dbn^{-/-}$: $P = 0.000000000000047$; ipsilateral WT vs contralateral WT: $P = 0.999999999999999$; contralateral WT vs contralateral $Dbn^{-/-}$: $P = 0.190172692939112$; Ipsilateral $Dbn^{-/-}$ vs contralateral $Dbn^{-/-}$: $P = 0.000000755492543$). Source data are provided as a Source Data file.

actin network organization from ARP2/3-dependent arrays to microtubule-compatible scaffolds, which facilitate the formation of injury-induced RAB8A-positive membrane tubules. (3) These tubules serve as a hub for the membrane trafficking of surface proteins involved in coordinating adhesive responses, such as β1-integrin. (4) The actin-dependent facilitation of RAB8 membrane tubules by DBN is essential to maintain astrocyte reactivity, ensure the physical integrity of the scar and prevent neurodegeneration.

We, therefore, propose a conceptually new role for DBN as an injury-induced actin regulator in reactive astrocytes.

DBN functions as an injury-induced actin regulator in membrane trafficking. DBN is highly abundant in dendritic spines and developing neurites, and confers resilience in dendritic spines during cellular stress responses[13,45,46]. Surprisingly, DBN protein is not detectable in astrocytes under healthy conditions but immediately upregulated after mechanical damage (Fig. 1, Figure S1). These findings are corroborated by previously published transcriptome data: focal penetrating injuries, like stab wounds and spinal cord injuries, cause significant upregulation in DBN transcripts in astrocytes. However, other disease models without direct mechanical damage, like "transient middle cerebral artery occlusion" -based stroke or lipopolysaccharide injections, show less pronounced increases in DBN mRNA[47–49]. Tissue damage in association with lesions is thus one major trigger for DBN upregulation in astrocytes. Currently, neither the molecular signaling pathways nor the mechanisms controlling DBN protein upregulation, are known. However, it is conceivable that DBN protein abundance is, in addition to increased transcription, also modulated by post-translational modifications. Such mechanisms would, analogous to the ATM-dependent phosphorylation of DBN in neurons[13], extend DBN protein lifetime and abundance.

Unexpectedly, the cell biological mechanism underlying the role of DBN during astrocyte scar formation involves a directive function for its participation in membrane trafficking. Until now, few studies have linked DBN to membrane dynamics in cells, other than a demonstration that DBN principally binds to membranes[26], that it restricts the entry of rotavirus into cells by limiting endocytosis[50], and that it regulates antigen presentation of dendritic cells[51]. Our study identifies a further avenue in DBN-dependent membrane trafficking and protein sorting mechanism that functions by stabilizing RAB8-positive tubular endosomes upon injury.

In cell culture and in vivo, we discovered prominent RAB8-positive tubular endosomes specific to a post-injury setting in astrocytes, which extend long palisading-like processes into wound areas. The GTPases, RAB8A and RAB8B, facilitate distinct routes of polarized membrane transport. RAB8 is involved in endocytosis, membrane recycling, autophagy, and exocytosis by associating with vesicles, macropinosomes, and tubules[34,52,53]. Moreover, RAB8 has been implicated in various diseases ranging from microvillar inclusion disease and cancer to neurodegenerative diseases such as Alzheimer's and Parkinson's disease[34]. Tubular membrane compartments serve as logistical platforms to sort membrane-bound cargos[54]. Membrane tubulation occurs particularly on maturing early endosomes and macropinosomes to separate components from the quick "bulk flow" back to the plasma membrane and to direct them towards other compartments such as the Golgi network or recycling endosomes[55]. The actin cytoskeleton creates stable tubular subdomains, where membrane-bound cargos segregate and concentrate according to their designated destinations[28,56,57]. We propose a role for DBN in inward-directed RAB8-based membrane trafficking: upon wounding, DBN may contribute to the uptake of plasma membrane material by compiling
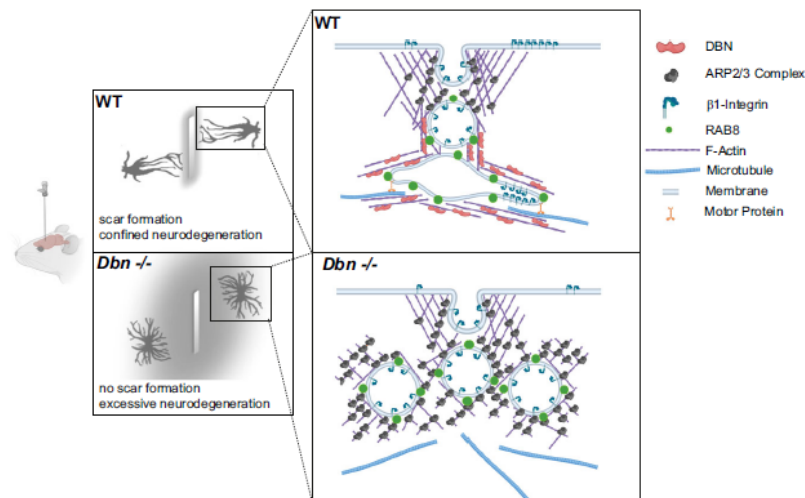
Fig. 7 Astrocytes require DBN to control damage during brain injury. Proposed model of how DBN/Rab8 functions during astrocyte polarization and scarring responses. In response to CNS injury, DBN generates actin scaffolds suitable for tubule-based membrane trafficking. DBN-loss results in the accumulation of endocytotic vesicles beneath the plasma membrane and affects the sorting of adhesion receptors essential for interaction with lesion core components. In this way, DBN/Rab8 membrane tubules are fundamental for the polarization and scarring responses of reactive astrocytes.

endocytosed receptors and material in the injury-induced RAB8 compartment that are essentially sorted by DBN-stabilized tubules (Fig. 7).

DBN antagonizes ARP2/3-dependent actin dynamics. ARP2/3-dependent actin nucleation has been shown to drive the fission of existing tubules into vesicular endosomes by the WASH complex[58]. DBN associates dynamically with scaffolds of forming tubular endosomes and counteracts their ARP2/3-dependent fission (Fig. 4b, d). DBN could thereby occlude ARP2/3-binding sites on the actin scaffold by its sidewise binding to actin filaments[6]. This model is consistent with DBN competition of ARP2/3 function, as identified in our pharmacological rescue experiments. The colocalization of DBN along RAB8+ tubules in our rescue experiments further supports a role of DBN as an integral scaffold component around tubular endosomes. Structural analyses showed that drebrin is able to form tetramers and thereby to bundle actin filaments[30]. An analogous organization of actin filaments by DBN at RAB8+ compartments could possibly promote membrane tubulation as well as counteract the ARP2/3 machinery. In addition, DBN could also facilitate the extension of RAB8 tubules from underneath the leading edge into the cell body by arranging the surrounding actin architecture. The observable actin filaments in WT astrocyte processes generally run parallel to RAB8 tubules. These linear actin filaments may serve as a permissive scaffold for RAB8 tubules, which then stabilize along intermingled microtubules analogous to membrane tubulation during sorting to recycling endosome transition in non-neuronal cells[36–38]. This mechanism would be susceptible to mislocalized ARP2/3-actin arrays upon DBN loss. Our live-imaging results also support this mechanism in view of $Dbn^{-/-}$ astrocytes, where, until their pharmacological disruption, ARP2/3-actin networks prevent the tubulation and transport of RAB8A-positive membrane along microtubules. We propose that DBN serves as a master switch to enable the assembly of microtubule-compatible actin networks for tubular membrane trafficking (Fig. 7).

Cellular trafficking by RAB8 tubular endosomes. Tubular endosomes and/or tubule-derived vesicles deliver their content to intracellular destinations, where it may be redistributed or degraded according to cellular requirements for efficient polarized astrocyte outgrowth. DBN deficiency disrupts the RAB8-dependent tubular protein sorting machinery. Consequently, membranes and associated proteins accumulate in intermediate endosomal compartments instead of being rerouted in a polarized manner in sufficient numbers. The resulting deficits and mislocalization of surface receptors first evoke the failed wounding response and polarization of astrocytes followed by their erratic behavior during scarring. The disarray within the scarring astrocytes could lead to the downregulation of their reactivity, as shown by the loss of GFAP and translocation of SOX9—either in a cell-autonomous manner and/or by an affected interplay with other cell types such as microglia.

Our protein traffic-based mechanism is supported by findings in DBN-depleted epithelial cells, which share some localization defects in apical markers with RAB8A-deficient intestinal cells during microvillar inclusion disease[59,60]. In addition, RAB8 was shown to organize cell adhesion in conjunction with RAB13 by transporting adhesion molecules, in cultured epithelial cells[61]. Moreover, the closely RAB8-related RAB13 organizes the collective cell migration of these non-neuronal cells in wounding assays in an ordered manner[62], analogous to our findings with erratic DBN-deficient astrocytes in scars in vivo and during live imaging experiments.

β1-integrin trafficking and astrocyte reactivity. The induction of tubular endosomes in response to injury suggests that they represent an efficient way of transporting and sorting cargo relevant for the injury response in astrocytes. We show the mislocalization of endogenous β1-integrin in DBN-deficient astrocytes in a Rab8-dependent manner. Cells require tight control of β1-integrin in terms of levels and distribution at the cell surface to migrate efficiently. The key mechanism for this is retrograde trafficking[63]. Inadequate β1-integrin subunits at the surface impair the assembly and turnover of focal adhesions, as seen with the outgrowth defects observed in DBN-deficient astrocytes. In particular, the vanishing astrocyte reactivity highlights comprehensive defects in signal reception and computation through the mis-sorting of membrane receptors. Astrocytic

β1-integrin has an important role as a co-receptor in signaling pathways, which control astrocyte reactivity[41–43]. However, other misregulated membrane receptors undoubtedly also contribute to the observed phenotype, and further research screening DBN-deficient astrocytes is required to identify them.

DBN function in brain astrocytes. A major finding of this study is the relevance of injury-induced DBN in forming functional astrocyte scars. We showed that DBN is crucial for the coordinated polarization and palisade-like outgrowth of astrocytes. These locally occurring morphological changes are of vital importance to restrict inflammation and fibrotic tissue[64], as astrocytes from adjoining regions do not migrate into lesion sites[15,65]. The DBN-dependent establishment of an astrocyte scar in turn, is essential for damage containment in the CNS, as highlighted by the high neurodegeneration observed in DBN-deficient mice without astrocyte scars. What is more, the severity of the DBN-dependent membrane-trafficking defects became apparent in our in vivo TEM studies. We showed the prominent enrichment of membranous material in multilamellar structures within processes and endfeet of DBN-negative astrocytes. The extent of these accumulating multilamellar structures in astrocytes is, to our knowledge, unique, occurs only upon injury and supports our results of trafficking defects in cell culture. Moreover, this phenomenon resembles membrane whorls, which are evocative for autophagy and which accumulate in smooth muscle cells during atherosclerosis[44,66]. Analogous structures have been reported from Alzheimer's disease and amyotrophic lateral sclerosis patients as well as neurons expressing mutated huntingtin[67–69]. Our findings indicate a putative role of the polarized DBN-Rab8-dependent membrane trafficking for disease-specific autophagy, which is well aligned with astrocytes becoming phagocytic under pathological conditions[70]. The aspects of DBN deficiency identified in astrocytes in our study, are likely to exacerbate a mild CNS insult into major trauma with progressing neurodegeneration. Further dissection of the underlying mechanism could open new therapeutic avenues to treat CNS trauma and, possibly, degenerative conditions, which to date have dismal outcomes.

In conclusion, this study identifies an important function of injury-induced DBN in controlling damage containment in the CNS via membrane trafficking. As DBN and its downstream targets RAB8 and β1-integrin are broadly expressed, it is conceivable that this mechanism may be pivotal in other pathologies in the CNS as well as in different organ systems.

Methods

Ethical approval. All animals were handled in accordance with the relevant national guidelines and regulations after ethical approval. Protocols were approved by the 'Landesamt für Gesundheit und Soziales' (LaGeSo; Regional Office for Health and Social Affairs) in Berlin, and animals are under the permit number G0189/14.

Mouse strains. $Dbn^{-/-}$ mice were described previously[12]. B6.CAMK:Cre/Dbn$^{fl/fl}$ mice were generated by crossing B6.Cg-Tg(Camk2a-cre)T29-1Stl/J (kindly provided by Dietmar Schmitz, Charité Berlin;[71] with B6. Dbn$^{fl/fl}$ mice. BAC Aldh1L1 eGFP mice, used for initial stab wound experiments, were described previously[14]. Mice were housed in individually ventilated cages (IVCs). The cages contained wooden bedding material (SafeR Select, Safe), nestlets (Ancare), and a red, triangular plastic house (length: 12,5 cm, width: 11 cm, height: 6 cm; Tecniplast) or a plastic tunnel (length: 10 cm, diameter: 4,5 cm, in-house fabrication). The animals were maintained under standard conditions (room temperature: 22 ± 2 °C; relative humidity: 55 ± 10%) on a light:dark cycle of 12:12 h of artificial light (lights on from 6:00 a.m. to 6:00 p.m.). The mice were fed pelleted mouse diet ad libitum (Ssniff, V1534-000) and had free access to tap water at all times.

Antibodies and reagents. Antibodies and their used concentrations in Western blotting (WB), immunofluorescence (IF), and immunohistochemistry (IHC): please note that several lots of each antibody were used over the years. Mouse anti-DBN M2F6 (Enzo Lifesciences, ADI-NBA-110-E, IF & IHC 1:100; WB 1:1000), rabbit anti-GFAP (Synaptic Systems, 173 002, IF & IHC 1:1000), guinea pig anti-GFAP (Synaptic Systems, 173 004, IHC 1:400), guinea pig anti-S100β (Synaptic Systems, 287 003, IHC 1:200); rabbit anti-S100β (Atlas Antibodies, HPA015768, IHC 1:1000), mouse anti-alpha tubulin DM1a (Sigma-Aldrich, T6199, WB 1:5000), mouse anti-NeuN A60 (Millipore, MAB377, IHC 1:1000), rabbit anti-IBA1 (Wako, 019-19741, IHC 1:500), anti-MAP2 (Synaptic systems, 188 004, IHC 1:500), mouse anti-GAPDH 6C5 (Abcam, ab8245, Wb 1:5000), mouse anti-RAB8 (BD Biosciences, 610844, WB 1:1000), goat anti-pan RAB8 (Sicgen, AB3176-200, IF & IHC 1:100), rabbit anti-integrin beta1 (Cell Signaling, #4706 S, WB 1:1000), mouse anti-CD29 18/CD29 (BD Biosciences, 61046, WB 1:1000), rat anti-active integrin beta1/CD29 9EG7 (BD Pharmingen, 553715, IF 1:100), rabbit anti-integrin beta1 c-term (LSBio, LS-C413122, IF 1:100), rabbit anti-paxillin (Genetex, GTX125891, IF (1:250), rabbit anti-GST (Abcam, #9085-200 µl, WB 1:500). Horseradish peroxidase (HRP)-conjugated secondary antibodies (WB 1:5000): Goat Anti-Rabbit IgG Antibody (H + L) (VectorLabs, PI-1000), Horse Anti-Mouse IgG Antibody (H + L) (Vectorlabs, PI-2000); cross-absorbed secondary antibodies conjugated to cyanine or Alexa dyes were purchased from Dianova (IF & IHC 1:250): Donkey IgG anti-Mouse IgG (H + L)-Alexa Fluor 488 (Dianova, 715-545-150), Donkey IgG anti-Mouse IgG (H + L)-Alexa Fluor 647 (Dianova, 715-605-150), Donkey IgG anti-Goat IgG (H + L)-Alexa Fluor 488 (Dianova, 705-545-147), Donkey IgG anti-Guinea Pig IgG (H + L)-Cy3 (Dianova,706-165-148), Donkey IgG anti-Rabbit IgG (H + L)-Alexa Fluor 647 (Dianova, 711-605-152), Donkey IgG anti-Rabbit IgG (H + L)-Alexa Fluor 488 (Dianova, 711-545-152), Donkey IgG anti-Rabbit IgG (H + L)-Cy3 (Dianova, 711-165-152). Filamentous actin was labeled with ActiStain488, 555, or 670 phalloidin (Tebu Bio, PHDG1-A, PHDH1-A, or PHDN1-A, 1:250). DNA staining was carried out using Hoechst 33258 (Thermo Scientific, H3569, 1:10,000).

Plasmids. Lifeact-GFP was cloned into the pCDF backbone (SBI), after replacing copGFP with a suitable multiple cloning site via XbaI/SalI digest (Sequence of MCS: TCTAGAGCTAGCGCTACCGGTCGCCACCATGGGATGTACAGCGGC CGCGTCGAC). Accordingly, the CMV promoter was substituted with the astrocyte-specific gfaABC1 promoter, kindly provided by Michael Brenner (University of Alabama, US), using PCR (pGFAP-5:ATAGATATCAACATATCCTGG TGTGGAGTAGGG, pGFAP-3:ATAGCTAGCGCGAGCAGCGGAGGTGATGC GTC).

pEGFP-RAB8A was a gift from Daniel Gerlich (Addgene plasmid # 31803[72]. EGFP-Rab8a was cloned via PCR into the pCDF backbone for viral expression (pCDF-GFP-5:GACCTCCATAGAAGATTCTAGAGCTAGCATGGTGAGC AAGGGCGAGGAGCTGTTC, pCDF-RAB8A-3: GTAATCCAGAGGTTGATT GTCGACTCACAGAAGACACATCGGAAAAAGCTGC).

mRuby- RAB8A was generated through replacement of EGFP in pCDF-eGFP-RAB8A with mRuby via NheI/BsrgI from pcDNA3-mRuby kindly provided by Nils Rademacher (Charité Universitätsmedizin Berlin, Germany). The lentiviral construct pCDF-paxillin-EGFP was subcloned from pEGFP-N3-paxillin (gift from Rick Horwitz,[73] Addgene plasmid #15233) into pCDF-GFAP:Lifeact-GFP via NheI/BsRGI after silent mutation of an internal BsRGI site (Paxillin-BsrGImut-s: GAGGAGGAACACGTGTATAGCTTCCCAAACAA GCAG; Paxillin-BsrGImut-as: CTGCTTGTTTGGGAAGCTATACACGTGT TCCTCCTC).

Previously published pEYFP-N1-DBN E was co-transfected in rescue experiments in $Dbn^{-/-}$ astrocytes in conjunction with pCDF-mRuby-RAB8A[74]. pEYFP-N1 (Takara Bio Inc) was used as a corresponding negative control. pDEST15-hSlp4-a was purchased from Addgene (Plasmid#40046). All used primers and oligonucleotides are listed in the Supplementary information (Tab. S8).

Cell culture and plasmid transfection. Cortical astrocytes were isolated from WT or $Dbn^{-/-}$ mouse brains according to procedures for rats[75]. Cerebral cortices from P2 mice were isolated, mechanically dissociated in Hanks' Balanced Salt Solution (HBSS) and trypsinized (Life Technologies) for 15 min at 37 °C. Afterwards, trypsin (Invitrogen) was inhibited by triturating cells in complete Dulbecco's modified Eagle's medium (DMEM, Lonza) with 10% FBS. Cell suspensions were subsequently plated into T75 flasks, coated with collagen-I (0.025%, BD Biosciences) and 100 µg/ml poly-ornithine (Sigma). Microglia were erased by treating astrocytes cultures at high density for 90 min with 60 mM L-leucine-methylester (LME, Sigma) in complete medium. Astrocytes were cultivated to 90% of confluency and, subsequently, plated for imaging or biochemical experiments. Enriched microglia cultures were acquired by shaking T75 cm flasks with polygonal astrocytes at 150 rpm at 37 °C for 2 h prior to treatment with LME. Supernatant with floating microglia was plated on poly-ornithine-coated glass coverslips. Microglia cultures contained <5% astrocytes. Primary mixed cortical cultures were dissected from male and female embryonic day 16.5 WT or $Dbn^{-/-}$ mice[76]. Cortices were isolated and digested for 15 min with 10% Trypsin in HBSS (Life Technologies), washed with HBSS and triturated to single cells with glass pipets. Cells were plated on poly-ornithine (15 µg/ml)-coated coverslips and cultured in Neurobasal A medium (Life Technologies) containing 2% B27 (Life Technologies), 1% penicillin/streptomycin (Life Technologies), 100 µM β-mercaptoethanol (Applichem), and 1% GlutaMAX (Life Technologies). HEK293TN were obtained from BioCAT (Cat. no. LV900A-1-GVO-SBI). All culturing materials were sterile and cell culture techniques were undertaken in Class II vertical laminar flow

49

cabinets (ThermoFisher Scientific). HEK293TN cells were not authenticated. Cultured HEK293TN cells were tested negative for mycoplasma. Astrocytes were transfected using TransIT LT1 (Mirus) according to the manufacturer's protocol.

Lentivirus production and astrocyte infection. Probes of fluorescent RAB8A and paxillin were expressed in astrocytes via lentiviral transduction. FIV particles were produced in the HEK293TN producer cell line (BioCat) and harvested analogously to HIV particles[77]. In all, 70% confluent astrocytes from WT and $Dbn^{-/-}$ mice on glass-bottom dishes were transduced 7 days before scratch wounding and live-cell imaging.

RNA interference. Astrocytes were transfected with siRNAs using Lipofectamine RNAiMax (Thermo Scientific) according to the manufacturer's instructions. The following published siRNA oligonucleotides were used (Sigma-Aldrich): siRab8a (GGAAUAAGUGUGAUGUGAA[78], siRab8b (GAAUGAUCCUGGGUAACAA[79], and control siRNA (AGGUAGUGUAAUCGCCUUGUU)[75], (Tab. S8).

Scratch wound in vitro and live-cell imaging. Confluent astrocytes were cultured in phenol red-free DMEM (Thermo Scientific) with 10% fetal bovine serum (FBS). Scratch wounds were performed by pulling a 200 µl-pipette tip through the confluent astrocyte layer as established previously:[80]. To subject the entire monolayer to the scratch injury, different scratch patterns were performed: for 18 mm coverslips, one scratch was performed vertically and one scratch was performed horizontally. For 4 well µ-slides dishes (IBIDI), one vertical scratch was performed. For 30 mm dishes, three horizontal and three vertical scratches were performed. Injured astrocytes were either biochemically analyzed via western blot or studied in live-cell imaging. Cell behavior was followed by live-cell imaging for 22 or 30 h using a Nikon Widefield with CCD camera, scanning stage, and environmental control chamber (OKO lab) and a ×40 objective (N.A. 0.7) with 1.5× intermediate magnification. Cells were imaged at 20-min intervals with composite large images (3 × 3 fields of view). Imaging start, unless specified otherwise, was 4 h after in vitro injury. Astrocytes in compiled movies were analyzed using kymographs in Fiji[81].

Quantitation of membrane tubules. Tubular membrane compartments were quantified based on a macro for Fiji, originally designed to analyze analogous structures in still images in heart muscle[82]. We extended the functionality of the original code by enabling analyses of z-stack image sequences acquired in live imaging experiments. The macro has been made available on github (see Code Availability).

Pharmacological treatments. In all, 100 nM Cytochalasin D (Merck Calbiochem, Cat. no. 250255), 100 µM CK-666 (Sigma-Aldrich, Cat. no: SML0006-5MG) or 25 µM SMIFH2 (Sigma-Aldrich, Cat. no. S4826-5MG) were pre-diluted in phenol red-free DMEM and added to GFP-RAB8A-expressing astrocytes after recording baseline for 30 min without treatment. Microtubule dynamics were imaged after incubating astrocytes for six hours in 1 µM SiR-tubulin (Spirochrome, cat#: SC002) in phenol red-free DMEM.

Immunocytochemistry. Cultured astrocytes were fixed using 3.7% formaldehyde in cytoskeleton-preservation buffer (25 mM HEPES, 60 mM PIPES, 10 mM EGTA, 2 mM MgCl$_2$, pH 7.4) for 20 min. After three washes with cytoskeleton-preservation buffer, cell permeabilization, while maintaining the utmost integrity of the cytoskeleton and endosomes, was achieved through 3 min incubation with 0.02% Triton X-100 in Phosphate-buffered saline (PBS). After three washes with PBS and brief incubation in 1% bovine serum albumin (BSA) in PBS, cells were incubated with primary antibodies diluted in PBS for 1 h at RT. After three washes with PBS and brief incubation in 1% BSA in PBS, cells were incubated in highly cross-absorbed secondary antibodies for another hour at RT. After three washes with PBS, cells were mounted in Mowiol. To visualize endogenous RAB8 tubules, PBS was generally replaced by the cytoskeleton-preservation buffer. Cells were permeabilized by incubation with 0.02% Triton X-100 in the cytoskeleton-preservation buffer for 30 min at RT. Wash steps were extended to 5 min each.

Confocal microscopy and imaging processing. Cells were imaged via multitrack mode on either Leica Sp8 (Leica) or Nikon A1Rsi+ (Nikon) confocal microscopes. Large image and multipoint scans were performed on Nikon A1 microscopes using an automated stage. Image processing were performed in FiJi and/or Imaris (Bitplane). To isolate and highlight DBN immunreactivity only in astrocytes, we merged GFP and GFAP in the CoLoc application of Imaris to create a mask. DBN signals within this mask resulted in "Astrocyte merge" by subtracting signals outside of astrocytes from the DBN channel. To categorize palisading astrocytes, we adapting protocols from previous publications[3,14]. We analyzed GFAP+ astrocytes in areas 300 µm around to the core lesion site. Polarized astrocytes with longer processes beyond the typical ~25 µm radius of non-polarized astrocytes were taken into account as "palisading". Most long processes were orientated perpendicularly to the core lesion. However, we detected occasionally astrocytes with long processes in diverting angles, which might be caused by collateral tissue damage. We included those cells in our quantification as well. "%palisading astrocytes" were

quantified as subset relative to the total number of GFAP+ astrocytes in the defined areas. Microglia morphometry was analyzed based on IBA1 immunoreactivity and the surface algorithm of Imaris. Kymographs were generated and analyzed via FiJi. Movies were compiled and annotated with Hitfilm Express 13 (FXhome Limited).

Focal adhesion analysis. To assess focal adhesion size, primary astrocytes were transduced with FIV lentivirus encoding for pCDF-GFAP:paxillin-EGFP. Seven days after transduction, medium was changed to phenol-free DMEM, and scratch injury was performed, followed by live-cell imaging for 22 h in 20 min intervals.

Acquired images were submitted to the Focal Adhesion Analysis Server[83] with the following specifications: Imaging frequency: 20 min; min. adhesion size 20, max. adhesion size 500; all further settings were left at default. The analyzed files obtained from the adhesion server were used to identify a region of interest at the leading edge of astrocytes extending into the scratch. Each Region of Interest contained at least 10 focal adhesions. Using the open source software INKSCAPE, the assigned number of every analyzed focal adhesion was identified and matched with the corresponding data (maximum adhesion size, mean adhesion size) from the excel-sheet as described on the focal adhesion analysis server website (https://faas.bme.unc.edu/results_understanding).

Surface biotinylation and internalization assay. Cultured astrocytes were incubated in 1 mg/ml cell-impermeant EZ-Link Sulfo-NHS-SS-Biotin (ThermoFisher) in ice-cold PBS pH 8 for 2 h. Any remaining unreacted biotin was removed by three washes with ice-cold PBS followed by 10 min of quenching with 100 mM glycine in ice-cold PBS. Cells were then split into four groups: (1) directed analyses of surface biotinylated proteins after labeling and quenching, (2) specificity control of surface biotinylation by removing biotin surface labeling with 50 mM 2-mercaptoethanesulfonic acid sodium salt (MESNA) in wash buffer (150 mM NaCl, 0.2% BSA, 20 mM Tris, pH 8.6), (3) pulse-chase analyses of internalized surface proteins after 15 min or (4) 30 min incubation at 37 °C in complete medium followed by MESNA-dependent removal of the surface-label. After three washes with wash buffer, samples were treated with 50 mM MESNA in wash buffer for 1 h on ice. Cell lysis of all samples was performed after two washes with ice-cold PBS by incubating cells for 20 min in ice-cold 1% Triton X-100 in PBS with protease inhibitor cocktails (Merck, Calbiochem set III, Cat. no. 539134), subsequent thorough scraping and sonication. Biotinylated proteins were isolated by incubating the samples with equal total protein amounts overnight at 4 °C and gentle agitation with 30 µl of Neutravidin-magnetic beads (Fisher Scientific, Cat. no. 11864143. The following day, beads were washed three times in ice-cold PBS + 1% Triton X-100 and twice with ice-cold PBS only. Samples were then subjected to sodium dodecyl sulfate polyacrylamide gel electrophoresis (SDS-PAGE) and WB probing with antibodies.

Protein lysate preparation, SDS–PAGE, and WB. Cultured astrocytes were washed once with cold PBS and lysed in cold radioimmunoprecipitation assay buffer, supplemented with protease inhibitors (Merck, Calbiochem set III, Cat. no. 539134). Cell lysates were centrifuged at $20,000 \times g$ and supernatant was transferred to a tube containing Roti load I SDS sample buffer. On average, 15–30 µg of protein was loaded on SDS–PAGE gel. Western blot analysis was performed by transferring proteins to nitrocellulose membranes using a wet blot tank system (Bio-Rad) for 2 h. The membranes were then blocked for 1 h at room temperature with 5% skim milk before incubating with primary antibodies overnight. Membranes were then washed 3 × 10 min in TBS-T and incubated with HRP-coupled secondary antibody for 1 hour, followed by 3 × 10 washes in TBS-T before detection. Membranes were imaged using the Fusion SL system from Vilber Lourmat. Quantification of band densities was performed using FIJI. The area of the band and the mean gray value were measured to obtain relative density. For relative quantifications, measurements were normalized to loading control.

Antibody-feeding assay. To visualize internalized active β1-integrin, astrocytes were first starved (DMEM without serum) for one hour and subsequently incubated with the 9EG7 antibody (BD Bioscience, 1:20 in DMEM) on ice for 1 h. After three washes with cold complete medium, cells were incubated for 30 min at 37 °C and 5% CO$_2$. Astrocytes were washed several times in PBS and then surface antibody was stripped with ice-cold acetic acid pH3 (0.5 M NaCl, 0.5% Acetic Acid in ddH$_2$O) followed by several washes in PBS before fixation.

In vivo stab wound. Mice were anesthetized with a mixture of ketamine (100 mg/kg) and xylazine (10 mg/kg), and head-fixed on a stereotactic frame (Kopf Stereotax). Throughout the operation, body temperature was maintained at 36–37 °C, using a heating blanket. Full anesthesia of the mice was verified throughout the procedure by carefully checking breathing and reflexes using the pinching toe method. For surgery, an incision was created in the scalp and a small craniotomy was drilled above M1 motor cortex (bregma: −1 mm; lateral: 1 mm). An injection needle (Hamilton, gauge 33 was carefully inserted into the motor cortex and moved up and down three times (0.8 mm). The needle was removed and the scalp was sutured. Metamizol (5 mg/ml) was added to drinking water as analgesics until sacrifice. After surgery, mice were replaced in their cage, and kept warm during

wake–up and recovery on a heating plate at 37 °C. Stab wound outcomes were analyzed 7 or 30 days later by IHC and confocal microscopy.

IHC and tissue clearance. Seven or 30 days after stab wound injury, mice were sedated with isoflurane, perfused with 4% formaldehyde and sacrificed. Coronal sections (60 μm diameter) were obtained, permeabilized with 1% Triton X-100 in PBS and blocked in 5% BSA. In a first step, sections were labeled with IHC for GFAP to label reactive astrocytes and identify lesion sites with adjacent scars. GFAP-positive sections were stained for additional marker proteins and subsequently fixed in 4% formaldehyde for 1 h at 4 °C. Tissue clearance was obtained by incubating brain slices in ScaleA2 (4 M UREA, 10% (wt/vol) glycerol, 0.1% (wt/vol) Triton X-100 and 0.1× PBS) for 48 h. Transparent slices were mounted on glass slides using Mowiol with 4 M UREA and analyzed using a Nikon A1 confocal microscope with a ×40 objective (N.A. 1.3, working distance 240 μm) and automated scanning stage. For visualization of RAB8 tubules in vivo, animals were sacrificed as described above and perfused with 3.7% formaldehyde in a cytoskeleton-preservation buffer (25 mM HEPES, 60 mM PIPES, 10 mM EGTA, 2 mM MgCl₂, pH 7.4). Slices were permeabilized with 0.02% Triton X-100 overnight and stained as described above in cytoskeleton-preservation buffer. For visualization of RAB8 tubules in vivo, no tissue clearing was performed and cells were mounted on glass slides using Mowiol without urea.

Histology. Brain slices adhered on superfrost coverslips overnight. Slices were pre-incubating in a descending ethanol series (96%-, 90%-, 70%-, 50%- and 30% ethanol, each step for 2 min). Cresyl violet (acetate) Certistain (Sigma-Aldrich) working solution was freshly prepared in manufacturer's acetate buffer solution (pH3.6) and filtered prior to use. Then slices were stained in cresyl violet solution for 20 min. Subsequently, slices were incubated for 1 sec in 96% ethanol and washed briefly with 70% ethanol. Clearing of slices was performed by two subsequent incubations in xylene for 2 min. Stained slices were mounted in water-free DPX medium (Sigma-Aldrich).

Purification of recombinant GST-hSLP4A and isolation of endogenous GTP-bound RAB8 from astrocytes. Recombinant GST-hSLP4A was expressed in and purified from BL21 Rosetta DE3 *Eschechia coli* (Merck, Ca. no. 70954). In all, 5 ml of saturated pDEST15-hSlp4-a-transformed BL21 Rosetta DE3 *E. coli* culture were diluted in 500 ml 2× YT (Sigma-Aldrich, Cat. no. Y2377-250G) with Ampicillin (Sigma-Aldrich, Cat. no. A9518) under shaking (230 rpm) for 3 h at 37 °C. Protein expression was induced by 1 mM isopropyl β-d-1-thiogalactopyranoside (Sigma-Aldrich, Cat. no. I6758) and occurred overnight at room temperature under shaking. Bacteria were harvested by centrifugation (Ja10 rotor, 5000 rcf for 15 min at 4 °C) and stored at −80 °C. Purification of GST-hSLP4A was performed directly before the isolation of GTP-bound RAB8 from astrocytes. Bacteria were resuspended in (50 mM HEPES, 250 mM NaCl, 10% glycerol plus 1% Triton X-100, supplemented with protease inhibitors (Merck, Calbiochem set III, Cat. No. 539134) and subsequently sonicated. Lysates were cleared by centrifugation (JA20 rotor, 25,402 × g, 25 min at 4 °C). Glutathione sepharose beads (Sigma-Aldrich, Cat. no. GE17-0756-01) were washed three times in HTG buffer (1% Triton, X-100, 25 mm HEPES, 150 mM NaCl, 10% glycerol). Bacterial lysates were incubated with glutathione sepharose beads for 1 hour on a rotating wheel at 4 °C. Beads were washed three times with ice-cold lysis buffer (20 mM HEPES, 150 mM NaCl, 0.5% Triton X-100). Subsequently, beads were incubated with astrocyte lysate buffer supplemented with protease inhibitors (Merck, Calbiochem set III, Cat. no. 539134) for 1 hour at 4 °C on a rotating wheel. After four times of washing with lysis buffer with protease inhibitors, samples were subjected to SDS–PAGE and WB.

Electron microscopy. Brain slices, fixed, permeabilized, and labeled for GFAP, were cryoprotected stepwise in 0.1 M sodium phosphate buffer pH 7.4 (PB) supplemented with increasing concentrations of glycerol [10–20–30% (v/v)] and left overnight in 30% glycerol in PBS at 4 °C. The tissue was frozen by plunging into hexane (Carl Roth) at −70 °C. Samples were transferred into cold methanol (−90 °C) in a freeze-substitution chamber (Leica EM AFS). Methanol was replaced three times before the specimens were immersed overnight in anhydrous methanol at −90 °C, containing 2% (w/v) uranyl acetate. After rinsing several times with methanol, the temperature was gradually raised to −50 °C and left overnight at −50 °C. Tissue was then infiltrated with a mix of Lowicryl HM20 resin (Polysciences) and methanol (1:2; 1:1; 2:1, 1 h each) and left in pure resin overnight at −50 °C. Samples were transferred to flat embedding molds containing freshly prepared resin at −50 °C. UV polymerization was started at −50 °C (overnight) and then continued for 4 d at temperatures gradually increasing from −50 °C to −20 °C (24 h) and finally to +20 °C (24 h). Ultrathin sections (70 nm) were mounted on 200-mesh formvar-coated nickel grids (Plano). Images were acquired using a Zeiss EM 900 equipped with a digital camera (Proscan 1 K Slow-Scan CCD Camera).

Statistics and reproducibility. All statistical analyses were performed in Graph-Pad Prism software (Prism 7.0). Details on the statistical tests applied are provided within the figure legends. The data are reported as bar graphs displaying individual values and means ± SEM, as indicated in the figure legends, or as box-and-whiskers plots, ranging from minimum to maximum values. All data were tested for normality and accordingly subjected to parametric or non-parametric statistical analysis. Test results for normality distribution are reported in the figure legends only when data were not normally distributed. No experiments were excluded from the analyses.

Data availability

All data supporting the findings of this study are provided within the paper and its supplementary information. All additional information will be made available upon reasonable request to the authors. Cartoons and schemes depicted in this manuscript were created by J.S. and K.M. with BioRender.com Source data are provided with this paper.

Code availability

The script to quantify tubules has been uploaded to Github and can be downloaded via the following link: https://github.com/jschiweck/TubuleMacro.git

References

1. Barker, R. A., Gotz, M. & Parmar, M. New approaches for brain repair-from rescue to reprogramming. *Nature* **557**, 329–334 (2018).
2. Schiweck, J., Eickholt, B. J. & Murk, K. Important shapeshifter: mechanisms allowing astrocytes to respond to the changing nervous system during development, injury and disease. *Front. Cell Neurosci.* **12**, 261 (2018).
3. Faulkner, J. R. et al. Reactive astrocytes protect tissue and preserve function after spinal cord injury. *J. Neurosci.* **24**, 2143–2155 (2004).
4. Frik J, et al. Cross-talk between monocyte invasion and astrocyte proliferation regulates scarring in brain injury. *EMBO Rep.* **19**, e45294 (2018).
5. Sofroniew, M. V. Astrocyte barriers to neurotoxic inflammation. *Nat. Rev. Neurosci.* **16**, 249–263 (2015).
6. Grintsevich, E. E. et al. Mapping of drebrin binding site on F-actin. *J. Mol. Biol.* **398**, 542–554 (2010).
7. Mikati, M. A., Grintsevich, E. E. & Reisler, E. Drebrin-induced stabilization of actin filaments. *J. Biol. Chem.* **288**, 19926–19938 (2013).
8. Aoki, C. et al. Drebrin A is a postsynaptic protein that localizes in vivo to the submembranous surface of dendritic sites forming excitatory synapses. *J. Comp. Neurol.* **483**, 383–402 (2005).
9. Butkevich, E. et al. Drebrin is a novel connexin-43 binding partner that links gap junctions to the submembrane cytoskeleton. *Curr. Biol.* **14**, 650–658 (2004).
10. He J. T., Li X. Y., Yang L, Zhao X. Astroglial connexins and cognition: memory formation or deterioration? *Biosci. Rep.* **40**, BSR20193510 (2020).
11. Pannasch, U. & Rouach, N. Emerging role for astroglial networks in information processing: from synapse to behavior. *Trends Neurosci.* **36**, 405–417 (2013).
12. Willmes, C. G. et al. Investigation of hippocampal synaptic transmission and plasticity in mice deficient in the actin-binding protein Drebrin. *Sci. Rep.* **7**, 42652 (2017).
13. Kreis, P. et al. ATM phosphorylation of the actin-binding protein drebrin controls oxidation stress-resistance in mammalian neurons and C. elegans. *Nat. Commun.* **10**, 486 (2019).
14. Yang, Y. et al. Molecular comparison of GLT1+ and ALDH1L1+ astrocytes in vivo in astroglial reporter mice. *Glia* **59**, 200–207 (2011).
15. Bardehle, S. et al. Live imaging of astrocyte responses to acute injury reveals selective juxtavascular proliferation. *Nat. Neurosci.* **16**, 580–586 (2013).
16. Robel, S., Bardehle, S., Lepier, A., Brakebusch, C. & Gotz, M. Genetic deletion of cdc42 reveals a crucial role for astrocyte recruitment to the injury site in vitro and in vivo. *J. Neurosci.* **31**, 12471–12482 (2011).
17. Nimmerjahn, A., Kirchhoff, F. & Helmchen, F. Resting microglial cells are highly dynamic surveillants of brain parenchyma in vivo. *Science* **308**, 1314–1318 (2005).
18. Alekseeva, O. S., Gusel'nikova, V. V., Beznin, G. V., Korzhevskii, D. E. [PROSPECTS OF THE NUCLEAR PROTEIN NeuN APPLICATION AS AN INDEX OF FUNCTIONAL STATE OF THE VERTEBRATE NERVE CELLS]. *Zh . Evol. Biokhim Fiziol.* **51**, 313–323 (2015).

51

19. Lucas, C. H., Calvez, M., Babu, R. & Brown, A. Altered subcellular localization of the NeuN/Rbfox3 RNA splicing factor in HIV-associated neurocognitive disorders (HAND). *Neurosci. Lett.* **558**, 97–102 (2014).

20. Shandra, O. et al. Repetitive diffuse mild traumatic brain injury causes an atypical astrocyte response and spontaneous recurrent seizures. *J. Neurosci.* **39**, 1944–1963 (2019).

21. Wang, J. et al. Comparison of different quantification methods to determine hippocampal damage after cerebral ischemia. *J. Neurosci. Methods* **240**, 67–76 (2015).

22. Wiley, C. A. et al. Ultrastructure of diaschisis lesions after traumatic brain injury. *J. Neurotrauma* **33**, 1866–1882 (2016).

23. Sun, W. et al. SOX9 is an astrocyte-specific nuclear marker in the adult brain outside the neurogenic regions. *J. Neurosci.* **37**, 4493–4507 (2017).

24. Menzel-Severing, J. et al. Transcription factor profiling identifies Sox9 as regulator of proliferation and differentiation in corneal epithelial stem/progenitor cells. *Sci. Rep.* **8**, 10268 (2018).

25. Cahoy, J. D. et al. A transcriptome database for astrocytes, neurons, and oligodendrocytes: a new resource for understanding brain development and function. *J. Neurosci.* **28**, 264–278 (2008).

26. Xu, W. & Stamnes, M. The actin-depolymerizing factor homology and charged/helical domains of drebrin and mAbp1 direct membrane binding and localization via distinct interactions with actin. *J. Biol. Chem.* **281**, 11826–11833 (2006).

27. Gautreau A., Oguievetskaia K., Ungermann C. Function and regulation of the endosomal fusion and fission machineries. *Cold Spring. Harb. Perspect. Biol.* **6**, a016832 (2014).

28. Simonetti, B. & Cullen, P. J. Actin-dependent endosomal receptor recycling. *Curr. Opin. Cell Biol.* **56**, 22–33 (2019).

29. Ginosyan, A. A., Grintsevich, E. E. & Reisler, E. Neuronal drebrin A directly interacts with mDia2 formin to inhibit actin assembly. *Mol. Biol. Cell* **30**, 646–657 (2019).

30. Li, Z. et al. Homer tetramer promotes actin bundling activity of drebrin. *Structure* **27**, 27–38 e24 (2019).

31. Kim, J. et al. Functional genomic screen for modulators of ciliogenesis and cilium length. *Nature* **464**, 1048–1051 (2010).

32. Nolen, B. J. et al. Characterization of two classes of small molecule inhibitors of Arp2/3 complex. *Nature* **460**, 1031–1034 (2009).

33. Rizvi, S. A. et al. Identification and characterization of a small molecule inhibitor of formin-mediated actin assembly. *Chem. Biol.* **16**, 1158–1168 (2009).

34. Peranen, J. Rab8 GTPase as a regulator of cell shape. *Cytoskeleton (Hoboken)* **68**, 527–539 (2011).

35. Wang, J. T., Teasdale, R. D. & Liebl, D. Macropinosome quantitation assay. *MethodsX* **1**, 36–41 (2014).

36. Delevoye, C. et al. BLOC-1 brings together the actin and microtubule cytoskeletons to generate recycling endosomes. *Curr. Biol.* **26**, 1–13 (2016).

37. Delevoye, C. et al. Recycling endosome tubule morphogenesis from sorting endosomes requires the kinesin motor KIF13A. *Cell Rep.* **6**, 445–454 (2014).

38. Tabdanov, E. D., Puram, V., Zhovmer, A. & Provenzano, P. P. Microtubule-actomyosin mechanical cooperation during contact guidance sensing. *Cell Rep.* **25**, 328–338 e325 (2018).

39. Hattula, K. et al. Characterization of the Rab8-specific membrane traffic route linked to protrusion formation. *J. Cell Sci.* **119**, 4866–4877 (2006).

40. Sun, Z., Guo, S. S. & Fassler, R. Integrin-mediated mechanotransduction. *J. Cell Biol.* **215**, 445–456 (2016).

41. Hara, M. et al. Interaction of reactive astrocytes with type I collagen induces astrocytic scar formation through the integrin-N-cadherin pathway after spinal cord injury. *Nat. Med.* **23**, 818–828 (2017).

42. North, H. A., Pan, L., McGuire, T. L., Brooker, S. & Kessler, J. A. beta1-Integrin alters ependymal stem cell BMP receptor localization and attenuates astrogliosis after spinal cord injury. *J. Neurosci.* **35**, 3725–3733 (2015).

43. Robel, S. et al. Conditional deletion of beta1-integrin in astroglia causes partial reactive gliosis. *Glia* **57**, 1630–1647 (2009).

44. Hariri, M. et al. Biogenesis of multilamellar bodies via autophagy. *Mol. Biol. Cell* **11**, 255–268 (2000).

45. Dun, X. P. et al. Drebrin controls neuronal migration through the formation and alignment of the leading process. *Mol. Cell Neurosci.* **49**, 341–350 (2012).

46. Koganezawa, N., Hanamura, K., Sekino, Y. & Shirao, T. The role of drebrin in dendritic spines. *Mol. Cell Neurosci.* **84**, 85–92 (2017).

47. Anderson, M. A. et al. Astrocyte scar formation aids central nervous system axon regeneration. *Nature* **532**, 195–200 (2016).

48. Sirko, S. et al. Astrocyte reactivity after brain injury-: the role of galectins 1 and 3. *Glia* **63**, 2340–2361 (2015).

49. Zamanian, J. L. et al. Genomic analysis of reactive astrogliosis. *J. Neurosci.* **32**, 6391–6410 (2012).

50. Li, B. et al. Drebrin restricts rotavirus entry by inhibiting dynamin-mediated endocytosis. *Proc. Natl Acad. Sci. USA* **114**, E3642–E3651 (2017).

51. Elizondo, D. M., Andargie, T. E., Haddock, N. L., Boddie, T. A. & Lipscomb, M. W. Drebrin 1 in dendritic cells regulates phagocytosis and cell surface receptor expression through recycling for efficient antigen presentation. *Immunology* **156**, 136–146 (2019).

52. Grigoriev, I. et al. Rab6, Rab8, and MICAL3 cooperate in controlling docking and fusion of exocytotic carriers. *Curr. Biol.* **21**, 967–974 (2011).

53. Ryan, T. A. & Tumbarello, D. A. Optineurin: a coordinator of membrane-associated cargo trafficking and autophagy. *Front Immunol.* **9**, 1024 (2018).

54. van Weering, J. R. & Cullen, P. J. Membrane-associated cargo recycling by tubule-based endosomal sorting. *Semin. Cell Dev. Biol.* **31**, 40–47 (2014).

55. Naslavsky N., Caplan S. The enigmatic endosome - sorting the ins and outs of endocytic trafficking. *J. Cell Sci.* **131**, jcs216499 (2018).

56. Bowman, S. L., Shiwarski, D. J. & Puthenveedu, M. A. Distinct G protein-coupled receptor recycling pathways allow spatial control of downstream G protein signaling. *J. Cell Biol.* **214**, 797–806 (2016).

57. Puthenveedu, M. A. et al. Sequence-dependent sorting of recycling proteins by actin-stabilized endosomal microdomains. *Cell* **143**, 761–773 (2010).

58. Derivery, E. et al. The Arp2/3 activator WASH controls the fission of endosomes through a large multiprotein complex. *Dev. Cell* **17**, 712–723 (2009).

59. Sato, T. et al. The Rab8 GTPase regulates apical protein localization in intestinal cells. *Nature* **448**, 366–369 (2007).

60. Vacca, B. et al. Drebrin E depletion in human intestinal epithelial cells mimics Rab8a loss of function. *Hum. Mol. Genet* **23**, 2834–2846 (2014).

61. Sakane, A. et al. Rab13 small G protein and junctional Rab13-binding protein (JRAB) orchestrate actin cytoskeletal organization during epithelial junctional development. *J. Biol. Chem.* **287**, 42455–42468 (2012).

62. Sakane, A. et al. Conformational plasticity of JRAB/MICAL-L2 provides "law and order" in collective cell migration. *Mol. Biol. Cell* **27**, 3095–3108 (2016).

63. Shafaq-Zadah, M. et al. Persistent cell migration and adhesion rely on retrograde transport of beta(1) integrin. *Nat. Cell Biol.* **18**, 54–64 (2016).

64. Wanner, I. B. et al. Glial scar borders are formed by newly proliferated, elongated astrocytes that interact to corral inflammatory and fibrotic cells via STAT3-dependent mechanisms after spinal cord injury. *J. Neurosci.* **33**, 12870–12886 (2013).

65. Tsai, H. H. et al. Regional astrocyte allocation regulates CNS synaptogenesis and repair. *Science* **337**, 358–362 (2012).

66. Martinet, W. & De Meyer, G. R. Autophagy in atherosclerosis: a cell survival and death phenomenon with therapeutic potential. *Circ. Res* **104**, 304–317 (2009).

67. Kegel, K. B. et al. Huntingtin expression stimulates endosomal-lysosomal activity, endosome tubulation, and autophagy. *J. Neurosci.* **20**, 7268–7278 (2000).

68. Nixon, R. A. et al. Extensive involvement of autophagy in Alzheimer disease: an immuno-electron microscopy study. *J. Neuropathol. Exp. Neurol.* **64**, 113–122 (2005).

69. Sasaki, S. Autophagy in spinal cord motor neurons in sporadic amyotrophic lateral sclerosis. *J. Neuropathol. Exp. Neurol.* **70**, 349–359 (2011).

70. Morizawa, Y. M. et al. Reactive astrocytes function as phagocytes after brain ischemia via ABCA1-mediated pathway. *Nat. Commun.* **8**, 28 (2017).

71. Tsien, J. Z. et al. Subregion- and cell type-restricted gene knockout in mouse brain. *Cell* **87**, 1317–1326 (1996).

72. Guizetti, J. et al. Cortical constriction during abscission involves helices of ESCRT-III-dependent filaments. *Science* **331**, 1616–1620 (2011).

73. Laukaitis, C. M., Webb, D. J., Donais, K. & Horwitz, A. F. Differential dynamics of alpha 5 integrin, paxillin, and alpha-actinin during formation and disassembly of adhesions in migrating cells. *J. Cell Biol.* **153**, 1427–1440 (2001).

74. Worth, D. C., Daly, C. N., Geraldo, S., Oozeer, F. & Gordon-Weeks, P. R. Drebrin contains a cryptic F-actin-bundling activity regulated by Cdk5 phosphorylation. *J. Cell Biol.* **202**, 793–806 (2013).

75. Murk, K., Blanco Suarez, E. M., Cockbill, L. M., Banks, P. & Hanley, J. G. The antagonistic modulation of Arp2/3 activity by N-WASP, WAVE2 and PICK1 defines dynamic changes in astrocyte morphology. *J. Cell Sci.* **126**, 3873–3883 (2013).

76. Schrotter, S., Leondaritis, G. & Eickholt, B. J. Capillary isoelectric focusing of Akt isoforms identifies highly dynamic phosphorylation in neuronal cells and brain tissue. *J. Biol. Chem.* **291**, 10239–10251 (2016).

77. Wittenmayer, N. et al. Postsynaptic Neuroligin1 regulates presynaptic maturation. *Proc. Natl Acad. Sci. USA* **106**, 13564–13569 (2009).

78. Wu, L. et al. Rab8a-AS160-MSS4 regulatory circuit controls lipid droplet fusion and growth. *Dev. Cell* **30**, 378–393 (2014).

79. Demir, K. et al. RAB8B is required for activity and caveolar endocytosis of LRP6. *Cell Rep.* **4**, 1224–1234 (2013).

52

80. Etienne-Manneville, S. & Hall, A. Integrin-mediated activation of Cdc42 controls cell polarity in migrating astrocytes through PKCzeta. *Cell* **106**, 489–498 (2001).

81. Hiroyasu, S., Colburn, Z. T. & Jones, J. C. A hemidesmosomal protein regulates actin dynamics and traction forces in motile keratinocytes. *FASEB J.* **30**, 2298–2310 (2016).

82. Pasqualin, C., Gannier, F., Malecot, C. O., Bredeloux, P. & Maupoil, V. Automatic quantitative analysis of t-tubule organization in cardiac myocytes using ImageJ. *Am. J. Physiol. Cell Physiol.* **308**, C237–C245 (2015).

83. Berginski, M. E. & Gomez, S. M. The Focal Adhesion Analysis Server: a web tool for analyzing focal adhesion dynamics. *F1000Res* **2**, 68 (2013).

Author contributions

J.S., K.M., A.M.W., M.O., and J.L. performed the experiments. J.S. and K.M. analyzed the experiments. J.S. developed the automated script for tubule quantification. K.M., B.J.E., and I.V. supervised experiments. K.M. and B.J.E. designed the study. K.M., B.J.E., and J.S. wrote the manuscript.

Competing interests

The authors declare no competing interests.

Additional information

Supplementary information The online version contains supplementary material available at https://doi.org/10.1038/s41467-021-21662-x.

Correspondence and requests for materials should be addressed to K.M. or B.J.E.

Peer review information *Nature Communications* thanks Binhai Zheng and the other, anonymous, reviewer(s) for their contribution to the peer review of this work. Peer reviewer reports are available.

Reprints and permission information is available at http://www.nature.com/reprints

**Publisher's note** Springer Nature remains neutral with regard to jurisdictional claims in published maps and institutional affiliations.

53

Supplementary Information

Supplementary Figure S1: Injury-dependent upregulation of DBN in astrocytes. (A) Widefield mosaic scan of 25 fields of view from confluent astrocyte cultures labeled with anti-DBN, without or 24 h after mechanical injury. Relative DBN fluorescence is displayed as heatmap. Scale bars: 100 μm. Representative image of 3 independent experiments. (B) IHC of uninjured or injured mouse brain. Upper panel shows a strong labeling of DBN (green) around MAP2+ dendrites (blue), and no DBN labeling in S100ß+ astrocytes (magenta) in the uninjured mouse brain. Images are single confocal sections. Representative images of 2 animals. Scale bars: 10 μm. Close up image (1) show that DBN+ structures emerge from MAP2+ dendrites, which identifies them as dendritic spines. Line-scan through an S100ß+ astrocyte in close up image (2) shows little overlap of DBN and S100ß signal. Center panel shows IHC of DBN protein in uninjured BAC Aldh1l1 EGFP mice. Aldh1l1:GFP+ astrocytes (green) are negative for GFAP (blue) and DBN (magenta) in uninjured settings. Bottom panel shows IHC of DBN expression (grey) in BAC Aldh1l1 EGFP mice 7 days post-stab-injury. Astrocyte reactivity at lesion sites was determined by GFAP (blue), whilst astrocytes independent of their reactivity were visualized by GFP expression (green). Magnifications demonstrate astrocytes exhibiting prominent (1) and moderate (2) DBN protein levels. Images are confocal stacks. Representative images of 2 animals. Scale bars: 20 μm. (C) Microglia-enriched cultures were labeled for DBN (green) and the microglia marker IBA1 (magenta). IBA1+ microglia are negative for DBN (asterisks), whilst neighboring reactive astrocytes (arrowheads) are DBN+. Representative images of 3 experiments. Scale bars: 10 μm.(D) IHC of DBN (green) and IBA1 (magenta) in the uninjured cortex of P30 WT mice or 7 days post injury. Representative images of 3 animals. Scale bars: 10 μm. Images in (C) and (D) are single confocal planes. Source data are provided as a Source Data file.
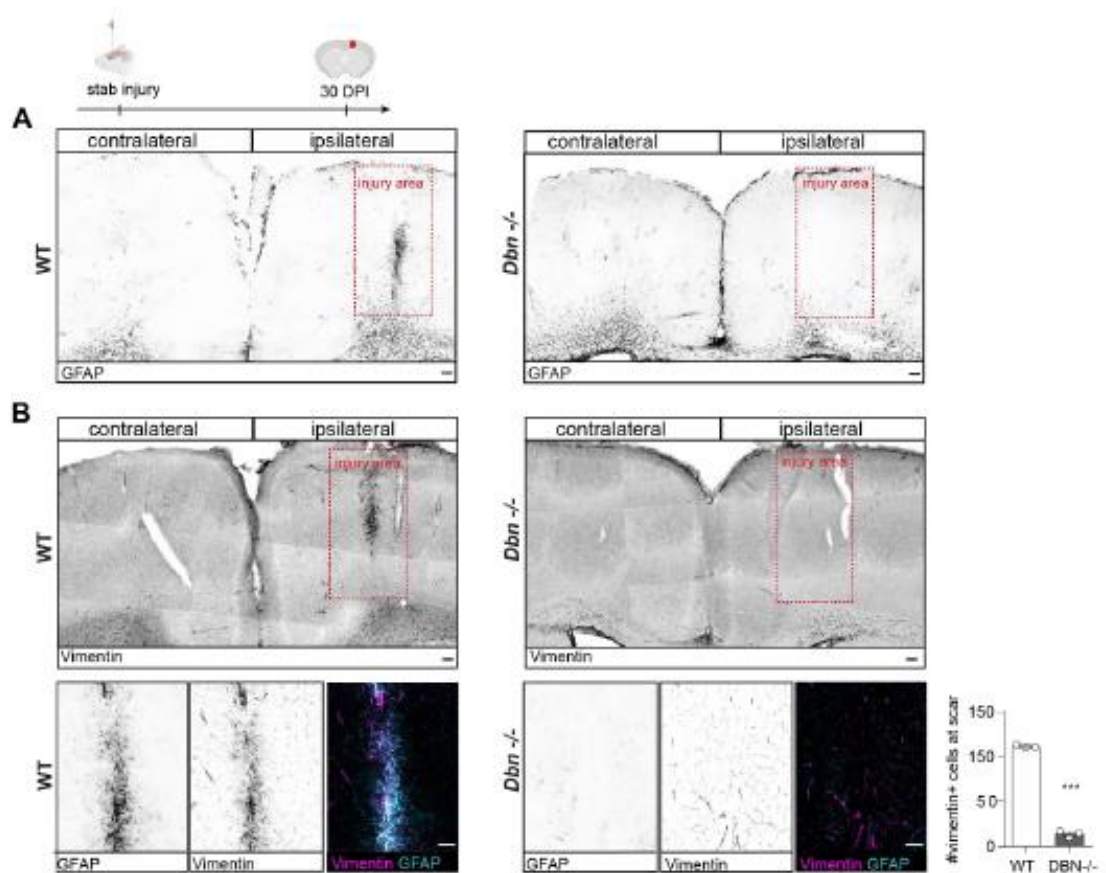
Supplementary Figure S2: Distribution of the reactive astrocyte markers GFAP and vimentin in WT and *Dbn*^{-/-} cortices. (A) Overview images of WT and *Dbn*^{-/-} cortices stained for GFAP 30 days post stab injury. Uninjured cortical tissue show little GFAP immunoreactivity. White matter astrocytes in the adjacent corpus callosum are overall GFAP+. WT but not *Dbn*^{-/-} cortices show GFAP+ reactive astrocytes at stab wounds (dashed box). Representative images of 11 WT and 13 *Dbn*^{-/-} animals. Scale bars: 100 µm. (B) Overview images of WT and *Dbn*^{-/-} cortices stained for vimentin 30 days post stab injury (upper panel). In WT brains, the vimentin antibody labels blood vessels and reactive astrocytes at stab wounds (dashed box). *Dbn*^{-/-} cortices lack vimentin+ astrocytes at injury sites. Scale bars: 100 µm. Bottom panel shows stab injuries labeled for GFAP and vimentin. Reactive WT astrocytes were positive for both GFAP and vimentin. Injury sites in DBN *Dbn*^{-/-} brains exhibit vimentin signals only around blood vessels. Scale bars: 100 µm. Quantification of vimentin+ cells at stab wounds 30 DpI shows means, individual data points and SEM; n=3 animals, *** P= 0.00000219 (Students unpaired t-test, two-sided, t=40.63 df=4). All images are confocal stacks. Source data are provided as a Source Data file.
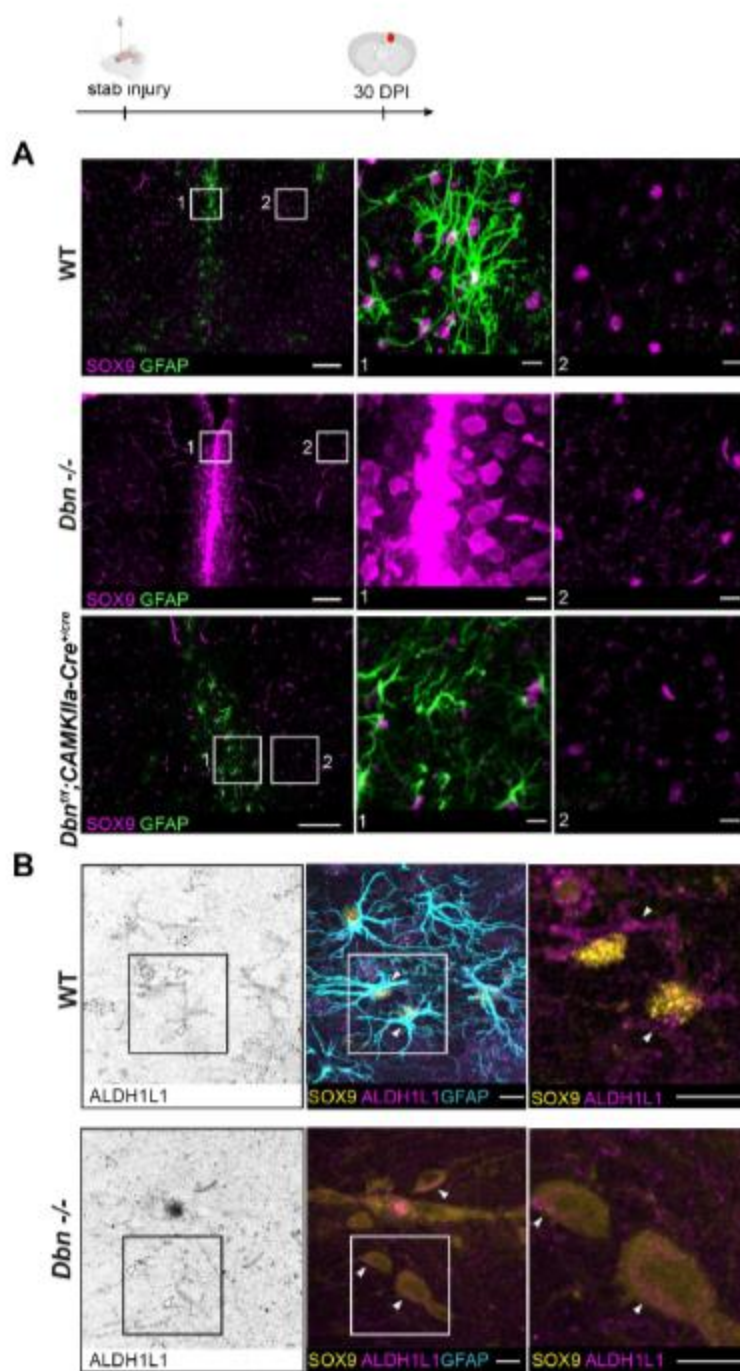
Supplementary Figure S3: Analyses of SOX9+ cells at stab wounds of WT, *Dbn*^-/- and *Dbn*^fl/fl^; *CAMKIIa-Cre*^+/cre^ mice (30 DPI). (A) IHC of stab wounds labeled for SOX9 (magenta) and GFAP (green) in WT (upper panel), *Dbn*^-/- (center panel) and *Dbn*^fl/fl^; *CAMKIIa-Cre*^+/cre^ brains (bottom panel). Close up images (1) show lesion sites, while close up images (2) magnify uninjured tissue. Scale bars overviews: 100 µm; Scale bars close up images: 10 µm. Representative images of 3 animals/condition. Images are confocal stacks (B) Triple labeling of ALDH1L1 (magenta), SOX9 (yellow) and GFAP (cyan) in stab wounds of WT and *Dbn*^-/- brains (30 DPI). Arrow heads indicate ALDH1L1 signals in cell bodies of SOX9+ cells. Representative images of 3 animals/condition Scale bars: 10 µm. Overviews are confocal stacks, while close ups are single confocal sections. Source data are provided as a Source Data file.
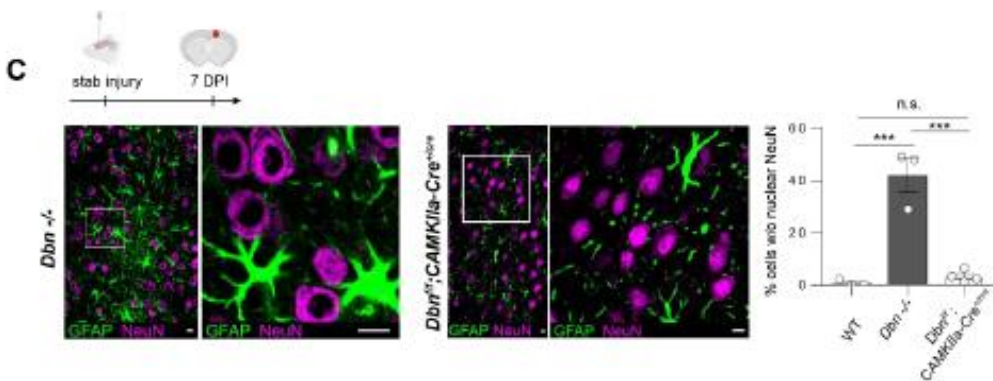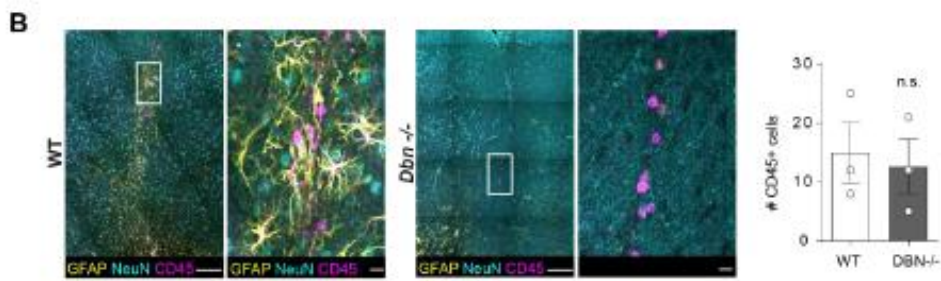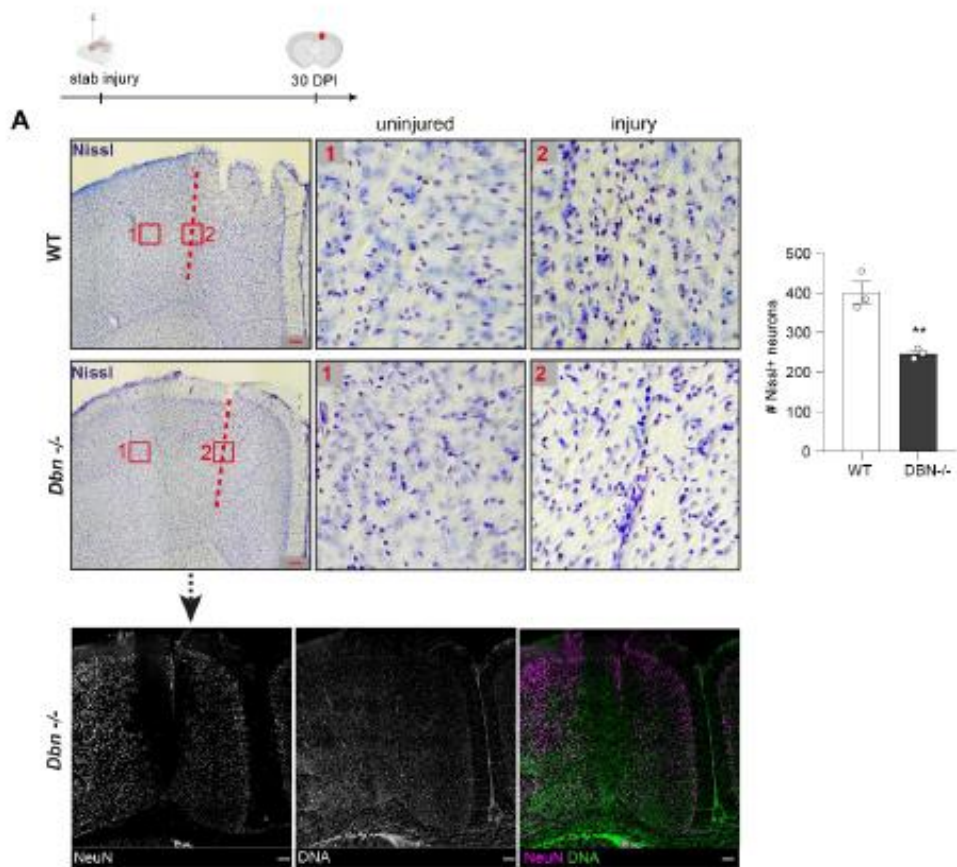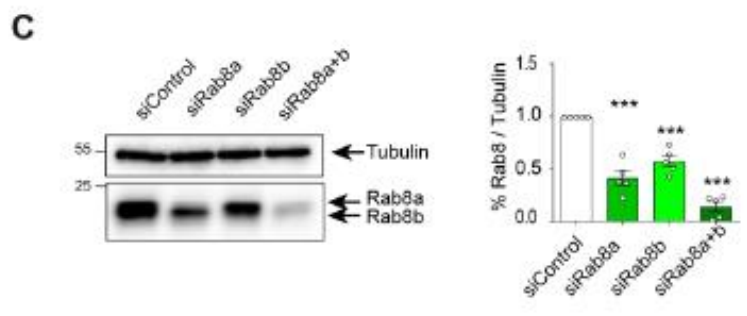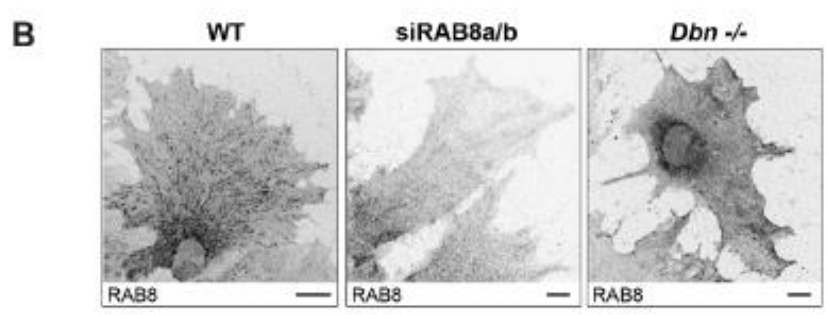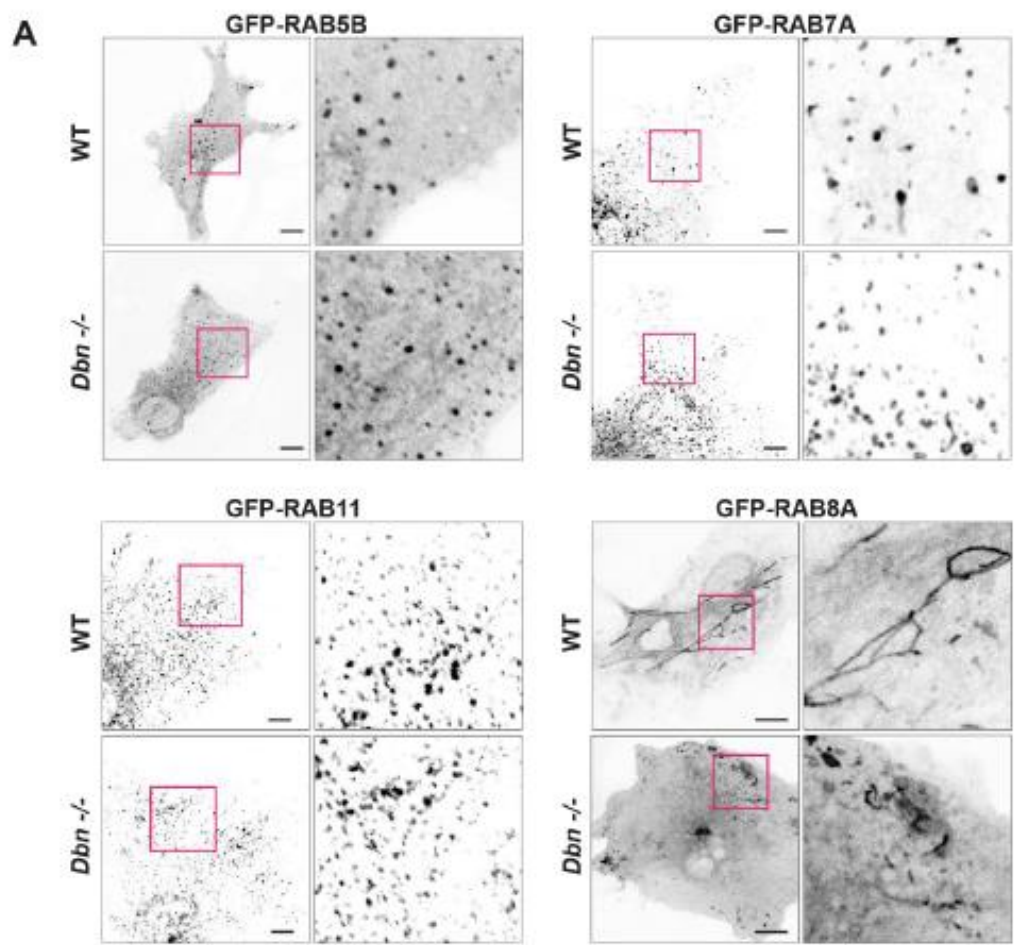
Supplementary Figure S4: Histological and immunohistochemical analyses of stab wounds in WT, *Dbn*^{-/-} and *Dbn*^{fl/fl}; *CAMKIIa-Cre*^{+/cre} mice (30 DPI). Nissl labeling of cortices from WT and *Dbn*$^{-/-}$ mice after stab wounding (30 DPI). Close up images (1) show uninjured tissue. Close up images (2) show tissue around stab wounds (dashed lines). Scale bars: 100 µm. Quantification of neurons, characterized by large Nissl+ cell bodies, 300 µm around the lesion sites, displayed as bar graphs showing mean, individual data points and SEM. n=3, ** *P*=0.0055 (Unpaired t-test, two-sided t=5.448, df=4). Lower panel shows the same *Dbn*$^{-/-}$ brain slice as above stained for NeuN (magenta) and DNA (green). (B) WT and *Dbn*$^{-/-}$ brains after stab wound (30 DPI) labeled for GFAP (yellow), NeuN (cyan) and CD45 (yellow). Scale bars: overview: 100 µm, magnification: 10µm. Quantification (means, individual data points and SEM) of CD45+ cells in stab wounded WT and *Dbn*$^{-/-}$ brains. n=3 animals, n.s. *P*=0.7527 (Unpaired t-test, two-sided, t=0.3376, df=4). (C) IHC of GFAP (green) and NeuN (magenta) in *Dbn*$^{fl/fl}$; *CAMKIIa-Cre*$^{+/cre}$ mice (7 DPI). Scale bars: 10 µm. Bar chart shows quantification (means, individual data points and SEM) of neurons without nuclear NeuN at injury sites of *Dbn*$^{fl/fl}$; *CAMKIIa-Cre*$^{+/cre}$ mice (7 DPI) and WT and *Dbn*$^{-/-}$ mice, as shown in Figure 2C. n=3 for WT and *Dbn*$^{-/-}$, 4 for *Dbn*$^{fl/fl}$; *CAMKIIa -Cre*$^{+/cre}$ (One-way ANOVA F=42.89, DFn=2, DFd=7; Tukey's multiple comparisons test: WT vs *Dbn*$^{-/-}$ *** *P*= 0.000214, WT vs. *CAMKIIa-Cre*$^{+/cre}$ n.s. *P*= 0.8631, *CAMKIIa-Cre*$^{+/cre}$ vs *Dbn*$^{-/-}$ *P*= 0.000208). All images are confocal stacks. Source data are provided as a Source Data file.
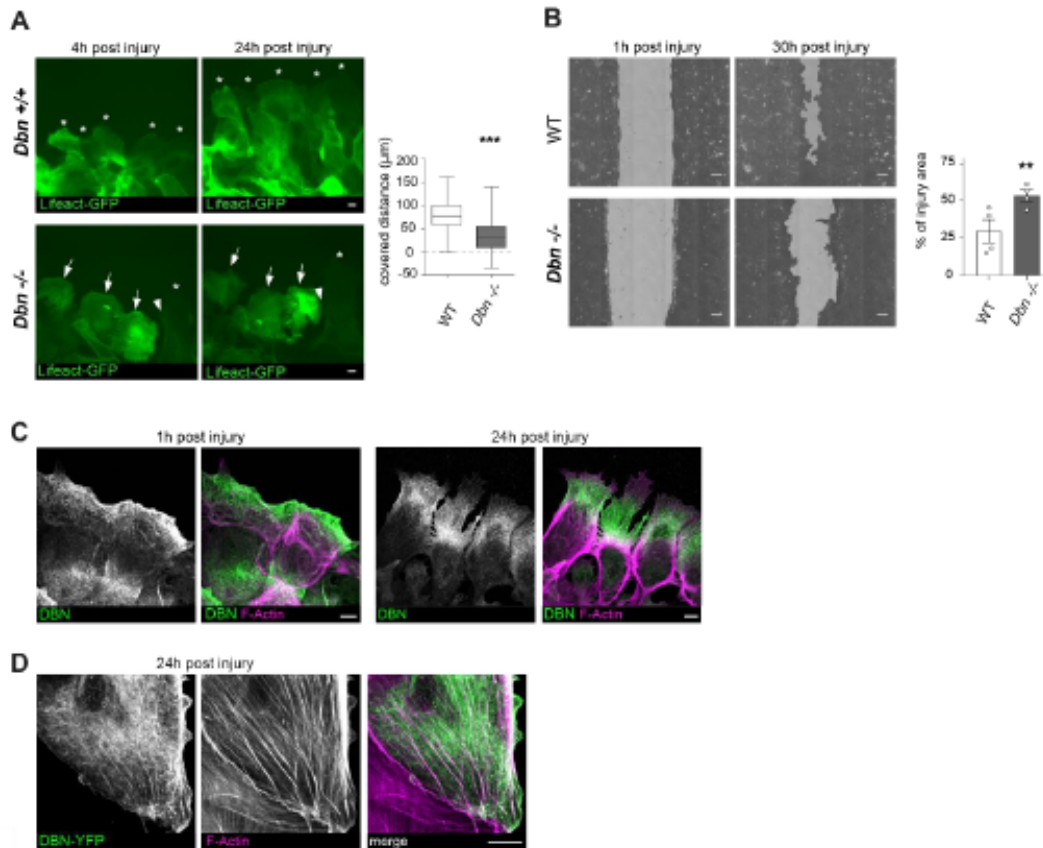
Supplementary Figure S5: DBN-loss perturbs the coordinated outgrowth of cultured astrocytes after scratch injury. (A) WT and *Dbn*⁻ᐟ⁻ astrocytes expressing Lifeact-GFP, at 4 h and 24 h after mechanical injury *in vitro*. Asterisks indicate cells with extending processes in a persistent manner towards injury. Arrows show moving cells with erratic migratory behavior. The arrowhead show retracting astrocytes. Scale bars: 10 µm. Images were acquired by widefield microscopy. Quantification shows box and whisker plots (box extends from 25th to 75th percentiles, central line=median, whiskers comprise all values from minimum to maximum) of distances covered by WT and *Dbn*⁻ᐟ⁻ astrocytes; n=180 cells per group obtained from three independent experiments, *** *P* < 0.0001 (Students unpaired t-test, two-sided, t=13.2 df=358). (B) Live imaging of the overall wound closure of cultured WT and *Dbn*⁻ᐟ⁻ astrocytes after 1 and 30 h. Scale bars: 100 µm. Bar diagram shows quantification of wound size 30 h after injuring the astrocyte monolayers (means, individual data points and SEM); n=4 independent experiments, Two-way repeated measurements ANOVA, F= 7.804, DFn=1, DFd=6; Sidak's multiple comparisons test: ** P=0.0038). (C) DBN and F-Actin labeling in cultured astrocyte during scratch injury. 1h post injury, DBN localizes to the rear and leading edge of injured astrocytes and shows little co-localization with the most prominent actin filaments. 24h after injury, DBN is detected between the leading edge and the actin-rich cell body, showing again little co-localization with typical actin fibers. Representative images of 3 independent experiments. Scale bars: 10µm. (D) Localization of DBN-YFP in vesicular and tubular structures and, partially, on actin fibers. Scale bar: 10µm. Representative images of 3 experiments. Images in (C) and (D) are single confocal sections. Source data are provided as a Source Data file.

A

GFP-RAB5B

GFP-RAB7A

GFP-RAB11

GFP-RAB8A

WT

Dbn -/-

B

WT

siRAB8a/b

Dbn -/-

RAB8

RAB8

RAB8

C

siControl   siRab8a   siRab8b   siRab8a+b

55 — ← Tubulin

25 — ← Rab8a
       ← Rab8b

% Rab8 / Tubulin

1.5

1.0

0.5

0.0

siControl   siRab8a   siRab8b   siRab8a+b

*** *** ***

Supplementary Figure S6: Localization and specificity RAB-GTPases in astrocytes during injury. (A) Expression of different GFP-tagged RAB GTPases in cultured WT and *Dbn*^{-/-} astrocytes. No major differences between genotypes could be detected for RAB5b, 7A and 11; RAB8A formed tubular structures in WT but not in *Dbn*^{-/-} astrocytes. Representative images of 3 experiments. Scale bars: 10 μm. (B) WT astrocytes, WT astrocytes transfected RAB8A+ siRNA and *Dbn*^{-/-} astrocytes; demonstrating the specificity of the antibody used. Scale bars: 10 μm. Representative images of 3 independent experiments. Image are confocal stacks. (C) Western blot of RAB8 levels using a pan RAB8 antibody in lysates derived from WT astrocytes transfected with control siRNA (siControl), Rab8a specific siRNA (siRab8a) and/or Rab8b specific siRNA (siRab8b). Tubulin immunoreactivity serves as loading control. Rab8 and Tubulin antibody incubations were performed on the same membrane on consecutive days without stripping. Bar diagram shows quantification of RAB8 levels from siRNA transfected astrocytes from corresponding western blots, displaying means, individual data points and SEM (n=5 independent experiments, One way ANOVA F= 55.82 (DFn=3,DFd= 16), Bonferroni's multiple comparisons test ***P<0.001; multiplicity adjusted p-values: siControl vs siRab8a: P= 0.000001199564256; siControl vs siRab8b: P= 0.000065561231107; siControl vs siRab8a+b: P= 0.000000005946593). Source data are provided as a Source Data file.
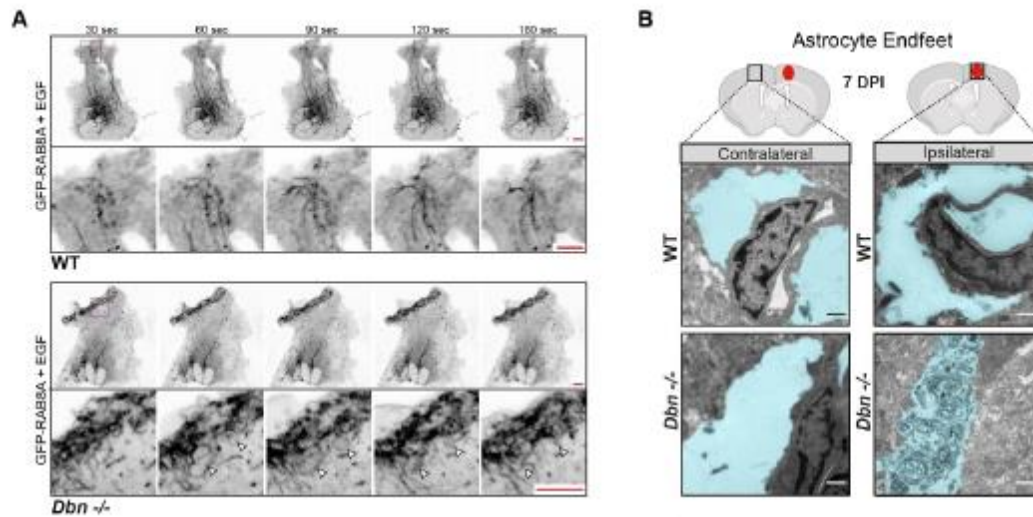
Supplementary Figure S7: DBN-loss results in accumulation of membranes in astrocytes. (A) WT and *Dbn*⁻/⁻ astrocytes expressing GFP-RAB8A after starvation and brief stimulation with EGF (see Movies 5 and 6). Images are confocal stacks acquired during live imaging. Representative images of 3 experiments. Scale bars: 10 μm. Images are confocal stacks. (B) TEM images showing accumulation of multilamellar bodies in endfeet of astrocytes in *Dbn*⁻/⁻ brains, but not in endfeet of astrocytes in WT brains after injury *in vivo* 7 DPI. Astrocyte endfeet are shaded in blue. Representative images of 3 animals/condition. Scale bars: 500 nm. Source data are provided as a Source Data file.

Supplementary Table S8 .List of primers.

Name	Sequence 5'-3'	Purpose
pCDF-New MCS-s	CTAGAGCTAGCGCTACCGGTCGCCACCATGGGATGTACAGCGGCCGCG	Cloning
pCDF-New MCS-as	TCGACGCGGCCGCTGTACATCCCATGGTGGCGACCGGTAGCGCTAGCT	Cloning
pGFAP-5	ATAGATATCAACATATCCTGGTGTGGAGTAGGG	Cloning
pGFAP-3	ATAGCTAGCGCGAGCAGCGGAGGTGATGCGTC	Cloning
pCDF-GFP-5	GACCTCCATAGAAGATTCTAGAGCTAGCATGGTGAGCAAGGGCGAGGAGCTGTTC	Cloning
pCDF-RAB8A-3	GTAATCCAGAGGTTGATTGTCGACTCACAGAAGAACACATCGGAAAAAGCTGC	Cloning
Paxillin-BsrGImut-s	GAGGAGGAACACGTGTATAGCTTCCCAAACAAGCAG	Mutagenesis
Paxillin-BsrGImut-as	CTGCTTGTTTGGGAAGCTATACACGTGTTCCTCCTC	Mutagenesis
CAMKII Cre FW wt+cre	GGTTCTCCGTTTGCACTCAGGA	Genotyping
CAMKII Cre B RV cre	CCTGTTGTTCAGCTTGCACCAG	Genotyping
CAMKII C B RV WT	CTGCATGCACGGGACAGCTCT	Genotyping
siRAB8A	GGAAUAAGUGUGAUGUGAA	RNAi
siRAB8B	GAAUGAUCCUGGGUAACAA	RNAi
siControl	AGGUAGUGUAAUCGCCUUGUU	RNAi

Curriculum Vitae

My curriculum vitae does not appear in the electronic version of my paper for reasons of data protection.

List of Publications

Murk, K., Ornaghi, M., **Schiweck, J.**, Profilin Isoforms in Health and Disease – All the Same but Different. Front Cell Dev Biol. 9, 2086 (2021).

Schiweck, J., Murk, K., Ledderose, J. et al. Drebrin controls scar formation and astrocyte reactivity upon traumatic brain injury by regulating membrane trafficking. Nat Commun 12, 1490 (2021).

Schiweck, J., Eickholt, B. J. & Murk, K. Important shapeshifter: mechanisms allowing astrocytes to respond to the changing nervous system during development, injury and disease. Front. Cell Neurosci. 12, 261 (2018).

Schiweck, J., Beauchamp, M., Humo, M., Lelievre, V. (2015) Old friends, new story: The role of Slit2C signaling through PlexinA1. Cell Adh Migr. 9(6):417-421.

Acknowledgements

This thesis and all the steps along the way would not have been possible without the support of many people to whom I wish to express my gratitude.

First and foremost, I would like to thank my doctoral supervisor, Prof. Dr. Britta Eickholt, to whom I am very grateful for accepting me in her laboratory and giving me the chance to obtain a PhD. I want to thank her for her scientific input, her support scientifically as well as financially throughout my whole PhD, for encouraging me to pursue a career in science, for excellent training opportunities and promoting scientific exchange by arranging research stays, conferences and collaboration opportunities. I also thank Prof. Eickholt for her positive attitude, curiosity and generosity, allowing me to pursue my own ideas and scientific questions.

I would also like to thank my supervisor and co-author Dr. Kai Murk, from whom I learned everything I know about astrocytes and laboratory techniques. I would like to thank Dr. Murk for his guidance, for his patience, for his constant support and his great ideas for our project, for many interesting discussions, for teaching me about life in academia, for a lot of coffees, burgers, and the right jokes in the right moments.

I further would like to thank my friend and colleague Joachim Fuchs, who not only offered great scientific input and taught me techniques, but also made conferences much more fun. I also thank him for his reflections on science and society which lead to great discussions and helped me accept that experiments rarely lead to black and white results.

Grazie to my colleague Marta Ornaghi for working on projects together and a lot of parmigiana, pasta and early morning swimming sessions. Danke to my colleague Shannon Bareesel for great talks and nice coffee breaks. Danke to Jonas Hollemann for being an excellent Master student who taught me as much as I taught him. Merci to Patricia Kreis for being an inspiring scientist, her positive attitude and talks about science and careers.

A big thank you to all my former and current colleagues for their help, support and criticism, for creating a nice work environment and making work a place where I wanted to be. I would also like to thank Daniela Höcke, who made the administrative side of work much easier by being kind, efficient and extremely helpful.

A PhD would be unthinkable without the support of my family and friends. I thank my mum Christiane Schiweck and my dad Dr. Helmut Schiweck for believing in me and supporting me on every step of the way from kindergarden to Charité. I thank them for being there no matter what and for always seeing the good in me.

I thank my sisters for the many memories that made me who I am, for their support and for letting me know I can rely on them. Specifically, I thank my sister Dr. Carmen Schiweck for always being there, for calling me every day, for the many visits and jokes, but also for scientific discussions and for always knowing what I am going through. I thank my sister Melanie Hein for being loving and caring, for insisting on bringing guinny pigs into my life, for giving me a different perspective on life and a wonderful niece and nephew. I thank my sister Nicole Schiweck for countless great moments together, for letting me practice my teaching on her and for being a wonderful sister.

I also thank my dear friend Dr. Pina Knauff, who changed my life in Berlin. I thank her for countless hours of talking, for many nice runs, swims, yoga sessions, for scientific discussion and collaboration, for small and big adventures and her support.

Last but not least, I thank my partner Ricardo Paricio Montesinos, for the countless nights he listened to my presentations, the crash courses in science on Sunday mornings, for accompanying me during the PhD and other marathons, for reading my manuscripts and improving my figures, for being the person who understands me better than myself, for insisting on a work-life balance, for great holidays and his support in all aspects of life.